

Hierarchical Structure of Silk Materials Versus Mechanical Performance and Mesoscopic Engineering Principles

Wu Qiu, Aniruddha Patil, Fan Hu, and Xiang Yang Liu*

A comprehensive review on the five levels of hierarchical structures of silk materials and the correlation with macroscopic properties/performance of the silk materials, that is, the toughness, strain-stiffening, etc., is presented. It follows that the crystalline binding force turns out to be very important in the stabilization of silk materials, while the β -crystallite networks or nanofibrils and the interactions among helical nanofibrils are two of the most essential structural elements, which to a large extent determine the macroscopic performance of various forms of silk materials. In this context, the characteristic structural factors such as the orientation, size, and density of β -crystallites are very crucial. It is revealed that the formation of these structural elements is mainly controlled by the intermolecular nucleation of β -crystallites. Consequently, the rational design and reconstruction of silk materials can be implemented by controlling the molecular nucleation via applying shearing force and seeding (i.e., with carbon nanotubes). In general, the knowledge of the correlation between hierarchical structures and performance provides an understanding of the structural reasons behind the fascinating behaviors of silk materials.

1. Introduction

Silks spun by *Nephila pilipes* spiders and *Bombyx mori* silkworms are typical examples of natural, soft materials with mesoscopic hierarchical structures. Owing to the extraordinary mechanical properties^[1–3] and biocompatibility,^[4] heat-conducting ability, controllable dissolution, and wide optical window, silk materials are considered to be among the most promising materials of the twenty-first century, and have attracted considerable

interest within the scientific community (Figure 1a).^[5] Silk materials have already been applied in many fields, such as tissue engineering,^[3] flexible photonics and electronics,^[6] drug delivery,^[7] biological analysis,^[8] and lithography (Figure 1b).^[9]

For many soft materials, including silk materials, the macroscopic performance is controlled largely by the unique structures, whose size ranges from the nanoscale to the mesoscale level. In general, the performance of soft materials is highly correlated to the following four structural factors^[10–12]:

1. *Topology*: It demonstrates how joints/points are associated with each other. In principle, network modifications often begin with an alternation in topology.
2. *Correlation Length, ξ* : It describes the average distance between two correlated joints/points. In terms of hierarchical structure, the joints/points refer to structural units at the same level.
3. *Ordering/Symmetry of Structural Units*: In many situations, structural units in a network are anisotropic. The ordering/symmetry enable us to understand how these structural units are patterned.
4. *Strength of Interactions*: Notably, the interactions between adjacent structural units can be of the physical, thermodynamic, or chemical type.


The stability of networks is largely controlled by the strength of these interactions. To obtain a comprehensive understanding of the correlation between the structure and performance of soft materials, a more precise insight into the hierarchical structures of soft materials is required; this has also inspired scientists and engineers to fabricate advanced functionalized soft materials, by effectively manipulating the aforementioned structural factors.^[13] Although numerous attempts have been made to characterize the hierarchical structures of silk materials, the mechanism by which the multilevel structures of silk materials are constructed and the corresponding structural factors affecting macroscopic performance remain debatable.

This review attempts to address the following questions: What are the hierarchical structures constituting silk materials? Do the existing models accurately describe the structures of silk fibers, and other forms of non-fibrous silk materials?

Dr. W. Qiu, Dr. A. Patil, F. Hu, Prof. X. Y. Liu
Research Institution for Biomimetics and Soft Matter
Fujian Key Provincial Laboratory for Soft Functional Materials Research
College of Physical Science and Technology & College of Materials
Xiamen University
Xiamen 361005, P. R. China
E-mail: phyluxy@nus.edu.sg

F. Hu
Advanced Soft Matter Group
Department of Chemical Engineering
Delft University of Technology
Van der Maasweg 9, Delft 2629 HZ, The Netherlands

Prof. X. Y. Liu
Department of Physics
National University of Singapore
2 Science Drive 3, Singapore 117542, Singapore

 The ORCID identification number(s) for the author(s) of this article can be found under <https://doi.org/10.1002/sml.201903948>.

DOI: 10.1002/sml.201903948

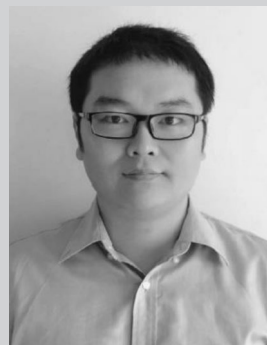
How many levels of structures can be identified from different forms of silk materials, and how can different levels of structures synergistically affect the performance? This review shall provide a fundamental, refined description of the hierarchical network structures of silk materials in a bottom-up manner, which will enable us to investigate the above-mentioned topics comprehensively. Moreover, the correlation between structure and performance will be discussed accordingly. **Figure 2** shows a brief timeline of the “silk road” with regard to the meso-structure, mechanical performance, self-assembly mechanism of silk materials. In 12, we will first investigate the different levels of hierarchical structures of silk materials, and discuss how they can be correlated to mechanical strength. Then, we will introduce several structural characterization techniques in 23. In 34, to illustrate how silk materials are self-assembled, we will enumerate upon previously reported models and put forward a hierarchical network structural model based on comprehensive observations and detailed experimental verification. Meanwhile, the relevant factors associated with silk fibroin (SF) molecule crystallization conditions are also discussed. In the last section, we will explain how the enhancement of macroscopic performance of silk materials (including silk fibers, hydrogels, films, and scaffolds) can be achieved by mesoengineering the hierarchical network structures in terms of controlling nucleation.

2. Hierarchical Mesoscopic Network Structure of Silk Materials in Correlation with Macroscopic Performance

2.1. Models of SF Fibers

The mechanical performance of silk fibers is largely determined by the fibers' unique hierarchical structures. To obtain a comprehensive understanding of the correlation between structure and performance, and synthesis strategies that enhance mechanical properties, we need to conduct a multilevel systematic study. Considerable efforts have been made over the past few years to obtain structural data at the nanoscale and mesoscale levels, which form the basis of functioning of silk fibers at the macroscale level, several structural models have been proposed and developed rapidly.^[11,14–19]

In the early stage, a 1) semicrystallite (bulk network) model based on polymer physics was first put forward.^[16,20] As illustrated in **Figure 3a**, this model considers spider dragline silk fiber to be a composite material, in which the crystalline regions are embedded into an amorphous matrix (made of rubber-like chains). Notably, the crystalline regions (mainly referred to as stiff β -sheet crystallites with a strong modulus) serve as multifunctional cross-links and cause silk fibers to have great strength, whereas the non-crystalline regions (amorphous matrices) are responsible for the excellent elasticity. To some degree, this model can successfully reproduce the complex stress–strain curves of silk fibers through molecular dynamics simulations that are consistent with the experimental data. However, according to the simulation parameters, the modulus of these β -sheet crystallites was as



Wu Qiu received his Ph.D. degree in biophysics from the National University of Singapore (NUS) in 2016 and is now doing his postdoc research in Xiamen University under the supervision of Prof. Xiang Yang Liu. His current scientific interest is focused on the crystallization mechanism and functionalization of silk fibroin-based supramolecular materials.



Xiang Yang Liu received his Ph.D. degree with the cum laude title from the Radboud University Nijmegen (Netherlands) in 1993. He is a tenured full professor in NUS, and the State Distinguished Professor, Chair Professor of the Changjiang Scholars Program. His research interests range from biomimetics, crystallization, biomimetics, flexible materials, flexible election etc.

high as 160 GPa; this value greatly exceeded the value observed during X-ray diffraction (XRD) experiments. Besides, this model is simple and only takes the nanoscale molecular level structures of silk fibers into account. A 2) “cylindrical fibril” model has been reported to exist within the framework of mesoscopic multilevel architecture, based on the observation of fibrils (with a diameter ranging from 90 to 170 nm) on the surface of both spider and silkworm cocoon silk fibers.^[17,18] In comparison to the bulk network model, the “cylindrical fibril” model explains the mechanical performance of silk fibers from a mesoscale point of view. Owing to the interactions between adjacent fibrils, the loading stress can be efficiently dissipated; thus, the strength of the fibers is enhanced. However, according to the 3) “micellar” model,^[14,19,21,22] the fibril-like morphology of the fiber surface should arise from the coalescence and elongation of micellar structures. This model assumes that nanoglobule micelles (with a diameter of ≈ 100 nm) are the basic microstructural building units of silk fibers, instead of fibrils. Recently, these assumptions are found to be debatable, because of the latest findings that show the presence of numerous, significantly thinner (≈ 30 – 50 nm), helically twisted nanofibrils along the fibrous axis of the fiber surface.^[11,23–25]

As discussed earlier, the outstanding mechanical performance of silk fibers is synergistically determined by the different structural levels. However, all the models discussed above provide incomplete information. Because silk fibers consist

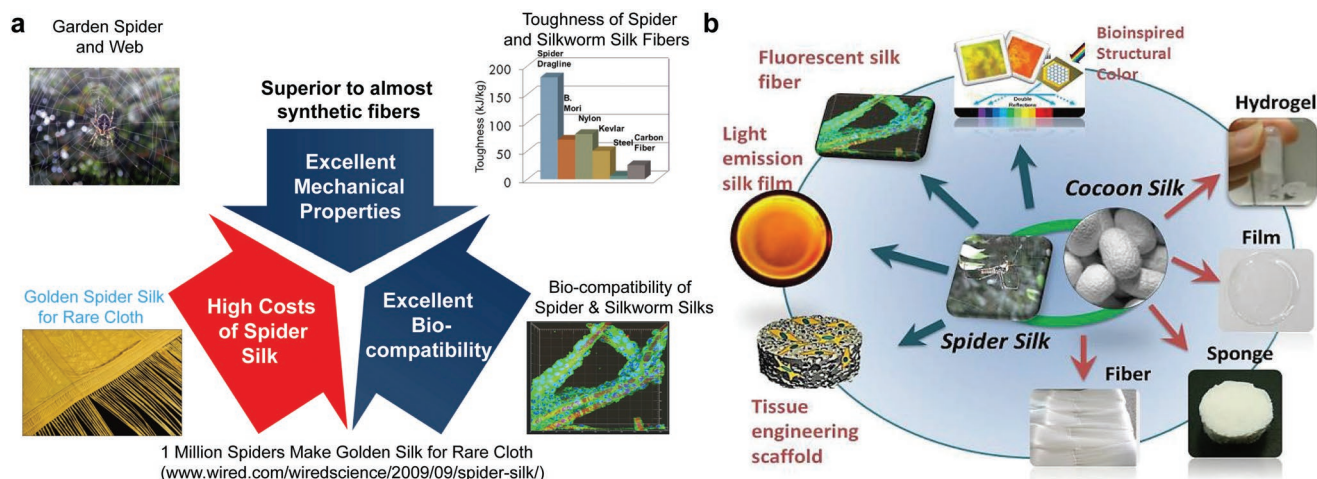


Figure 1. Spider silk and silkworm silk fibrous materials are well known for the unique properties, that is, excellent biocompatibility, heat conductivity, electric insulating capacity, controllable dissolution, and wide optical window (260–2600 nm). Nevertheless, the relatively high cost greatly limits their application. Reproduced with permission.^[25] Copyright 2015, Wiley-VCH. b) Various forms of silkworm cocoon silk and spider silk. Both spider and silkworm silk materials and the applications: silk hydrogels, films, and sponges, used to apply to tissue engineering, and biocompatible, optical, and electronic flexible devices. Reproduced with permission.^[10] Copyright 2015, Royal Society of Chemistry.

of numerous crystallites, complete information regarding the structure is essential for obtaining further insight into how these crystallites are linked to crystal networks. Typically, at least three molecular crystal networks can exist, including 4) a molecular network that is similar to that observed among amyloid fibrils (“amyloid fibril-like” model),^[11,26] 5) the more ordered slab-segment structure (“slab-segment” model proposed by Oroudjev et al.),^[27] and 6) the fishnet structure, where β -crystallites serve as crosslinkers.^[11] The latest results have ruled out the possibility of the former two models.^[11] Indeed, the strong β -crystallites serving as the nodes in the nanofishnet can reinforce the silk fibers, by sharing external forces among the optimized network. Therefore, the adoption of the fishnet topology in crystal networks is a natural selection process for obtaining silk fibers exhibiting an excellent macroscopic mechanical performance. Details regarding models with different crystal network topologies will be comprehensively introduced in Section 2.2.3.

2.2. Hierarchical Structure of Silk Materials

2.2.1. Primary (Level One) Structure of Silk Materials

The primary structure of silk materials is defined as a sequence of amino acids present within protein molecules. Silkworm cocoon silk fibers are mainly reported to be comprised of two basic structural proteins, that is, fibroin and sericin proteins. Notably, the sericin proteins located outside the fibroin proteins act as the glue that brings the two fibroin brims together. The sericin proteins are hydrophilic and can be removed easily by boiling the fibers in hot water. However, the fibroin proteins are mostly hydrophobic and can be further divided into two main categories based on the molecular weight as the light (L) and heavy (H) fibroin chains, with a molecular weight of ≈ 25 and 350 kDa, respectively. The L and H chains are linked together via a single disulfide bond at the C-terminus,

and consequently form the H-L complex.^[28] The H-chains of SF materials are generally responsible for the extraordinary mechanical performance, as they can self-assemble into discrete β -sheet crystallites (β -crystallites).^[10,11] L-chains play a much less important role, because their sizes are significantly smaller than that of H-chains; besides, no L-chain amino acid sequences are reported been observed in the crystalline region.

The H- and L-chains are composed of 5263 and 266 amino acids, respectively. Specifically, the H-chain is primarily comprised of the three simplest amino acids, that is, glycine (G) ($\approx 43.5\%$), alanine (A) ($\approx 28\%$), and serine (S) ($\approx 12.3\%$). Besides, nearly 5% of tyrosine (Y) is also observed to be present (cf. **Figure 4a**).^[29,30] Apart from the above four amino acids, the next most abundant amino acids include valine (V), aspartic acid (D), phenylalanine (F), glutamic acid (E), threonine (T), and isoleucine (I); however, in total, all these amino acids are present only in small amounts, that is, less than 2%.^[30]

In terms of amino acid organization, the SF H-chain is determined to be a regular biopolymer; it consists of 12 large hydrophobic domains (also denoted repetitive domains, named R01–R12) that are intervened by 11 smaller hydrophilic domains (denoted non-repetitive amorphous domains, named A01–A11).^[30] Further insight into these hydrophobic domains reveals that they are composed of dipeptide units in the form of glycine-X (GX), where X can be alanine, serine, tyrosine, valine, or threonine. Specifically, the hydrophobic domains can be divided into four distinct subdomains, including the GAGAGS repeats, GAGAGY repeats, GAAS tetrapeptides, and irregular sequences.^[31] Statistically, the hexapeptide GAGAGS and GAGAGY repeats are the most abundant; they are present in 433 and 120 copies, respectively, altogether accounting for 72% of all the overall repeat dipeptides.

It is reported that these four subdomains play distinct roles. For instance, the $(GAGAGS)_n$ repeats are the main units constituting β -sheets,^[32–34] and are the only units that can organize themselves into the well-defined β -sheet crystallites (β -crystallite). However, no well-defined crystalline structures

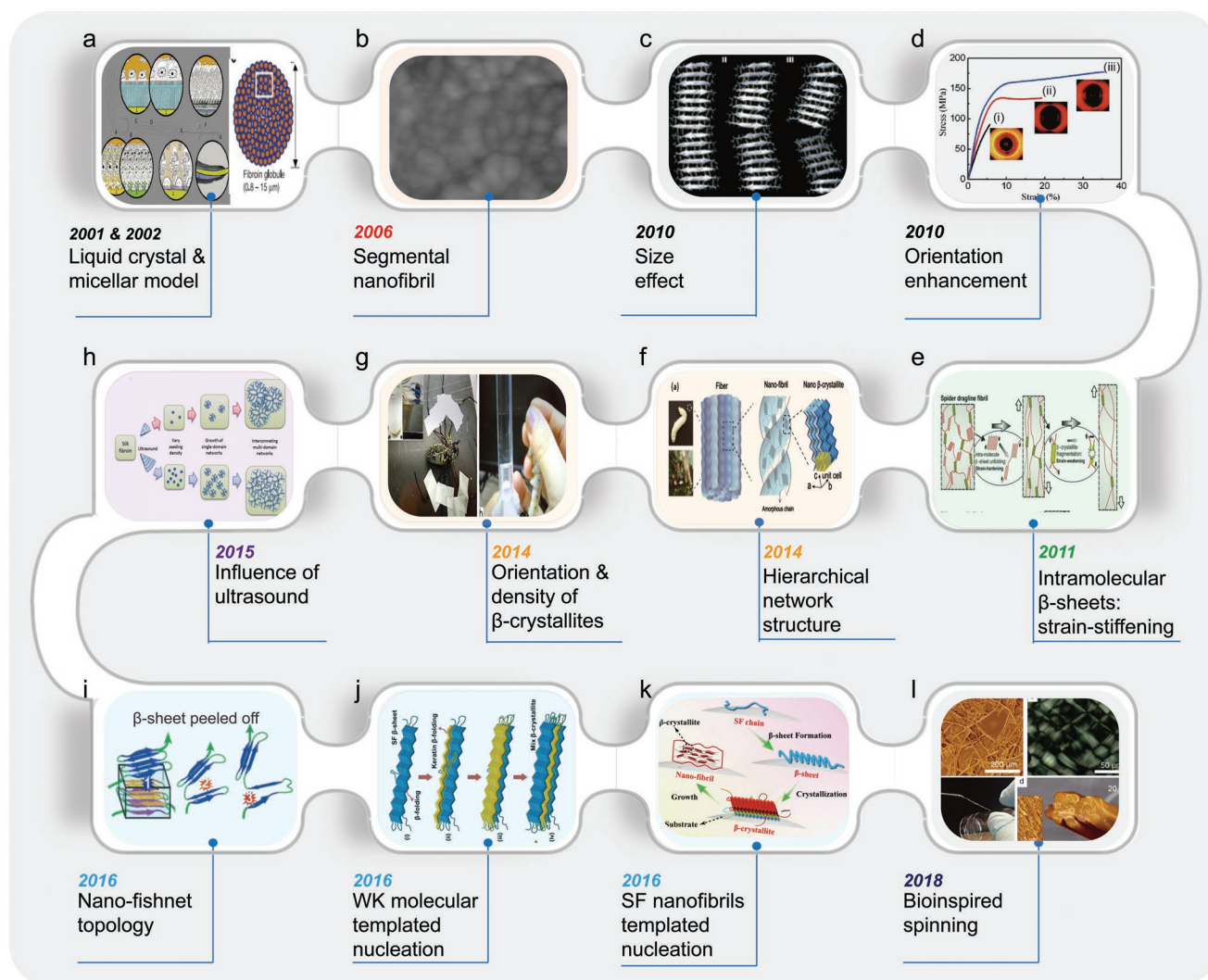


Figure 2. The “ β -sheet”-like brief timeline of main silk research with regard to the mesostructure, mechanical performance, self-assembly mechanism of silk materials. a) Reproduced with permission.^[1] Copyright 2002, Springer Nature; Reproduced with permission.^[2] Copyright 2002, Springer Nature. b) Reproduced with permission.^[46] Copyright 2006, Elsevier. c) Reproduced with permission.^[44] Copyright 2010, Springer Nature. d) Reproduced with permission.^[104] Copyright 2010, American Chemical Society. e) Reproduced with permission.^[24] Copyright 2011, Wiley-VCH. f,g) Reproduced with permission.^[23] Copyright 2014, Royal Society of Chemistry. h) Reproduced with permission.^[25] Copyright 2015, Wiley-VCH. i) Reproduced with permission.^[11] Copyright 2016, Wiley-VCH. j) Reproduced with permission.^[28] Copyright 2016, Wiley-VCH. k) Reproduced with permission.^[12] Copyright 2016, Wiley-VCH. l) Reproduced with permission.^[88] Copyright 2017, Springer Nature.

have reportedly been formed by GAGAGY repeats yet. Although some evidence indicates that GAGAGY repeats might form “ β -crystallites,” the structural units (especially the intersheet distances) within such “ β -crystallites” are significantly different from the ones formed by (GAGAGS)_n repeats.

GAAS tetrapeptides, which are located between the (GAGAGS)_n repeats and serve as β -strand turns, can limit the size of (GAGAGS)_n β -crystallites. Similarly, by forming a loop structure with a distorted Ω shape, irregular sequences can reverse the direction of β -strand backbones, which control crystallite dimensions. Besides, a reversion of the backbone direction might also enable adjacent β -strands to be in contact with each other, to facilitate the occurrence of interstrand interactions. Apart from domestic mulberry *B. mori* silkworms, many other arachnids or insects can also produce silk. Among these,

fibers from non-mulberry *A. mylitta* and *A. pernyi* silkworms and *Nephila* spiders are the most famous and most extensively studied. Irrespective of the sources, all these silk fibers are primarily composed of proteins and have a hierarchical structure that is similar to that of *B. mori* fibers. However, the amino acid sequences of these silk proteins can vary significantly from one species to another, which results in these silk proteins having distinct mechanical properties. Specifically, for the dragline spider fiber proteins in the *major ampullate* (MA), four main amino acid blocks have been identified, including polyalanine (A)_n repeats, glycine-alanine (GA)_n repeats, glycine-rich sequences (GGX, where X is typically tyrosine, leucine, or glutamic acid), and GPGXX sequences.^[35] Among these, the polyalanine (A)_n repeats (which are flanked by (GA)_n repeats) are the most abundant and play a role similar to that of the

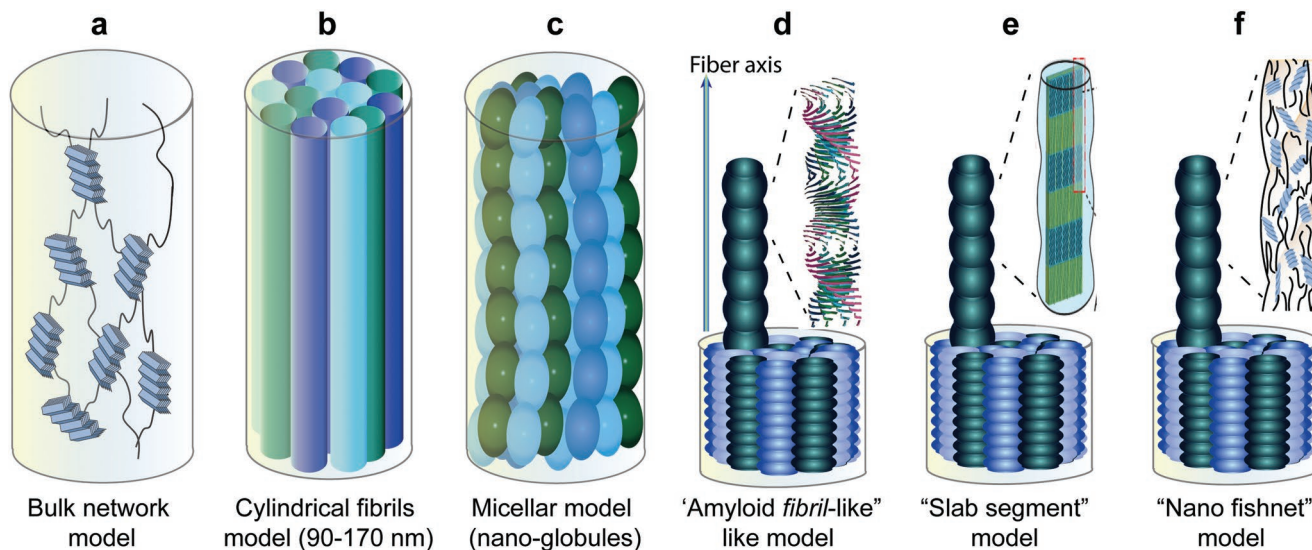


Figure 3. Several models describing the possible mesoscopic structure of natural spun silk. a) Bulk network model; b) cylindrical fibril model; c) micellar model; d) amyloid fibril-like model; e) slab segment model; Reproduced with permission.^[27] Copyright 2002, National Academy of Sciences. f) nanofishnet model.

(GAGAGS)_n repeats in silkworm silk fibers, that is, they are responsible for the formation of β -sheet structures.^[36] The GXG sequences could also possibly participate in the formation of crystalline structures, but such crystalline structures need to be investigated further.^[37] The GPGXX sequences are thought to form β -turn spirals, which are responsible for the excellent elasticity/flexibility of *MA* dragline fibers and capture silk fibers.^[38,39] Recently, the results of quantitative studies have shown that the mechanical properties of *N. clavipes* *MA* fibers are also directly correlated to the proline (P) content; though the initial modulus of spider silk fibers decreases with an increase in the proline content, the elasticity increases.^[40]

A. pernyi silk fibers reportedly present significant differences in both the amino acid compositions and amino acids sequences, as compared to those of *B. mori* silk fibers (Figure 4d). For example, the primary repetitive domains of *A. pernyi* silk fibers are the alternating tandem repeats of the polyalanine motif. In addition, it is confirmed that such polyalanine motifs serve as the structural units for the construction of β -sheet and higher-level structures.

2.2.2. Secondary (Level Two) Structures of Silk Materials

Secondary structure refers to the symmetrical structures by folding peptide chains which are stabilized by hydrogen bondings (H-bond) between the amine and carboxyl groups (the side-chain–backbone and sidechain–sidechain hydrogen bonds are nonrelevant). The most common secondary structural elements are α -helices and β -sheets (Figure 5a). Random coils refer to the multiconformational state of peptides and unfolded proteins and polypeptide chains. Sometimes it is also adopted to describe the unstructured conformations. Notice that random coils are not true secondary structure due to the irregularity.

β -turn, leading to a change in the direction of polypeptide chains, does not belong to certain type of secondary structure by

definition due to structural irregularity. In a β -turn, a hydrogen bond is formed between the backbone carbonyl oxygen of one residue (e.g., the glycine in the sequence of GAAS) and the backbone amide of the residue three positions further along the chain (e.g., the serine in the sequence of GAAS).

Concerning α -helices, the hydrogen bonds form between the oxygen atom of the C=O of each peptide bond in the strand and the hydrogen atom of the N–H group of the peptide bond four amino acids below it in the helix. In this way, the direction of H-bonds is roughly parallel to the α -helices, and the hydrogen bonds help to make this secondary structure especially stable. In comparison, the H-bonds in β -sheet locate between strands (interstrand) rather than within strands (intrastrand). The carbonyl oxygens in one strand hydrogen bond with the amino hydrogens of the adjacent strand (Figure 5a). Similar as α -helix, this hydrogen bonding is the main interaction maintaining the structure of β -sheets. It is noted that although individual H-bond is relatively weaker than covalent bond (e.g., 10–50 kJ mol⁻¹ for H-bond and 250 kJ mol⁻¹ for covalent bonds, respectively),^[41] numerous H-bonds accumulated between strands can greatly reinforce the interactions and thus strengthen the α -helix and β -sheets. On the other hand, although it is revealed that adjacent β -strands can run either in the same direction (parallel arrangement) or in the opposite direction (antiparallel arrangement). The β -sheets in silk materials have naturally chosen the antiparallel β -strand arrangement (Figure 5b). This is because the linear H-bonds (2.76 Å) within antiparallel β -strands are shorter than the non-linear H-bonds (2.97 Å) between parallel β -strands, which consequently results in greater β -sheet stability.^[30]

β -sheets are structurally more compact and stable in aqueous environments, and have stronger mechanical properties than random coils and α -helices. In fact, most molecules within silk materials exhibiting β -sheet conformations (Silk II structure) are more likely to be insoluble. However, when the α -helix conformation plays a dominant role (Silk I structure), such materials can be dissolved easily. In addition, because

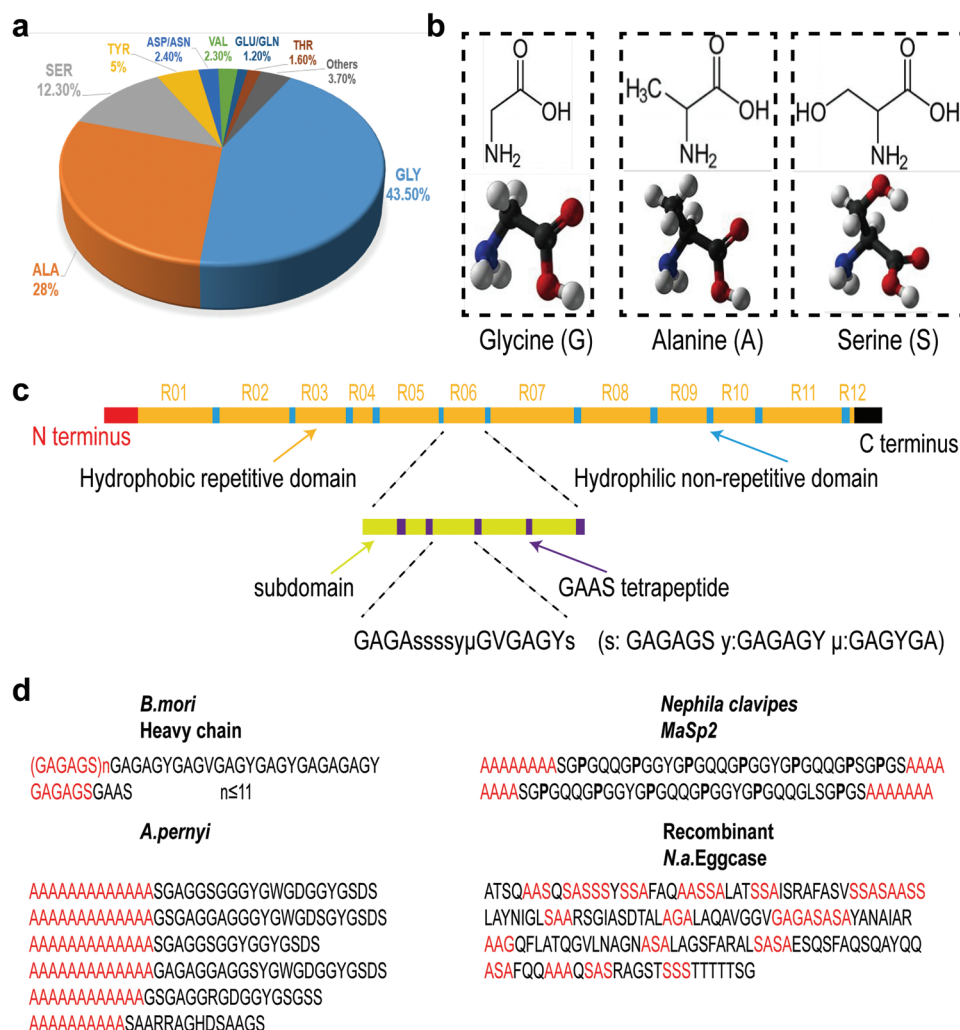


Figure 4. Primary structure of silk materials. a) The amino acid composition of fibroin molecules; b) Illustration of the three most abundant amino acids; c) the amino acid sequence of a fibroin heavy chain. d) Representative repetitive sequences of *B. mori*, *Nephila clavipes* MaSp2, *A. pernyi*, and *N. antipodiana* eggcase silk. The β -sheet constructing units are denoted in red for visual guidance.

α -helices consist of easily movable chains, it is reasonable that a higher α -helix content within silk materials can lead to better extensibility.

2.2.3. Tertiary (Level Three) Structures of Silk Materials and Crystalline Binding Interaction

As mentioned at the beginning, silk materials, in particular, spider dragline fibers, display a very high toughness in terms of breaking energy, this can be to some extent attributed to the occurrence of β -crystallites and the networks. Typically, several secondary structural elements might be used to create a highly compact and organized 3D protein structure, which is known as the tertiary structure. For silk materials, the tertiary structure can be defined as intermolecular β -crystallites (Figure 5c).^[10,11] Specifically, β -crystallites are comprised of several adjacent β -sheets from different molecules, among which hydrogen bonds, hydrophobic interactions/van der Waal's

interactions play a key role in the β -sheet (Figure 5d).^[10,11,30] In this regard, these interactions can also be referred to the "crystalline binding interaction/force." From the point of view of crystallography, β -sheets and β -crystallites can be considered as a sort of polymorphism: if β -sheets are considered as 2D crystals, β -crystallites belong to more stable form of 3D crystals. Although some β -sheets are capable of converting themselves into β -crystallites, it is not necessary for all β -sheets to be converted into β -crystallites. In general, Fourier transform infrared spectroscopy (FTIR) and XRD are the most widely applied characterization techniques, to quantify the total β -conformation and β -crystallite content, respectively. It is noticed that the β -conformation content is always higher than the β -crystallite content as it consists of two types of polymorphism, namely the intramolecular 2D β -sheets and intermolecular 3D β -crystallites. The intramolecular β -sheet content can be calculated simply by deducting the β -crystallite (measured by XRD) content from the gross amount of β -conformation (measured by FTIR or Raman).

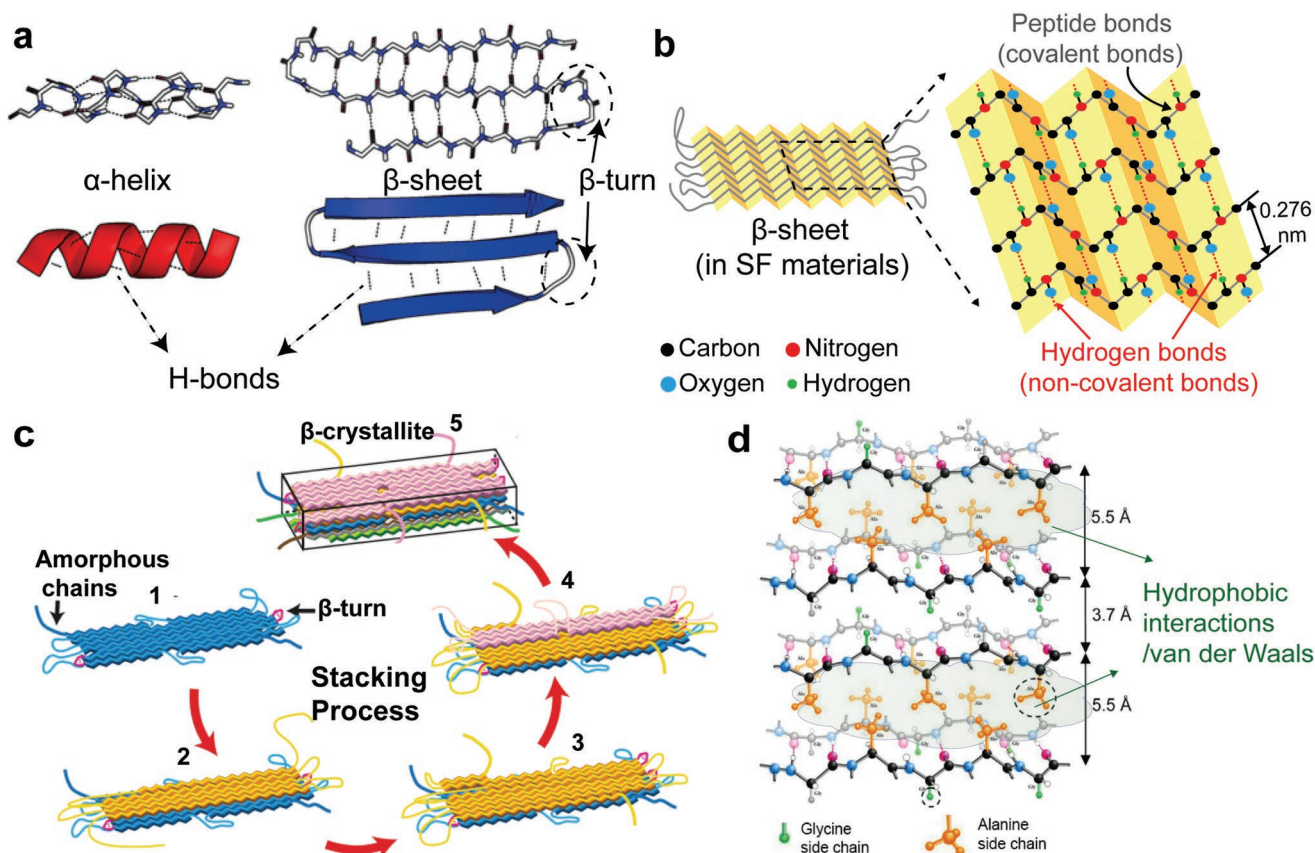


Figure 5. Secondary and tertiary level of structures of silk materials. a) Schematic of two typical secondary structure: α -helix and β -sheet. b) In β -sheets within silk materials, the β -sheets adopt an anti-parallel arrangement. c) Illustration of the process of β -sheets from different molecules stacking into β -crystallite. Reproduced with permission.^[11] Copyright 2016, Wiley-VCH. d) Inside β -crystallites, the main force maintaining the structure of β -crystallites by linking different β -sheet plates are the hydrophobic interactions/van der Waals interactions, especially those between alanine and serine. Reproduced with permission.^[30] Copyright 2015, Elsevier.

Recently, it has been widely accepted that different content of β -sheets and β -crystallites give rise to distinct mechanical properties of different silk fibers. For instance, in spider *MA* dragline silk, the total β -conformation and the intramolecular β -sheet content is 51% and 29%, respectively.^[24] In *A. pernyi* silk fibers, the content of intramolecular β -sheet is 23%.^[42] In comparison to the above two types of fibers with a large amount of intramolecular β -sheet content, *B. mori* silk fibers exhibit a much smaller ratio of intramolecular β -sheet content (9% out of 49%, seen in **Table 1**).^[24] XRD analysis of the β -crystallite structure further confirms that the crystallites within silk fibers exhibit an orthorhombic crystal lattice (with the space group of $P2_21_21$) structure and have unit cell dimensions of $a = 9.2$, $b = 9.4$, and $c = 6.94$ Å, respectively, where a is the direction in which β -sheets are stacked (intersheet distance), b is the direction of a β -sheet that is perpendicular to the strand axis (backbone-backbone hydrogen bonding direction, or interchain direction), and c is the direction of the strand axis.^[24]

Detailed investigation into the structure of β -sheets reveals that the side chains of adjacent β -strands within the same β -sheet plates are the same, that is, the front side of an entire β -sheet projects only the glycine side chains (-H), whereas the back side projects only the alanine (-CH₃)/serine (-CH₂OH) side chains. Above/beneath this β -sheet plate, the

arrangement of the next plate is the opposite; thus, the β -sheet assembly is realized in a front-to-front and back-to-back manner. The side chains are arranged in such a way that the -CH₃ and -CH₂OH groups of opposing β -sheets can be closely packaged; this gives rise to intersheet interactions (Figure 5d).^[30]

We notice that both hydrogen bonding and hydrophobic interactions are much weaker than covalent bonds (Figure 6a).^[41] Nevertheless, if the binding entities are in the form of crystalline state, the binding force can be significantly enhanced: unlike the non-crystalline state where each non-covalent bond/interaction can be broken individually, in the crystalline binding state, the minimal breaking force of binding crystallites is equivalent to the simultaneous breakage of all the non-covalent binding interactions in a critical volume of crystallite. This is due to the fact that the crystallites become unstable if the size of the crystallites is smaller than the critical size. This gives rise to the collectiveness of non-covalent bonds within the volume, displaying much stronger bonding. In this case, although a single noncovalent interaction is weak, the combination of noncovalent interactions can result into a strong bonding case. This will give rise to strong connections and stable binding points of networks in silk materials. In this case, β -crystallization plays a key role in the stabilization of the meso structure of silk protein materials. This is why without

Table 1. Structural parameters of silk fibers.

Sample name	Overall content of β -sheet [%]	Crystallinity [%]	Content of intramolecular β -sheet [%]	Crystallite size [nm] ^{a)}			Reference ^{b)}
				<i>a</i>	<i>b</i>	<i>c</i>	
<i>B. mori</i> cocoon silk	49	40	9	2.3	4.1	10.3	[24]
Spider dragline [10 mm s ⁻¹]	51	22	29	2.1	2.7	6.5	[24]
<i>B. mori</i> cocoon silk	54	41	13	2.5	4.1	9.8	[42]
<i>A. pernyi</i> silk	49	26	23	3.1	3.9	4.0	[42]

^{a)}Crystallites Size along *a* (intersheet direction), *b* (interchain direction), and *c* (fiber axis) axes are measured at 10 mm s⁻¹ reeling speed for dragline silk and 0% strain for *B. mori* and *A. pernyi* silk.; ^{b)}The structural data are taken directly from references.

β -crystallization, silk protein materials are very unstable and highly water soluble.

To acquire a comprehensive understanding of the role of hydrophobic interactions in maintaining the structural integrity of β -crystallite, the strength and number of hydrophobic interactions within different silk fibers are semiquantita-

tively compared. According to the latest simulation results, the strength of ensemble of hydrophobic interactions can be roughly estimated by counting the number of alanine and serine residues per sheet.^[11] Besides, the regularity with which the alanine/serine pattern occurs is also relevant.^[11] For instance, the protein sequence and residues forming β -sheets within *B. mori* cocoon silk (BMCS) and spider *N. antipodiana* eggcase silk (NAES) fibers are shown in Figure 4d. The number of times the alanine/serine pattern occurs within NAES is relatively lower, consequently the probability of occurrence of hydrophobic interactions between β -sheets in NAES is smaller. Hence, the average peel-off force in BMCS fibrils is stronger than that for recombinant NAES fibrils (250 ± 95 pN and 162 ± 49 pN, respectively) (Figure 7b,c).^[11] This difference can further explain why a higher breaking stress (550 MPa) is associated with natural BMCS fibers than with recombinant NAES fibers (256 MPa) (Figure 7d).^[11]

Essentially, apart from inter β -sheet interaction strength, the size of β -crystallites is also an important structural factor that influences the performance of silk materials. The size of β -crystallites in spider dragline silk fibers, *B. mori* silk fibers, and *A. pernyi* silk fibers has been investigated using XRD and are shown in Table 1.^[24,42] The size of crystallites in spider silk fibers, especially along the *c*-directions (i.e., along the fiber axis), is much smaller than that in silkworm silk fibers. To provide insights into the mechanical role of β -crystallites and the correlation between β -crystallite size and mechanical properties of silk fibers, molecular modeling as well as simulations have been adopted. For instance, Wu et al.^[43] has proposed the “ β -sheet (within β -crystallites) splitting” mechanism and found that, upon assuming that this mechanism is used, the predicted stress–strain profiles of silkworm silk fibers are in agreement with the results of experimental measurements. According to their reports, during the silk fiber stretching process, the extension linearly increases with the responsive force in the linear region, until the force reaches a threshold, after which β -crystallites start to split. The splitting of β -sheets (within β -crystallites) results from the breakage of H-bonds, and assuming that the occurrence of H-bonds (along the β -strands) is uniform everywhere, a larger amount of force is required to extract longer molecules from β -crystallites, because more H-bonds must be broken.^[43] In other words, if the fibrous axis (the *c*-direction) of a β -crystallite is larger, such crystallites become more robust. However, the beneficial effect attributable to crystallite size in the *c*-direction (i.e., the L_c) on the mechanical stability is limited. On the contrary,

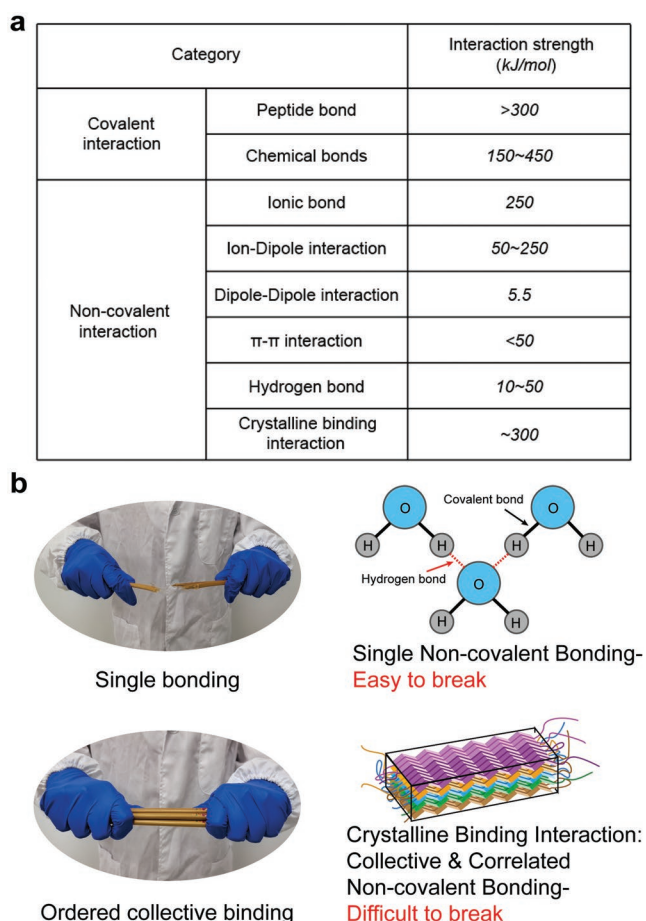


Figure 6. Summary of variety of interactions involved in sf materials and enforcement strength in crystallization (crystallization force). a) Table of interaction strength of different categories of interactions. The method estimating the strength of crystalline binding interaction is present in Note S1, Supporting Information. b) Illustration of the strength enforcement due to β -crystallization, which is subject to collective interactions from correlated hydrogen bonding between neighboring β -strands and hydrophobic interaction among the adjacent β -sheets within β -crystallites.

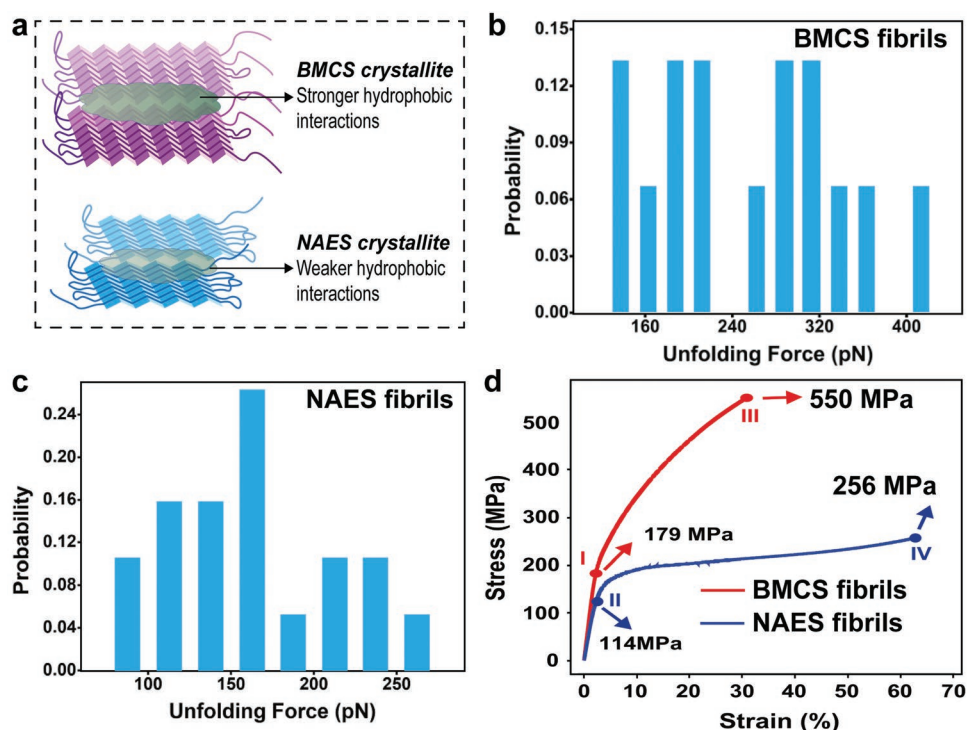


Figure 7. Mechanical properties of *B. mori* cocoon silk (BMCS) and spider *Nephila antipodiana* eggcase silk (NAES) fibers. a) Schematic illustration showing that the hydrophobic interactions within BMCS fibers are stronger than those within NAES fibers. b,c) Statistical results showing the force required to peel off a β -sheet plate from β -crystallites of regenerated BMCS and recombinant NAES fibrils, respectively. The average unfolding force values are 250 ± 95 pN and 162 ± 49 pN. d) Typical stress–strain profiles of natural BMCS (red) and recombinant NAES (blue) fibers. The BMCS fibers are much stronger during the application of breaking stress. Reproduced with permission.^[11] Copyright 2016, Wiley-VCH.

Xu et al.^[23] have proven that if the crystallite size L_c is larger than 6 nm, the influence of size on the splitting force becomes negligible (Figure 8b). In natural fibers obtained from either the silkworm or spider, the measured L_c values are more than 6 nm (Table 1). Thus, the splitting force of β -crystallites in silk materials should not be correlated to the crystallite size along the c -direction.^[23] However, Keten et al.^[44] performed a series of large-scale MD simulations to investigate the effects of crystallite size (in the b -direction) and reported that small β -crystallites with a size of only a few nanometers can give rise to the highest strength, stiffness, and toughness, as compared to large β -crystallites, as shown in Figure 8c,d.^[44] According to the results of their simulation study, in the crystal network, if the length of β -crystallites is 2–4 nm along the interchain direction (L_b), the mechanical properties are optimal.^[44] This experimental finding is in accordance with the reported results for β -crystallites in spider MA dragline fibers; the strength and toughness of spider dragline fibers are enhanced when the β -crystallite size is reduced from 10 to 6.5 nm, and further reduced to 3 nm. This can be attributed to the difference in geometry and stress distribution pathways of small and large β -crystallites. For large crystals, the hydrogen bonds are directly stretched because of tension (i.e., the β -crystallites are pulled in a direction parallel to that of the hydrogen bonds) (cf. Figure 8e, bottom). In contrast, for small crystals that can be deformed when exposed to shear forces, hydrogen bonds are pulled orthogonal to the bonding direction (cf. Figure 7e). This shear deformation pathway can optimally utilize hydrogen

bonds and consequently lead to a significant enhancement in the mechanical strength of β -crystallites.^[44]

From another perspective, compared with smaller crystallites, larger crystallites should contain more defects/mismatches, which also deteriorate the stability. As per the crystallization theory, the formation of large crystallites normally relies on the package with a certain degree of ordering or symmetry.^[10] During the normal crystal growth process, crystallites grow together via self-epitaxial nucleation, which consequently results in an ordered assembly. Nevertheless, under some specific conditions (e.g., when the supersaturation is so high that the nucleation barrier for mismatched epitaxial nucleation decreases rapidly), some mismatches may occur between the parent crystals and nucleating layers of crystals. In this regard, the newly deposited layers of growing crystals would deviate from the optimal structural match position and mismatched/misaligned structural packing would be observed.^[10]

2.2.4. Level Four Structure of Silk Materials: Fishnet-Like Crystallite Networks and Nanofibrils

Merely crystalline binding is insufficient to build up tough materials. To have a tough material depends to a large extent on how these β -crystallites are connected. This is then associated the forth level of structure: β -crystallite networks. In general, the quaternary structure of a protein should refer to complexes composed of multiple subunits. The molecular β -crystallite

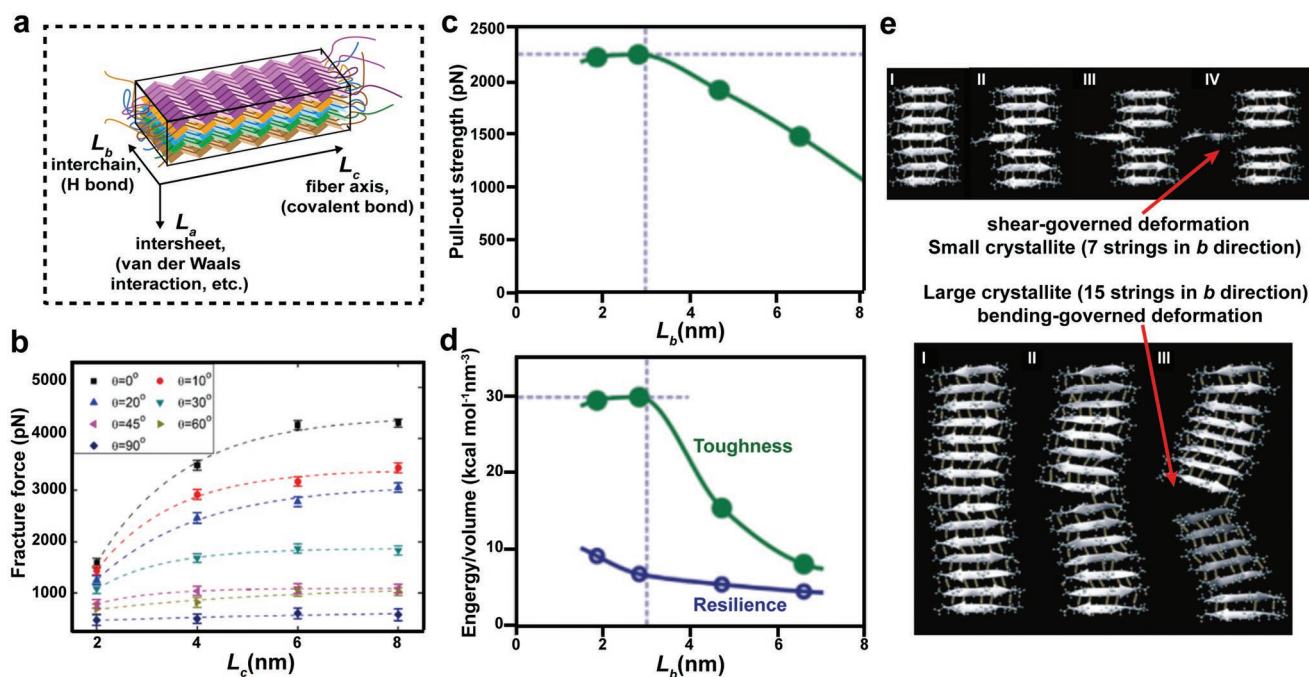


Figure 8. Effect of size on the mechanical performance of silk fibers and failure mechanisms of β -crystallites. a) Schematic illustration of the crystallite and the definition of size along three directions. b) The splitting force of a β -crystallite as a function of the size of β -crystallites along the c -direction, L_c , and its orientation angle θ . a,b) Reproduced with permission.^[23] Copyright 2014, Royal Society of Chemistry; c) strength. d) Toughness and resilience of β -crystallites as a function of crystal size along the b -direction. Toughness is calculated as the area under the force–displacement curve, while resilience is defined as the energy stored just before the initial rupture of hydrogen bonds. e) During pull-out simulations (lateral loading), smaller ($L = 2.83$ nm) and larger ($L = 6.56$ nm) crystallites show shear-governed deformation and bending-governed deformation, respectively. c–e) Reproduced with permission.^[44] Copyright 2010, Springer Nature.

networks of silk materials can be defined as a fourth level structure.^[10,11,23] Notably, each individual nanofibril is a crystallite network, in which amorphous chains link the crystallites together. In this regard, we can also regard nanofibrils (crystal network) as level 4 structures. Nanofibrils are observed in all forms of silk materials (including fibers, hydrogels, films, and scaffolds), convincing that nanofibrils are the basic mesoscopic structural units of the hierarchical structure of silk materials.

As mentioned in Section 2.1, three main types of crystal network topologies can exist. Recently, atomic force microscopy (AFM) is being used to examine the nanostructures of nanofibrils, by measuring the corresponding nanomechanical performance. By combining AFM topography (Figure 8a), SAXS, FTIR, and XRD spectra of SF nanofibrils, obtained from regenerated SF (RSF) solutions and natural SF fibers, Liu et al.^[11] confirm that the structures of the RSF solutions and natural SF fibers are highly similar, which enable the use of individual RSF nanofibrils as an effective surrogate for natural SF fibers. Afterward, they further use the regenerated nanofibrils to verify the type of topology of the β -crystallite network, using AFM force spectroscopy.^[11] By studying the unfolding force patterns of β -crystallites, Liu et al. hypothesize about the mechanism by which the breakage of β -crystallites occur during stretching and conclude that the β -crystallites are associated with each other in the “nanofishnet” topology.^[11] In the AFM force spectroscopy experiments, the AFM tip is used to pull out individual nanofibrils, to probe the elasticity of β -crystallites. The manner in which the silk protein chains are connected via β -crystallites

can significantly affect the dissipation of force from the AFM tip among the semicrystalline networks; this is reflected by the measured force patterns. Typical saw-tooth patterns are observed in the force versus extension trajectories of regenerated nanofibrils. In these force patterns, the height of the force peaks corresponds to the strength of the hydrogen bonds between β -strands in the β -sheet and/or the inter- β -sheet interactions in β -crystallites, while the changes in the level of extension between two adjacent peaks correspond to the released length of the polypeptides (contour length changes can be determined by fitting data to the worm-like chain model). The aforementioned saw-tooth patterns of SF nanofibrils are distinct from the characteristic plateau force pattern observed for amyloid fibrils,^[26] indicating that the molecular network structures within amyloid fibrils and SF nanofibrils are different. This disparity between amyloid fibrils and SF nanofibrils is also observed while examining the XRD spectra; the β -strands in crystallites are aligned along the fibrous axis in silk fibers but are perpendicular to the long axis of amyloid fibrils. Statistical results show that most force–extension curves (94%) of RSF nanofibrils exhibit sequential unfolding events involving random peak forces; no clear trend is observed. However, for the rest of the trajectories (6%), another characteristic pattern is identified.^[11] The highest unfolding force peak is followed by a series of events, which shows a general upward trend in unfolding forces. It is known that hydrogen bonds between β -strands and hydrophobic interactions between β -sheet layers are responsible for the stability of β -sheets

and β -crystallites, respectively. Two possible pathways for unfolding β -strands from β -crystallites can be activated. Pathway 1 involves the sequential unzipping of β -strands directly from a β -crystallite (without affecting the inter- β -sheet interactions), while pathway 2 involves the peeling of a β -sheet off the crystallite, followed by the unzipping of β -strands from the peeled off β -sheet. In the first pathway, at each step of unzipping of β -strands, the force is mostly applied onto the strand directly connected to the AFM tip, whereas an equal amount of force is exerted on the other strands in the β -crystallites, due to the integrated response of β -crystallites. Hence, the strands directly linked to the AFM tip should experience a force much stronger than elsewhere so that they are unzipped in prior. This is then repeated for the next adjacent strand. As the strength of collective hydrogen bonding between different β -strands is different, the corresponding force pattern should result in peaks with different heights. According to the slab-segment model, the force distribution among β -strands in the β -sheet is similar to that in β -crystallites; hence, the force pattern should be similar to the first pathway.^[27] However, if the β -crystallites are cross-linked with each other, as seen in a “fishnet” network, the peeled-out β -sheet are stretched out between two anchor points, that is, the AFM tip and the remaining β -crystallites. In this condition, an equal amount of stretching force is applied on all the β -strands within the peeled-off β -sheet, because they are connected in a series. Thus, the weakest β -strands turn to be unzipped first, followed by others in the order of strength.^[11] This can explain the existence of the 6% trajectories. Further, Liu et al.^[11] carried out a series of simulations to compare the relative strength of networks according to the two pathways. The simulation results confirm that both the possibility of use of each pathway and change in the contour length of a β -sheet being peeled off from β -crystallites in the case of a fishnet structure are in agreement with the AFM results.^[11] This again proves that β -crystallites in the SF nanofibrils are crosslinked, in order to ensure that fishnet-like molecular networks other than the amyloid-like and slab-segment structures are adopted. Furthermore, it is reported that a similar force pattern for recombinant spider eggcase silk fibrils has been observed, suggesting the prevalence of the molecular fishnet structure in animal silk nanofibrils of different types (Figure 9e).^[11] It is noted that adoption of such “fishnet” structure is the natural choice of silkworm and spider dragline fibers for obtaining outstanding toughness of crystallite network. In fact, by Monte Carlo approach to simulate breaking stress of different network structures, it is calculated that the fishnet structure can stabilize long silk fibers at a substantially reserved mechanical strength, which has greatly surpassed the breaking force predicted within the model of entangled amyloid fibril model and no friction strings model (seen in Figure 9f).^[11]

Several types of crystallite patterns can be observed within the framework of the “nanofishnet” crystal network topology. For example, while β -crystallites can be effectively oriented adjacent to each other along the fibrous axis, they can also be oriented in a direction that is perpendicular to the fibrous axis (Figure S1, Supporting Information). Recently, it has been determined that the nanofibrils in natural SF fibers are dominated by parallel- β -sheets, where β -strands are parallel to the fibril axis. However, the cross- β -sheet arrangement, in

which β -strands are perpendicular to the fibril axis, can also exist in some non-fibrous silk materials.^[45] Gong et al.^[45] have reported that silk fibroin materials can be selectively folded into β -sheets in either the cross- β -sheet or parallel- β -sheet arrangement, by incubating SF solutions either quiescently or under a shear force, respectively. It should be noted that shear forces exist during the natural process of spinning of silk fibers. It is reasonable to assume that this shear force plays a dominant role in determining the arrangement of β -strands. Based on this assumption, we have made a series of ex situ attempts to mimic the in situ natural spinning process in silkworm glands, by adjusting the pH, changing metallic ion concentrations, and applying a shear force. Our experimental results show that only the RSF nanofibrils created by shear forces adopt the para- β -sheet arrangement (not published yet). Different β -sheet arrangements might contribute to the distinct performance of silk fibers and hydrogels, because parallel- β -sheets are more regularly patterned along the fibrous axis, consequently they are stronger (1, Supporting Information). Thus, the application of shear force during β -sheet formation might be a promising strategy for the preparation of various non-fiber silk materials with enhanced mechanical properties.

Although β -crystallites are mostly responsible for the outstanding mechanical performance of silk fibers, the intermolecular β -sheet is also equally important and plays a unique role. Specifically, mechanical tests show that both MA dragline fibers and *A. pernyi* silk fibers display unique strain stiffening characteristics.^[24,42] Earlier efforts have confirmed that rich intramolecular β -sheets should primarily contribute to the strain-stiffening effect observed in spider dragline silk fibers.^[24] Recently, the structural origin of the strain-stiffening effect in *A. pernyi* silk fibers is comprehensively studied.^[42] The mechanism of strain stiffening is described as follows:

At relatively low stretching ratios (i.e., less than 5% or before the so-called yield point *S*, shown in Figure 10a), the intramolecular β -sheet content in *B. mori* silk is only slightly decreased.^[24] In comparison, the intramolecular β -sheet content in MA dragline silk and *A. pernyi* silk fibers decreases significantly.^[24,42] In other words, the intramolecular β -sheets (in MA dragline silk and in *A. pernyi* silk fibers) are unfolded prior to the splitting of the intermolecular β -crystallites (Figure 10b,d).^[24,42] This is attributed to the fact that the intramolecular β -sheets show a lower level of morphological perfection and stacking compactness than intermolecular β -crystallites. Thus, the unfolding of intramolecular β -sheets results in the release of the entire lengths of protein chains, which consequently leads to the extension of draglines without causing the breakage of the intermolecular linkage of molecular networks (i.e., the β -crystallites). In terms of macroscopic performance, during the above process (strain less than 10%), the modulus of MA dragline almost drops to zero, as fiber extension is mainly caused by the breaking of weak intramolecular hydrogen bonds within intramolecular β -sheets. Afterward, with the progressive unfolding of fibers, the intermolecular β -crystallites begin to support the load. The dragline fibers become stiffer due to the contribution of the enthalpic component.^[24] This is how strain-stiffening occurs in spider dragline fibers. However, it is further determined that the intermolecular β -crystallites in *A. pernyi* silks are also reoriented and become aligned along

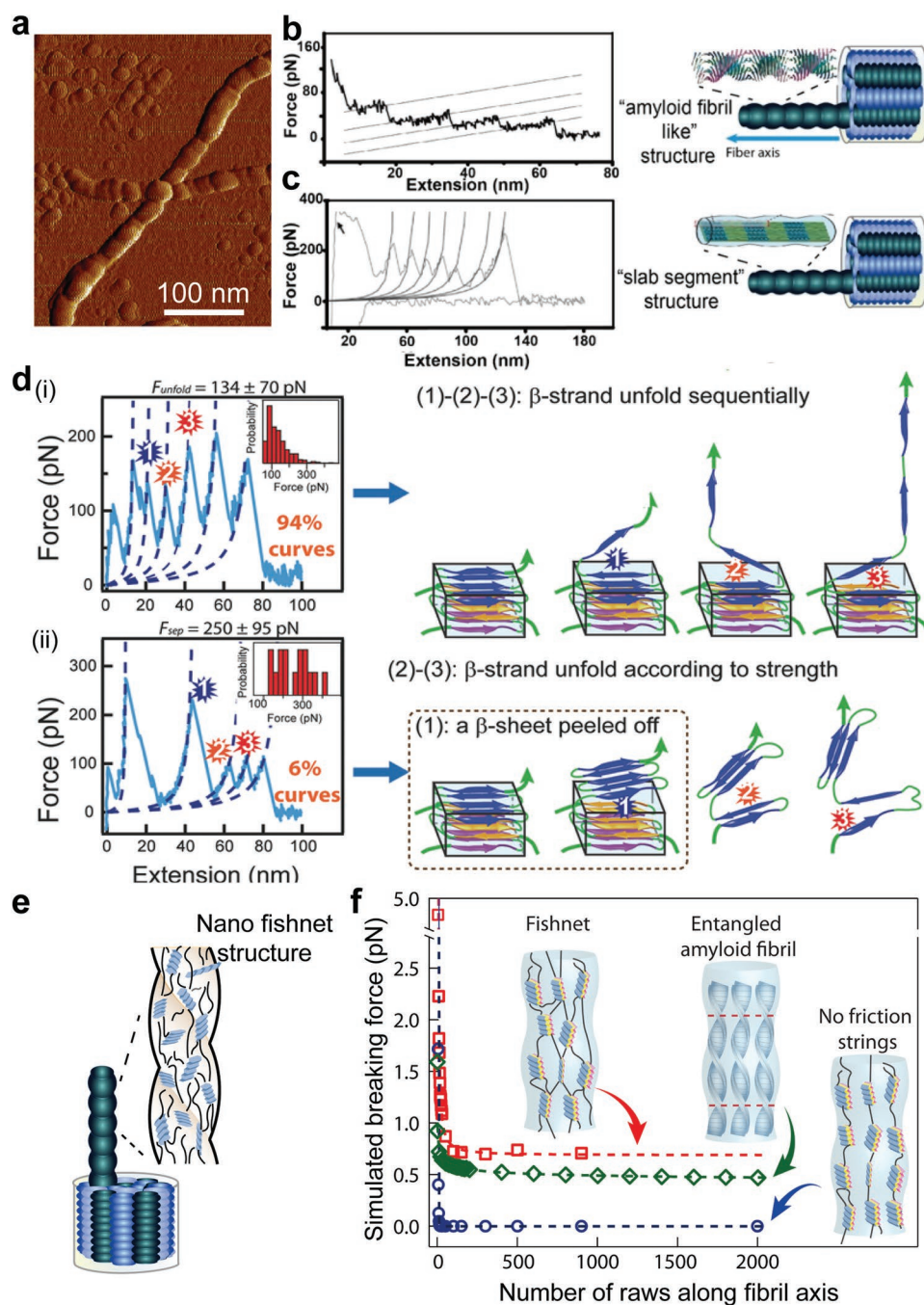


Figure 9. Schema of crystal network of silk materials. a) AFM morphology of regenerated nanofibrils in SF solutions. b) Typical force–extension curves and schematic structure of amyloid fibrils. Reproduced with permission.^[26] Copyright 2006, Elsevier. c) results reported by Oroudjev et al.; the heights of the peaks are random. Reproduced with permission.^[27] Copyright 2002, National Academy of Science. d) Force spectra and the corresponding mechanism reported by Liu et al. Reproduced with permission.^[11] Copyright 2015, Wiley-VCH. e) The molecular fishnet structure of a silk nanofibril. f) Simulated mechanical strength of the fishnet, no friction strings, and entangled amyloid fibril structures of silk fibrils. Breaking forces are plotted as functions of the length of the fibrils, that is, the number of rows along fibrils axis. Insets show the cartoon of the different types of networks. Reproduced with permission.^[11] Copyright 2015, Wiley-VCH.

the fibrous axis (Figure 10d)^[42]; this also contributes to the stiffening of the entire crystal network (Figure 10e). The stretching of fibers beyond the inflection point H will cause a failure in the functioning of β -crystallites. Obviously, demolishing such nodes of the crystal network in fibers results in the weakening

of the fiber (so-called strain weakening). This breakage process has been verified by XRD measurements, which shows that once the spider MA dragline is stretched beyond point H, the β -crystallinity drops immediately (Figure 10b).^[24] *B. mori* fibers with significantly lower intramolecular β -sheet content in the

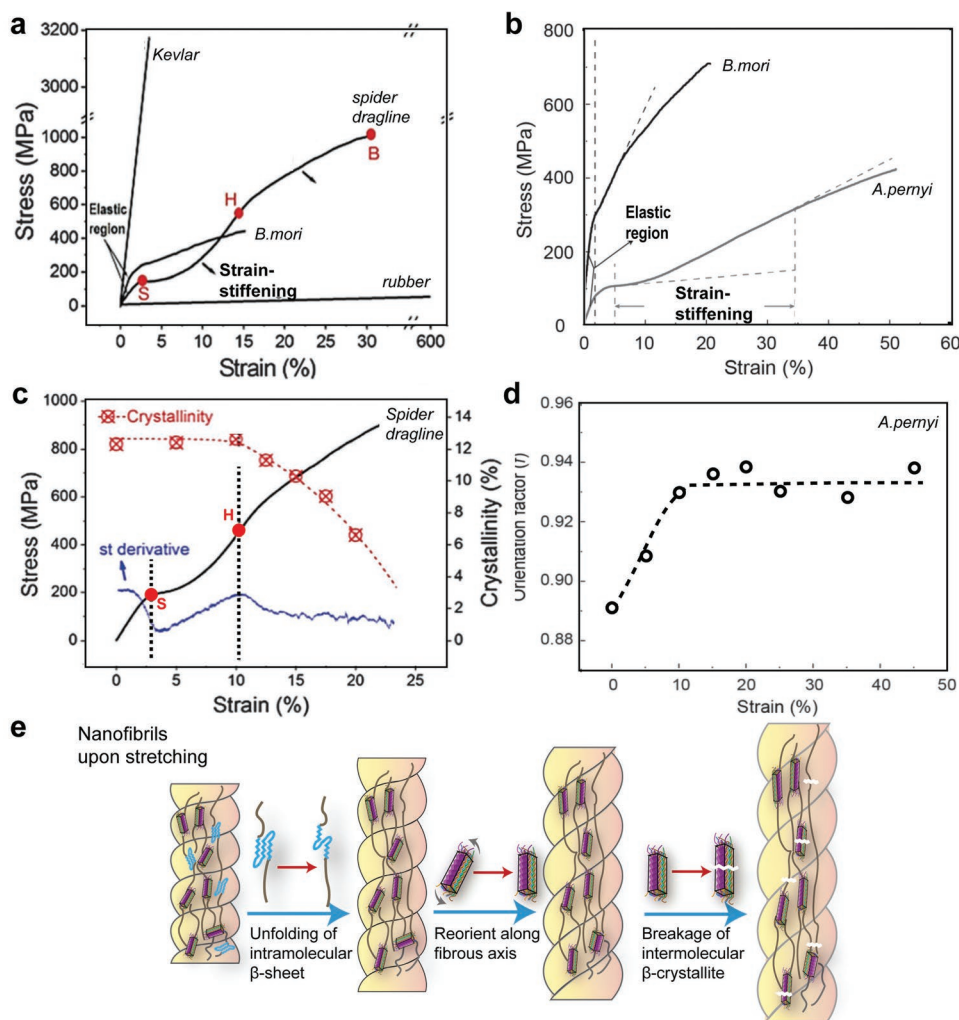


Figure 10. a, b) Typical stress–strain curves of different fibers. The points S and H are denoted as the yield and inflection points, respectively. The strain stiffening effect is only observed for spider MA dragline and *A. pernyi* silk fibers. c) Effect of tensile deformations on the β -crystallinity of spider MA dragline fibers; intramolecular β -sheets unfold prior to the fragmentation of β -crystallites. a, c) Reproduced with permission.^[24] Copyright 2011, Wiley-VCH. d) Variations in orientation functions of *A. pernyi* silk, as a function of strain. e) A schematic illustration of the response to stretched *A. pernyi*/spider MA dragline silk fibers. It consists of three distinct stages, that is, i) unfolding of intramolecular β -sheets, which makes the fiber extensible; this stage is not observed in *B. mori* silk, ii) reorientation of β -crystallites, which enhances the strength of fibers, and iii) the breakage of β -crystallites, which results in the breakage of entire fiber. b,d) Reproduced with permission.^[42] Copyright 2017, Wiley-VCH.

non-crystalline regions (only 9%) have lower extensibility and exhibit only strain-weakening behavior after the yield point (Figure 10a). Thus, it is assumed that if there is a method for increasing the number of intramolecular β -sheets in silk materials, the mechanical property should be reinforced accordingly. However, it should be noticed that the content of intramolecular β -sheets is largely controlled by intrinsic primary structures. As discussed above, the core repetitive motifs forming β -sheet crystallites in *B. mori*, spider MA dragline fibers, and *A. pernyi* silks are (GAGAGS)_n, polyalanine domains, and polyalanine motifs, respectively. Besides, it is confirmed that the (GAGAGS)_n motifs in *B. mori* silk fibers are significantly longer than the polyalanine motifs of MA dragline fibers. The longer lengths of repetitive (GAGAGS)_n sequences can increase the likelihood of the association with each other and consequently lead to the formation of intermolecular β -crystallites, instead of intramolecular β -crystallites. On the other hand, a statistical

comparison of the primary fibroin sequences of *B. mori* and *A. pernyi* further reveals that *B. mori* silk fibroin contains approximately 65% of the repetitive GAGAGS motif, whereas *A. pernyi* contains only approximately 18% of the repetitive poly(A) motif. This difference is attributable to the distinct content and size of intramolecular β -crystallites in *B. mori* and MA silk fibers. Within the framework of the primary structure, the protein sequences might need to be altered to achieve an increment in the intramolecular β -sheet content of *B. mori* silk fibers and silk materials.

The orientation of crystallites is another very important structural factor that determines the crystal networks' mechanical properties. However, although most of the β -strands in crystallites are roughly parallel to the fibril axis, the β -crystallites in the crystal network are still not perfectly oriented. So far, the influence of crystallite ordering on the breaking stress of both silkworm silk and spider dragline silk fibers has been

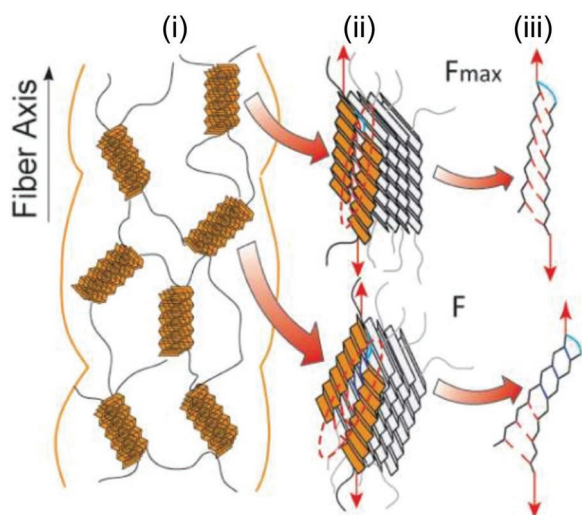


Figure 11. microscopic mechanism of silk yielding behavior and the effect of ordering function of crystallites network. i) illustrates the interspersed β -crystallites in nanofibrils, whose orientations were deviated from those of the fiber axis, ii) illustrates the splitting of β -crystallites in an arbitrary direction, and iii) is a sketch presenting the number of H-bonds involved in splitting dynamics, indicated using red dashed lines. A better alignment along the fiber axis would cause more H-bonds to be recruited to endure the splitting force and consequently give rise to stronger crystalline binding interactions within β -crystallites. Reproduced with permission.^[11] Copyright 2016, Wiley-VCH.

intensively investigated via modeling and simulations, as well as experimental studies.^[11,23] According to the β -crystallite splitting theory, a better orientation of β -crystallites along the fiber axis results in higher breaking stress, because it influences the “effect force” for the separation of β -sheets, as schematically illustrated in **Figure 11**.^[11] In terms of experimental results, it is known that spider dragline silk fibers have a much higher breaking stress than silkworm silk fibers. This is attributed to the fact that natural silkworm silk fibers display a relatively low orientation function $f \approx 0.84$, as compared with spider dragline silk fibers (orientation function $f = 0.93$).^[23,25] However, it has revealed that the mechanical performance of even the silk fibers obtained from the same species can be improved further, by increasing the orientation function value. For example, Liu et al.^[11] have carried out MD simulations to investigate the influence of different orientation functions on the stability of corresponding crystal networks and then compared the simulation results with the experimental results. Notably, the simulated data fits well with the experimental data. Apart from this, the results also show that the breaking stress of both spider and silkworm silk fibers increase with f unambiguously in the same fitting curve after eliminating the influence of other factors.^[11]

Apart from the crystallite orientation function, the density of crystallites is another important structural factor that decides the strength of silk fibers. Evidently, within the framework of the crystal network structure, the fishnet-like topology of this crystal network can further isolate the products of breakage of individual crystallites, by bypassing the loading stress from the broken ones to the surrounding interconnected crystallites.^[11] Consequently, the more β -crystallites participate in load sharing, the stronger the network should be.

Making the comparison between spider dragline silk and silkworm silk fibers, although the crystallinity of spider silk fibers is only half of silkworm silk fibers, given the fact that the size of β -crystallites in spider silk materials is only 1/4th of silkworm silk materials (Table 1), the β -crystallite density in spider silk is still almost double than silkworm silk fibers.^[25] This is in excellent agreement with the fact that spider silk fibers are much stronger.

2.2.5. Level Five Structure of Silk Materials

As discussed earlier, each individual nanofibril is a molecular crystal network. If such nanofibrils are isolated, we can treat each nanofibril as a single, individual domain, whereas the interconnectivity of these nanofibrils causes the formation of a network of nanofibrils, which is regarded as a multidomain system.^[12,23] In principle, the nanofibrils network can be defined as the level 5 structure of silk materials, in which the structural unit refers to the individual nanofibril, and the “links” between neighboring nanofibrils are either formed by strong physical contact (in case of silk fibers) or weak interactions (in case of non-fiber silk materials). It is apparent that the strength (or stability) of the nanofibrils and internanofibril interactions have a great impact on the macroscopic mechanical performance.^[10,12,23] In the subsection 2.2.4, we have described the structural factors affecting the stability of nanofibrils (crystal network), while in this subsection, we will comprehensively study the influence of the strength of interactions between nanofibrils.

Figure 12 illustrates two typical nanofibrils network architectures in silk materials, that is, a) a multidomain system in which the domain–domain interaction is weak or zero; and b) a multidomain system in which the domain–domain interaction is strong or infinite. AFM morphological results have proven that although both silk fibers and SF hydrogels are comprised of numerous nanofibrils, SF hydrogels exhibit a system of weak domain–domain interactions, because the nanofibrils in SF hydrogels are patterned in a disorderly manner and the interactions between fibril domains are relatively weak. However, SF fibers exhibit a system of strong domain–domain interactions, because SF fibers are comprised of a bundle of highly well-oriented, twisted nanofibrils that are interlocked by adjacent nanofibrils, to ensure that the nanofibrils cannot move freely.^[10,12,23]

The above discussion reveals the importance of the helically twisted morphology of SF nanofibrils. We have assumed that this characteristic morphology results from associations between periodically repeating segments. Hence, the breakage of an individual nanofibril should take place at the most loaded “segments.” The fracture of entire SF fibers, which are comprised of numerous nanofibrils, is initiated because of the failure in the functioning of the weakest nanofibrils. However, the “rough” morphology of helically twisted nanofibrils can enable it to effectively avoid mutual slips, even after a critical external force has been applied. This is attributed to the presence of a non-slipping fibril bundle (N-SFB) structure; in addition, strong interactions between nanofibrils consequently give rise to stronger silk fibers.

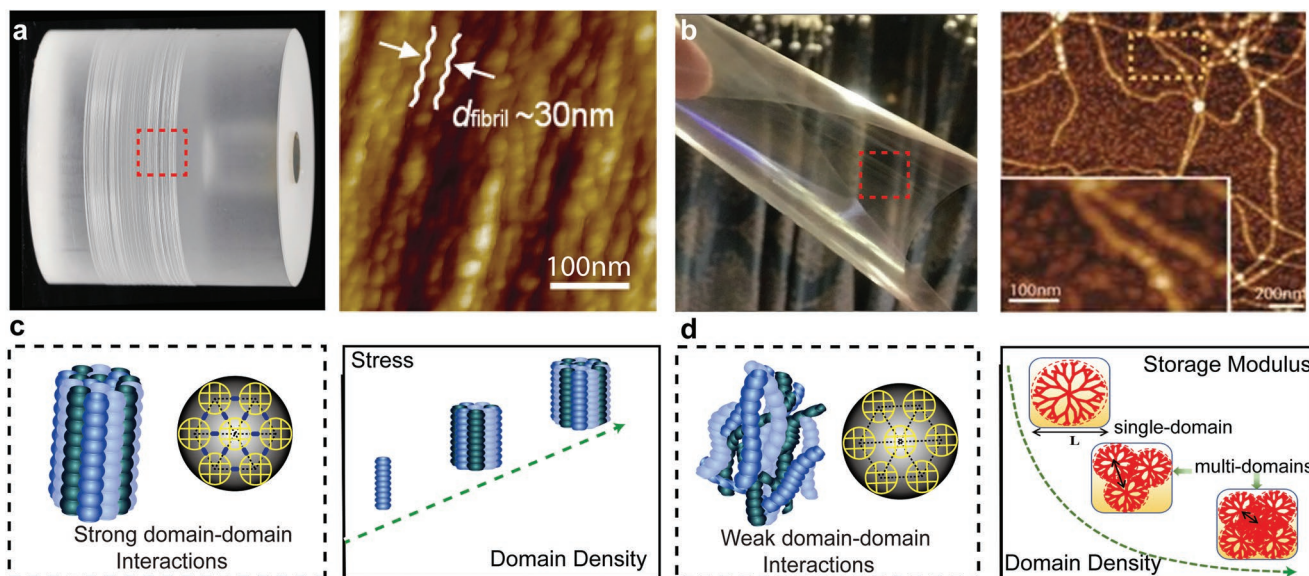


Figure 12. Illustration of the fifth level structure of silk materials. AFM images reveal that sf nanofibrils are helically twisted a) in silk fibers and b) non-fiber silk materials such as SF films. c,d) Illustration of the relationship between mechanical properties and density of nanofibril domains. c) Weak internanofibril interactions. d) Strong internanofibril interactions. a) Reproduced with permission.^[23] Royal Society of Chemistry.

The advantage of this “non-slipperiness” feature of nanofibrils for toughening silk fibers can be demonstrated by comparing these fibers with two other structures, namely, the slippery fibril bundle (SFB) structure and the bulk network (BN) structure. The SFB model assumes that the nanofibrils are smooth and can slip out freely. The BN model assumes

the entire silk fibers to be a bulk molecular crystallite network. Using simulations, the mechanism by which the SFB and N-SFB structures react upon being stretched until breakage and the respective estimated mechanical strength are identified, as demonstrated in **Figure 13a,b**. The manner of breakage of the BN structure is similar to that of brittle materials, and the

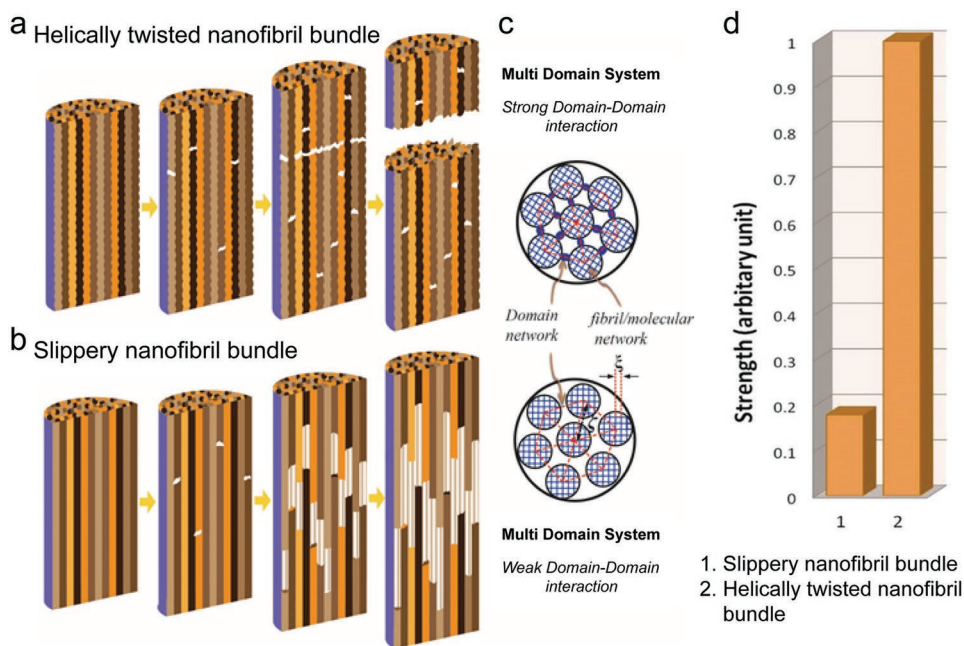


Figure 13. Correlation of nanofibril bundles with the breakage of silk fibers. how sf nanofibrils correlation will determine the breaking pathway and toughness of silk fibers. Schematic illustration of the breakage of silk fibers with a) helically twisted nanofibril bundle structure and b) slippery nanofibril bundle structure. c) The periodic segmental morphology of helically twisted nanofibrils gives rise to frictions, and consequently to strong domain–domain interactions. In comparison, relatively weaker domain–domain interactions are observed in the slippery nanofibril bundle model. d) Comparison of the breaking strength of silk fibers, simulated according to above two models. Reproduced with permission.^[23] Copyright 2014, Royal Society of Chemistry.

emergence of entire fiber fracture results from the catastrophic growth of numerous small cracks. According to Griffith's fracture theory, the extra stress caused by a small crack would mainly cause it to dissipate adjacently, especially at the transverse boundary.^[23] In this regard, within the framework of the BN model, the extra stress are redistributed uniformly in the cross sections that contain cracks. The accumulation of such extra stress can promote the formation of cracks, which finally results in the splitting up of the entire network. In comparison, in the SFB structure model, a bundle of smooth nanofibrils is stretched gradually. As the slipperiness results into weak interactions between neighboring nanofibrils, each nanofibril carries a certain load independently; thus, the breakage of the nanofibril bundle (the entire fiber) begins from the weakest nanofibril. Afterward, the total loads are passed onto the adjacent nanofibrils, which eventually gives rise to the catastrophe of the unbroken nanofibrils, leading to the breakage of entire fiber. The abovementioned process is similar to ductile materials, whose deformation is carried out by localized shear forces at the nanoscale level. The simulated breaking strengths of silk fibers are accordingly plotted in Figure 13d. The SFB fibers are much weaker than those of the N-SFB model. This plot indicates that the non-slippery feature and the bundled structure of nanofibrils affect the strengthening of silk fibers. In the BN model, a crack can easily develop at the weakest position along the transverse direction. However, in the N-SFB model, the boundaries of the helically twisted nanofibrils can physically terminate the growth of such cracks across fibers, and the extra stress can be uniformly redistributed among surviving nanofibrils. On the other hand, in the SFB model, due to the lack of strong friction between neighboring nanofibrils, the cracks can easily occur along the fibrous axis, without any impediments. In summary, the helically twisted morphology of nanofibrils results in strong internanofibril interactions, which further stops the occurrence of cracks in the transverse and longitudinal directions.

Based on the above discussion, there are at least two impressive structural factors in the level 5 structures of silk materials, namely, 1) the periodic segmental morphology of nanofibrils, which prevents adjacent nanofibrils from slipping, and 2) the nanofibril bundle architecture as well as the non-slipperiness between nanofibrils causes the extra stress to be shared equally among the unbroken nanofibrils.

As discussed in Figure 12, nanofibrils either in silk fibers or in SF hydrogels have similar diameters. In addition, most of the structural parameters (including of level 1 to level 4 structures, except the orientation of β -crystallites) are also nearly the same.^[11] However, different types of interactions between nanofibrils are observed in these two level 5 silk materials. Specifically, weak nanofibril–nanofibril interactions are observed in non-fiber silk materials, while strong internanofibril interactions are observed in silk fibers. They both also exhibit different, distinct nanofibrils network architectures. For instance, the nanofibrils in silk fibers are well aligned along the fibrous axis, whereas the nanofibrils in RSF hydrogels are much less ordered or are randomly distributed. Hence, natural silk fibers are much stronger than SF films (measured around 300–400 MPa and 40 MPa for silk fiber and SF films, respectively; see Table S1, Supporting Information).

2.2.6. Summary of Hierarchical Structure of Silk Materials

Based on the structural analyses of silk materials, the extraordinary properties of *N. pilipes* spider and *B. mori* silkworm silk materials are attributed to the five levels of hierarchical network structures illustrated by Figure 14. From the bottom-to-top manner, the hierarchical network structure was identified as the following five levels: (1) amino acid sequence, (2) secondary structure, 3) β -crystallites, 4) crystal networks or nanofibrils, and 5) nanofibrils networks.

Within the framework of the hierarchical structure, crystalline binding interaction is very important in the stabilization of silk materials, while the crystallite networks or nanofibrils and the networks of nanofibrils are two of the most essential structural elements, which to a large extent determine the macroscopic performance of SF materials.

This detailed and comprehensive understanding on the hierarchical structure of silk materials is so crucial that displays the correlation between the macroscopic performance and mesoscopic structure of silk materials, and the identification of effective technologies in materials engineering for silk materials highlighted in this review. As can be seen from this review, based on this model, we can establish the correlation between the mesonetwork structures and the mechanical performance of silk materials.^[11,23,24,46]

3. Methods for Structural Characterization

As discussed in Section 1, an accurate and quantitative method for the characterization of the secondary and tertiary structure content within silk materials is of the utmost importance. In addition, to provide comprehensive insight into the morphology and architecture of the nanofibrils as well as nanofibrils network, advanced imaging techniques are also in demand. So far, a large amount of effort has been devoted to the corresponding techniques development and several characterization and imaging methods have been developed. For instance, the structural characterization methods include FTIR spectroscopy,^[47,48] Raman spectroscopy,^[49,50] circular dichroism (CD),^[51] and X-ray diffraction spectroscopy.^[24] Besides, AFM force spectra also emerges as a powerful tool^[11,52] studying the nanostructures within SF materials. As for imaging, scanning electron microscopy (SEM), transmission electron microscopy (TEM), and AFM are the most popular imaging techniques. In this section, we will provide a brief introduction about the principle and operation of above-mentioned methods, specifically, several typical examples are also presented.

3.1. Structural Characterization Techniques

3.1.1. FTIR Spectroscopy

Owing to its simplicity and practical usage, FTIR is the earliest and one of the most widely applied methods used for studying the secondary structures of proteins. FTIR spectroscopy can be used to obtain information from the infrared spectrum about

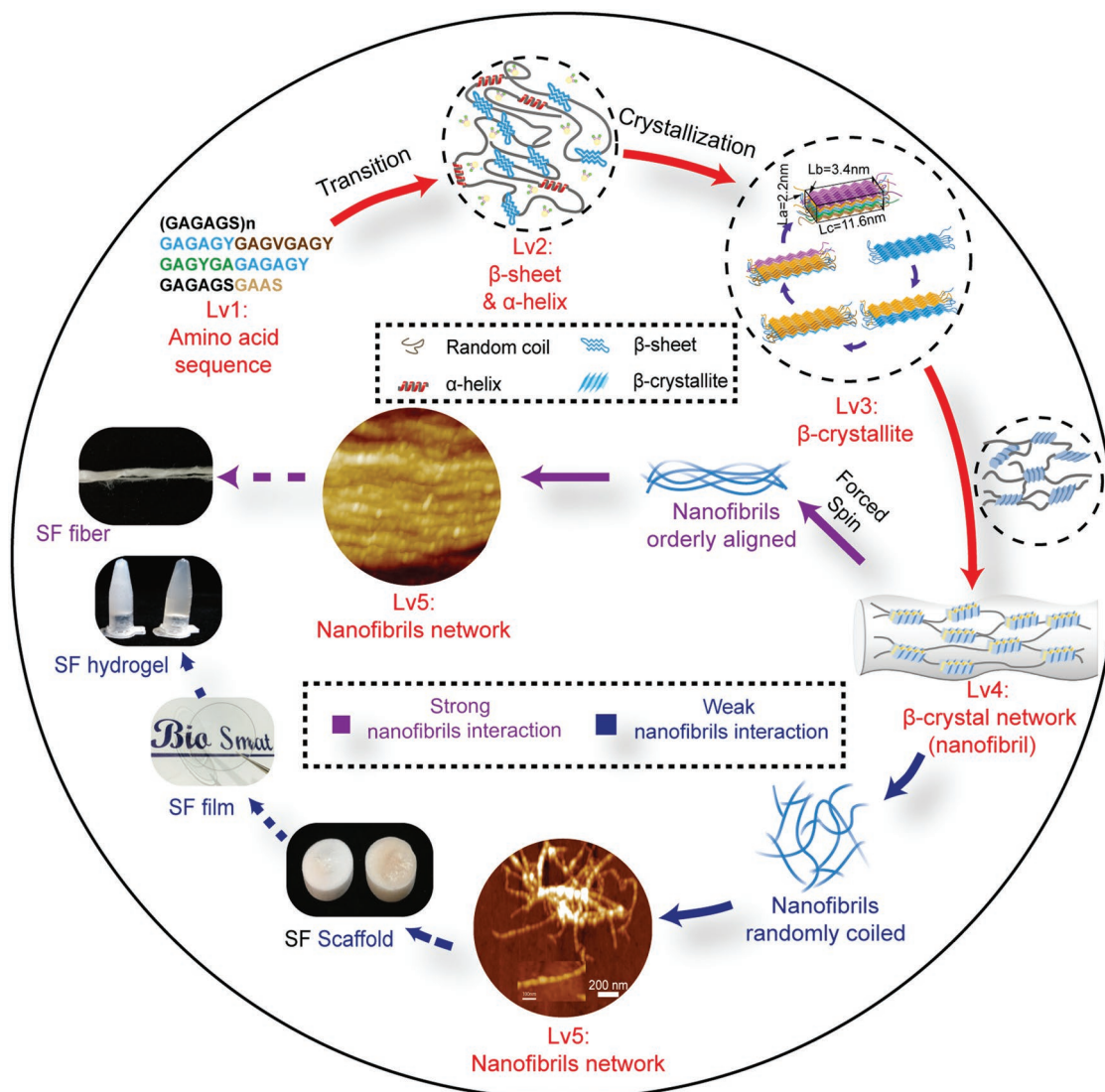


Figure 14. Schema of the hierarchical network structures of sf fibers and non-fiber silk materials. i) lv1-1: the amino acid sequence; ii) lv1-2: α -helix & β -sheet. They are stabilized by intermolecular H-bonds, and β -sheets are crystallized. iii) lv1-3: β -crystallites. The formation is attributed to intersheet interactions, and several neighboring β -sheets (from different molecules) can crystallize into intermolecular β -crystallites; iv) lv1-4: crystal network. It is composed of numerous β -crystallites, which are connected with each other by amorphous chains, a crystal network is indeed an individual nanofibril. During the process of crystal network formation, shear forces can help to orient the directions of the crystallites. v) lv1-5: nanofibrils network. Based on the nanofibrils network topology and internanofibril interaction strength, silk fibers and non-fiber silk materials are of different fibrils arrangements: among silk fibers, silk nanofibrils are bundled along the fibrous axis, while for non-fiber silk materials, silk nanofibrils are interconnected in a nearly random manner.

molecular vibrations and rotational information. Its principle is that when the bonds between the atoms in protein polypeptides (e.g., C=O bonds and C-N bonds) stretch and bend, they will absorb the infrared energy and consequently display a characteristic spectrum. Because the vibration frequencies for different bonds are distinct, the corresponding spectrum can therefore be regarded as the fingerprint of the molecules, to be used for identification. Peak deconvolution analysis is usually required for silk material characterization using FTIR, to quantify the content of each secondary structure. Specifically, deconvolution is carried out on the amide I vibration band, which is composed of strongly overlapping components that

correspond to various secondary structures, including the β -sheet, α -helix, β -turn, and random coil. The amide I vibration band is chosen because it is the only band among all amide vibration bands that depends on the secondary structure of the protein backbone; thus, it is minimally affected by the nature of the side-chain residues. Using peak deconvolution methods, the amide I band in FTIR spectra can be fitted with several Gaussian peaks indicative of different secondary structures. For example, the peaks of β -sheets are located at around 1620 and 1698 cm^{-1} , whereas the amorphous components are located at around 1645 cm^{-1} . The content of each secondary structural component can be determined by measuring the

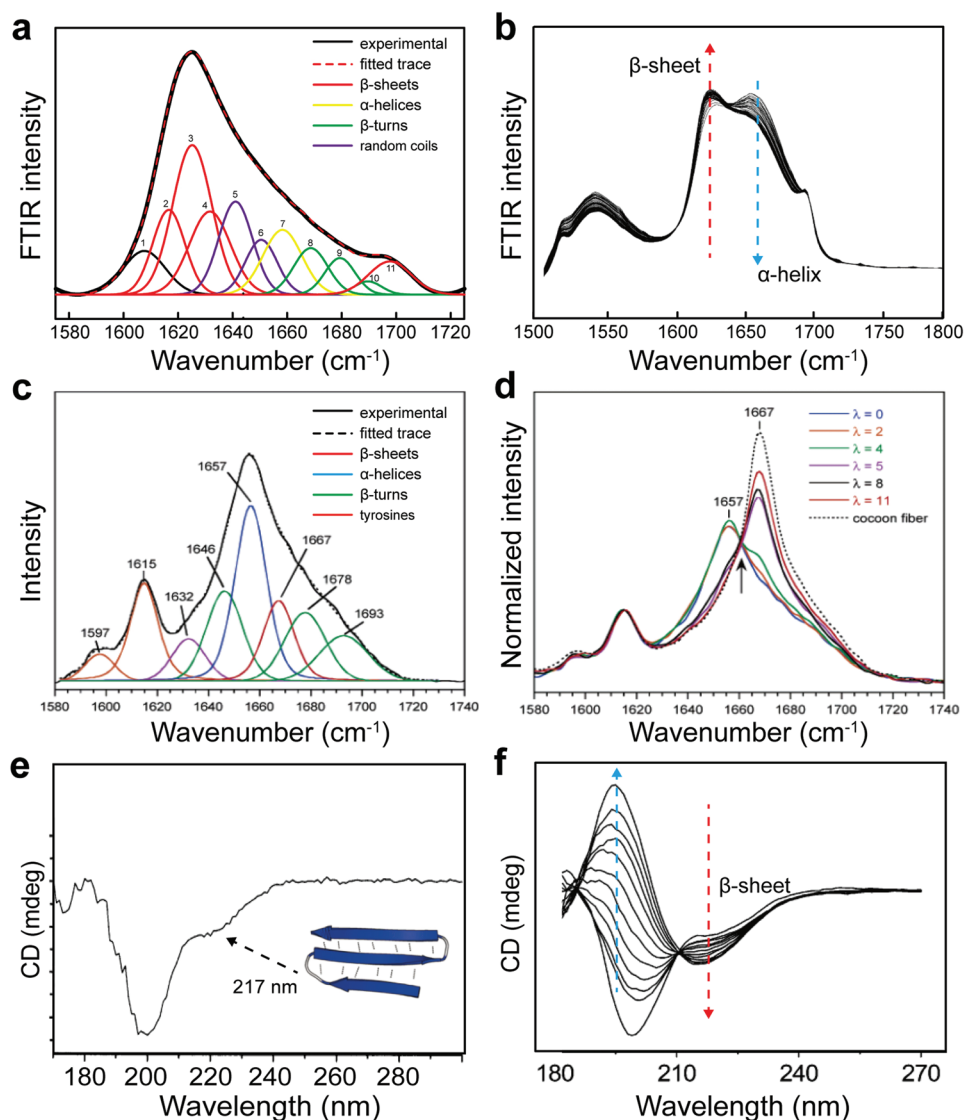


Figure 15. Techniques to characterize secondary structure in silk materials. a) deconvolution of FTIR spectra and assignment of the peaks. b) Conformation transition kinetics of regenerated *B. mori* silk fibroin membrane monitored by time-resolved FTIR spectroscopy. Reproduced with permission.^[47] Copyright 2001, Elsevier. c) Raman Band decomposition of the amide I region [1580–1740 cm^{-1}] of the isotropic spectra for *S. c. ricini* silk fibroin fibers. d) Effect of the draw ratio on the secondary structure of *S. c. ricini* fibroin fibers, revealed by Raman spectroscopy. c,d) Reproduced with permission.^[54] Copyright 2006, American Chemical Society. e) Typical far-UV spectrum for native spidroin. Two characteristic bands are presented, the plateau at 217 nm is indicative of β -sheet structures. f) Methanol induced transition of spidroin revealed by CD spectra. e,f) Reproduced with permission.^[56] Copyright 2004, American Chemical Society.

ratios of the areas under the corresponding peaks in those areas (Figure 15a).

Previously, most of the studies using FTIR for silk material structural characterization have yielded static instead of dynamic data, as they only focus on the conformations of SF molecules before and after the natural spinning/gelation process, or under other specified conditions. It is useful to monitor the conformational transition kinetics continuously in time.^[47,48] Recently, time-resolved FTIR spectroscopy has been promoted for monitoring the kinetics of conformational transition induced by various environmental factors (Figure 15b). For instance, the time-resolved FTIR process has been applied to study the influence of metallic ions on the conformational

transition process in dried spidroin/fibroin films.^[47] Similarly, the conformation transition kinetics of SF films and SF aqueous solutions induced by changes in pH and organic solvents with a low dielectric constant (e.g., methanol and ethanol) have also been studied using time-resolved FTIR.^[48]

3.1.2. Raman Spectroscopy

Apart from FTIR, Raman spectroscopy is another powerful and nondestructive technique used to investigate the secondary structures of silk materials.^[49,50] In general, Raman spectroscopy can provide information that is complementary to that

of FTIR spectroscopy. As discussed, the signals in FTIR spectrum correspond to the absorbance energy of the infrared photons released by molecules. In contrast, the Raman effect deals with the scattering process involving interactions between the incident photons and the sample molecules; in other words, the Raman spectra records the inelastically scattered energy of photons. For molecules to be infrared-active, the molecular vibrations must give rise to a change in the dipole moment of the molecules. To determine Raman activity, the molecular vibrations should induce a change in the molecular polarizability. In principle, if a molecule has a center of symmetry, then a Raman-active vibration is always infrared-inactive, and vice versa.^[53] For example, polarizable bonds, such as C–C, S–S, N=N, and O–O bonds can display intense Raman bands; however, in the infrared spectrum, these bonds show only weak or even undetectable bands. Another advantage of Raman spectroscopy for studying the protein molecular structure is that it can also provide quantitatively information about the content of secondary structures, in a similar way with the FTIR method (Figure 15c).

Recently, a so-called Raman spectromicroscopy technique has been developed by mounting a microscope onto the conventional Raman spectroscopy setup. This technique can precisely refine the size of an incident laser beam to less than 20 μm , and can thus collect scattered signals from very small samples, making it an ideal tool for recording high-quality Raman spectra of single silk filaments. Moreover, by combining Raman spectromicroscopy with an external mechanical deformation puller, the transition process of secondary structures in silk filaments when they are subjected to mechanical stretching can be detected in situ. Specifically, it is reported that both *B. mori* and spider dragline filaments have displayed well-defined Raman spectra in which the frequencies of some bands shift under the action of tensile stress or strain, suggesting the molecular conformational transition. For instance, Raman microspectroscopy has been used to quantitatively study the effect of a mechanical deformation on the secondary structure conformation and order parameters of *Samia cynthia ricini* silk fibroin fibers. According to studies of Rousseau et al.^[54] their samples were obtained from the aqueous solution stored in the silk gland and stretched at draw ratios (λ) ranging from 0 to 11. The Raman data unambiguously show that in response to mechanical deformation, SF molecules undergo a cooperative α -helix to β -sheet conformational transition (Figure 15d).

Based on the FTIR and Raman data, it is surprisingly determined that the amounts of β -sheets in silkworm silk fibers ($\approx 50\%$) almost coincide with the proportion of relevant amino acid sequences (i.e., GAGAGS amino acids that are recognized to be involved in β -sheet generation), which is 53%. In comparison, for *Nephila* dragline silk fibers, the amino acids (A)_n constitute only 18% of the total content, and this is significantly lower than the β -sheet content (36–37%) measured by Raman spectroscopy. Taking the AG and GGA motifs, which are usually located adjacent to the (A)_n blocks, into consideration, the sum value would increase to 31%. Thus, this result strongly suggests that apart from the polyaniline sequences, the AG and GGA sequence motifs might also somehow be incorporated into the β -sheets.^[55]

3.1.3. CD Spectroscopy

In comparison with FTIR and Raman spectroscopy techniques, CD spectroscopy is more suitable for quantifying the secondary structural content of proteins dissolved in solutions.^[51] CD spectroscopy is uniquely sensitive to protein chirality or overall asymmetry; it can measure the differential absorption between left-handed and right-handed circularly polarized light as a function of wavelength.^[56] As the chirality of protein molecules is determined solely by the secondary conformation, information about the secondary structure can be obtained by CD measurements accordingly (Figure 15e). Moreover, CD spectroscopy is also capable of monitoring the conformational transition kinetics in situ under different conditions. For instance, Canneti et al.^[57] have applied CD spectroscopy to investigate the conformational transition of fibroins in both aqueous solutions or in organic solvents. Dicko et al.^[56] studied the influence of storage time, storage temperature, and methanol solvents (Figure 15f) on the conformation transition kinetics of spidroin. Li et al.^[58] use CD spectroscopy to measure conformational transition kinetics and present evidence indicating that such transitions should follow a nucleation-dependent aggregation mechanism. It should be noted that although CD spectroscopy can serve as a versatile method for examining the secondary structure of SF solutions in principle, its accuracy is largely affected by the protein concentrations. In practice, only very diluted SF solutions (i.e., with concentrations ranging from 0.01 to 0.2 g L⁻¹) are appropriate for CD experiments.

3.1.4. Wide Angle X-ray Diffraction and Small Angle X-Ray Scattering

FTIR, Raman, and CD spectroscopy are generally used to quantify the secondary structure content, while the X-ray diffraction (XRD) technique is the most commonly applied technique for analyzing the level 3 structure of silk materials.^[46,59,60] The principle of XRD is that the crystalline structure within silk materials can cause incident X-ray beams to diffract into many specific directions; by measuring the angles and intensities of such diffracted beams, a 2D profile reflecting the crystalline structures can be produced and gathered for quantitative analysis. In particular, according to the Bragg's law, in case of subnanometer-sized crystalline structures (e.g., 0.1–10 nm), wide angle X-ray diffraction (WAXD) or wide angle X-ray scattering (WAXS) can be applied. Small angle X-ray scattering (SAXS) is ideal for obtaining structural information of larger crystalline molecules with dimensions between 1 and 100 nm, and of repeat distances in partially ordered systems with a length of up to 150 nm. On condition that silk materials belong to semicrystalline macromolecular materials; WAXS has been developed as a powerful method for studying the size and orientation of crystallites as well as the crystalline content (crystallinity) within the crystal network of silk materials. On the other hand, the SAXS technique is applied to measure the intercrystallite distances within crystal network inside silkworm silk and spider dragline silk fibers.^[46] The detailed analysis methods will be described below.

Crystallite Content (Crystallinity) and Crystallite Size: Radial integration along the equatorial and meridian directions of the WAXS pattern (Figure 16a) can give rise to a 1D profile of the

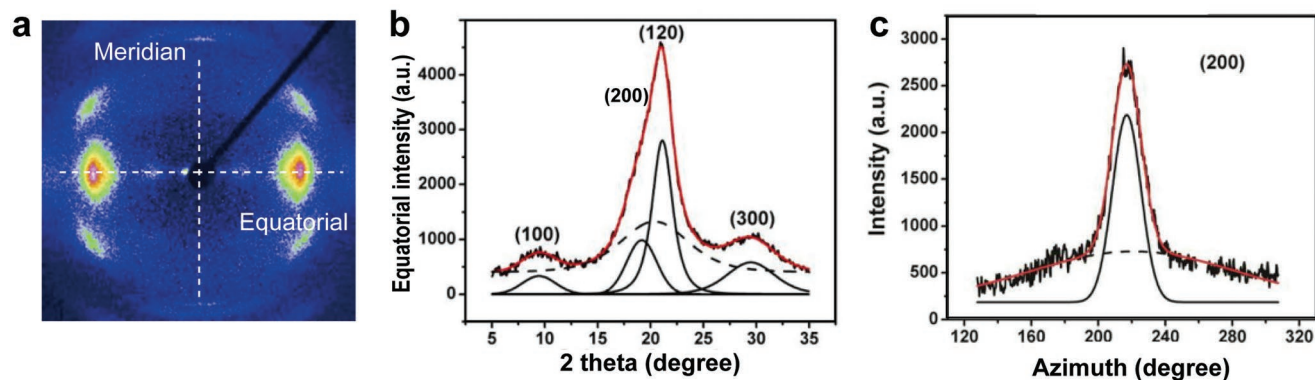


Figure 16. XRD analysis of the structural information of silk materials. a) Typical scattering pattern of silkworm silk fiber. b) The radial integration of intensity as a function of diffraction angle (2θ) along the equatorial direction of the WAXS pattern. c) Intensity as a function of azimuth angle at the radial position of the equatorial (200) peak of silkworm silk. The peak is fitted as sums of two Gaussians, corresponding to crystalline (black, solid line) and amorphous (black, dashed line) distributions. The orientation function f is calculated by FWHM of the crystalline Gaussians peak.

scattering intensity as a function of the 2θ angle (Figure 16b). Afterward, this profile is deconvoluted into several peaks (corresponding to crystalline domains) and a halo (corresponding to amorphous regions). For silkworm silk fibers, the equatorial data is deconvoluted into four crystalline peaks corresponding to the (100), (200), (120), and (300) Bragg reflections and an amorphous halo. The meridian data, on the other hand, is deconvoluted into two more crystalline peaks corresponding to (002) and (102), and an amorphous halo. The crystallinity is determined by the ratio of the area under the crystalline peaks in the equatorial data (i.e., the (100), (200), (120), and (300) peaks) to that of the total reflection patterns. According to Scherrer's formula, the crystalline size in 1D is equal to $\frac{0.9\lambda}{FWHMCOS\theta}$, where FWHM is the full width at half-maximum of the peak, at the diffraction angle θ , and the wavelength of incident ray λ is 0.15418 nm. The crystallite size along the a -, b -, and c -directions is determined by the position and FWHM of the (200), (120), and (002) peaks, respectively.^[46] For spider dragline silk fibers, the crystallite size is measured to be $a = 2.1$ nm, $b = 2.7$ nm, and $c = 6.5$ nm. The dimensions of silkworm silk fibers are relatively larger, that is, $a = 2.3$ nm, $b = 4.1$ nm, and $c = 10.3$ nm.

Orientation Function f : Experimentally, the information about the orientation of crystallites can be measured via the WAXS intensity integration, as a function of the azimuth angle at the radial position of equatorial (120) and (200) peaks (Figure 16c). Here, the orientation function f is defined by the Hermans orientation function.

$$f = (3\langle \cos^2\phi \rangle - 1)/2 \quad (1)$$

where Φ is the angle between the c -axis of the crystallites and the fiber axis. For the two reflections, (200) and (120), which are not orthogonal, but have a known geometry in the equatorial plane, the expression of $\langle \cos^2\phi \rangle$ is determined using the equation:

$$\langle \cos^2\phi \rangle = 1 - 0.8\langle \cos^2\phi_{200} \rangle - 1.2\langle \cos^2\phi_{120} \rangle \quad (2)$$

The FWHM values of the (200) and (120) peaks were measured in a direction perpendicular to that of the fiber axis, using the following equation:

$$\langle \cos^2\phi_{200} \rangle = 1 - [\cos(0.4FWHM_{200})]^2 \quad (3)$$

Thus, the FWHM data can be applied to calculate the orientation function. If $f = 1$, β -crystallites are oriented in a direction that is completely parallel to the fiber axis. However, if $f = 0$, β -crystallites are oriented randomly.^[46]

Intercrystalline Distance: As described by the molecular crystal network structure, crystallites, which serve to scatter the incident X-rays, are embedded randomly into amorphous regions and have a cylindrical symmetry along the fiber axis. In this regard, the SAXS intensity in the equatorial direction can be determined using the formula:

$$I = \frac{Kl_c^2}{(1 + l_c^2q^2)^{3/2}} \quad (4)$$

Here, $q = 4\pi\sin\theta/\lambda$ is the scattering wave vector, θ is the scattering angle, and λ is the X-ray wavelength; l_c is the correlation length and can be determined from the intercept and slope of a plot of $I^{-2/3}$ versus q^2 . To determine the level of scattering along the meridional direction, the SAXS intensity is expressed as

$$I = \frac{Kl_c^2}{1 + l_c^2q^2} \quad (5)$$

Here, the correlation length l_c along the meridian is determined from the intercept and slope of the plot of I^{-1} versus q^2 . These two correlation lengths can be related to the intercrystalline distance. Notably, the silk fiber has a fibrous axis with and its properties are different along the equatorial and meridional directions. Hence, the correlation lengths should be considered separately along two directions. Recently, Du et al.^[46] have applied this SAXS technique to study the influence of different reeling speed on the intercrystallite distances within spider dragline silk fibers. According to their results, there exists a deflection point in the correlation between intercrystallite distance and the reeling speed. Specifically, when the reeling speed is below 10 mm s^{-1} , the distance between the crystallites (correlation length) becomes larger with the reeling speed, along both the meridional and equatorial directions. This is consistent with the fact that fast reeling speed easily extends the relatively

loosely packed amorphous chains between crystallites, which consequently gives rise to larger intercrystallite distance. Nevertheless, upon further larger reeling speed (that is, $>10 \text{ mm s}^{-1}$), the nanofibril segments start to merge together so that the distance between the crystallites becomes smaller. This merging phenomena of nanofibril segments has been observed with AFM, where the observed “particle size” becomes larger meanwhile several hollow regions begin to appear.

3.1.5. AFM Force Spectroscopy

Conventionally, AFM force spectroscopy is a technique that endows probing mechanical unfolding and refolding processes of proteins and DNA at a single molecule level. During the measurements, the AFM cantilever approaches and snaps into the sample, and then retracts from the surface. At the same time, the cantilever deflection (correlated to the force applied onto the sample) versus piezo movement (correlated to the separation between AFM tip and protein sample) is recorded, which is ultimately converted to *force versus extension* curves of protein in response of mechanical pulling and can provide detailed mechanical information as well as nanostructures about samples. For instance, AFM force curves can reveal various mechanical properties of the sample including adhesion, stiffness (modulus), rupture force and indentation depth (how much the AFM tip penetrates in the sample at a given load, which reflects the hardness of the sample). Recently, AFM force spectroscopy has also been applied to study the sequential unfolding of nano- β -crystallites within SF materials (Figure 17).^[11] The analysis focused on how these crystallites breaks (i.e., β -sheets been pull off or β -strands been unzipped) can provide insight into how such crystallites are associated with each other and form into crystal networks.

3.2. Imaging Techniques

3.2.1. Scanning Electron Microscopy

SEM is capable of scanning silk material samples with a focused electron beam instead of light and delivering largely magnified images with information about the samples' topology as well as composition. The principle of SEM is that the incident electrons can have interactions with the atoms within silk samples so that different parts of samples produce various signals, that is, secondary electrons, backscattered electrons and characteristic X-rays. These signals can reveal hidden information of the silk materials samples: specifically, the secondary electrons signals are associated to the topography of the samples; the backscattered electrons can provide the information of phase contrast in the samples while the characteristic X-rays can be applied for element identification (so-called energy dispersive x-ray spectroscopy, EDX technique).

So far, SEM has been widely applied to examine the micro/nanostructures within different forms of silk fibroin materials. For instance, Nguyen et al.^[25] imaged the freeze-dried regenerated silk fibroin hydrogels and found that they are composed of numerous nanofibrils with random distribution. The

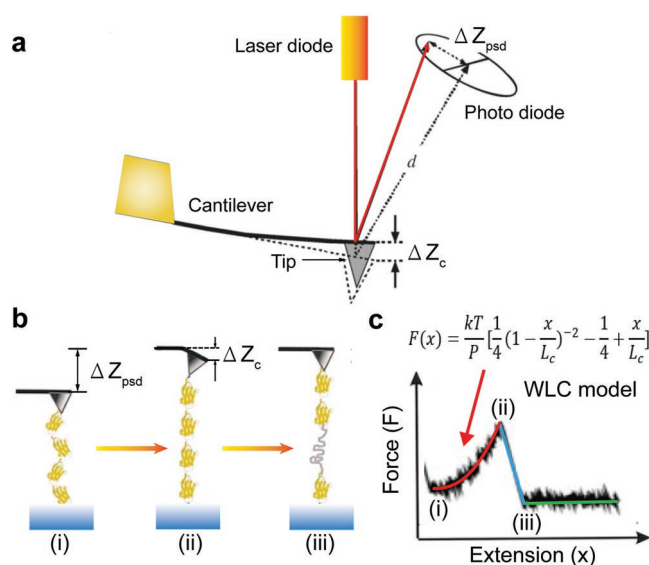


Figure 17. a) Schematic illustration of the AFM setup. The force is measured by the deflection of the cantilever and the extension can be calculated from the position of the cantilever. b) The unfolding of a protein domain (or crystallite in case of SF materials) by an external force. When stress is applied onto samples, the protein domains will begin to unravel. As the distance between substrate and cantilever increases (from states (i)–(ii)), the protein elongates and the reduction of its entropy generates a restoring force that bends the cantilever. When a domain unfolds (state (iii)), the contour length of the protein increases, returning the force on the cantilever to near zero. Further extension again results in force on the cantilever (state (i) again). c) The entropic elasticity of proteins can be described by the worm-like chain (WLC) model of polymer elasticity (inset). This equation predicts the entropic restoring force (F) generated upon extension (x) of a protein in terms of its persistence length (p) and its contour length (L_c). The saw-tooth pattern of peaks on the force–extension relationship corresponds to sequential unraveling of individual domains of a modular protein like the one shown here. The number of peaks correspond to the number of domains.

corresponding SEM image clearly shows that the average diameter of nanofibril is ranging from 20 to 50 nm.^[25] For natural silk fibers, SEM has successfully distinguished the sericin coating from the core fibroin filaments (Figure 18a).^[1] However, given the fact that silk fibers belong to nonconductive materials so that they require a gold spraying process in prior of SEM imaging. Besides, the nanofibrils within silk fibers are bundled very close to each other. In this regard, it is much more difficult to obtain satisfying images of the nanofibrils network on silk fiber surface. Nevertheless, upon proper sample preparation (e.g., applying freeze-drying and controlling spraying time), the morphology of nanofibrils within silk fibers can still be observed (Figure 18b, to be published).

3.2.2. Transmission Electron Microscopy

Similar as SEM, TEM is a microscopy technique which also applied a beam of electrons but it is capable of imaging at even higher resolutions. Nevertheless, such electrons are transmitted through the samples to form an image. In principle, the samples for TEM measurements are most often ultrathin sections less than 100 nm thick or a suspension on a grid, which

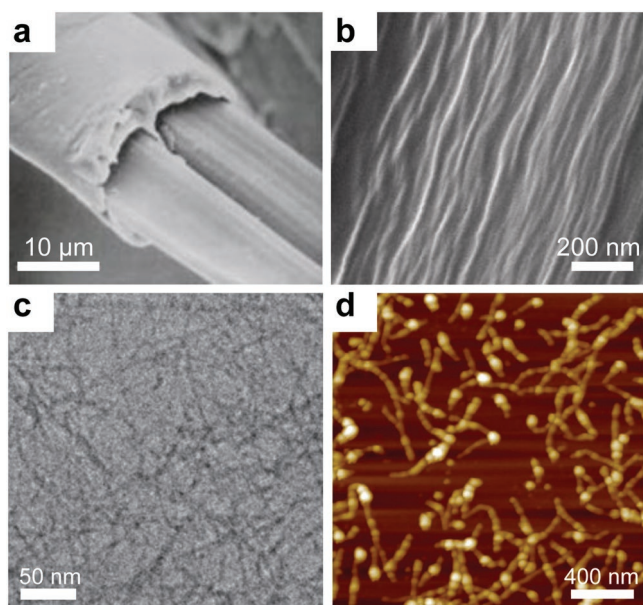


Figure 18. Morphology of SF materials characterized by imaging techniques. a) Typical SEM image of natural silkworm silk fiber. Reproduced with permission.^[1] Copyright 2002, Springer Nature. b) SEM image of natural silkworm silk fibers after proper freeze-drying treatment, fibrous morphology was revealed. c) Cryo-TEM image of RSF gel (incubated 50 min), nanofibrils can be easily observed. Reproduced with permission.^[45] Copyright 2009, Royal Society of Chemistry. d) AFM height image of 0.01 mg mL⁻¹ SF aqueous solution; nanofibrils have spontaneously formed and deposited on the substrate.

gives difficulty in preparing ideal silk materials samples. For instance, in case of measurement on cross sections of natural silk fibers, given the fact that β -crystallites within crystal networks are patterned parallel with each other and along with the fibrous axis, the silk fiber display a strong tenacity. In other words, when perpendicularly sliced the silk fibers, the crystallites are more likely to be bent or deformed rather than to be tore apart. On the contrary, when applying TEM technique to study the morphology of nanofibrils within SF gels, Gong et al.^[45] have observed that the spontaneously formed translucent gel is composed of entangled proto-fibrils with length of hundreds of nanometers and width of about 5 nm (Figure 18c). In addition, they have also mimicked the “flow-effect” by applying circular agitation to the RSF solution and found that several white fibrous flocs are generated after shearing the RSF solution for a period of time, suggesting shear flow has impact on the formation of SF nanofibrils.^[45]

3.2.3. AFM Imaging

AFM can provide a nanoscale 3D profile of a sample surface by measuring forces between a sharp probe (with radius less than 10 nm) and the sample surface. Different surface topography and property of samples can lead to different values of interactions, which can be reflected and detected by the AFM instruments. So far, AFM height imaging technique has been widely applied to study morphology of silk materials (Figure 18d). An advantage of AFM is that it can provide height information

of the samples with very high resolutions. It is determined that the thickness of nanofibrils are much smaller compared with the diameters, suggesting that the SF nanofibril are flat ribbon-like rather than symmetric cylinder-like aggregates.

Recently, AFM has also been applied to distinguish the locations of different constituents within composite RSF films. For instance, Xing et al.^[61] have incorporated wool keratin molecules @ gold nanoclusters (WK@AuNCs) into the mesoscopic network structures of SF films and synthesized a novel biodegradable WK@AuNCs-SF memristors and then successfully identified the location of such clusters via AFM. As the WK@AuNCs accumulate electrons at their surface, the interactions with the conductive AFM tip can significantly differ with those SF molecules. In this regard, the Kelvin probe force microscopy (KPFM) is capable of potential imaging by measuring the surface charge distribution.^[61]

4. Self-Assembly Pathways of Silk Materials and Controlling Mechanisms

4.1. Different Self-Assembly Pathways: Liquid Crystal and Micelles Models

The formation of a solid fiber from soluble spidroin or fibroin proteins is a result of a complex biochemical and physical process that occurs within specialized spinning organs. To describe how the spidroin proteins self-assemble into fibers, there are different models that have been put forward. Two of them are namely the “liquid crystal” and “micelle” models (Figure 19).^[62]

The “liquid crystal” model is proposed by Vollrath and Knight.^[2] After using polarizing microscopy to study the spinning ducts and MA gland of spiders, they propose the presence of liquid crystalline structures. In examining the roles and structures of the spinning ducts, they claim that the adoption of such liquid crystalline phases for proteins is necessary. Specifically, the MA gland consists of a long tail and wider sac. The tail can secrete spidroin molecules, while the sac constitutes the main storage area and is linked to a tapering duct (spinning duct). The spinning duct has three loops inside a sheath and terminates in the valve. The newly formed silk thread in the valve is inserted into a narrow tubular region, which has a specialized design for rapid water recovery. Within the MA gland, the first and second loops of the spinning duct, the spider’s dope can spontaneously form a nematic liquid-crystalline phase, that is, the molecules form a “substance” that flows as a liquid but maintains some of the orientational order that is characteristic of a crystal. This phase endows viscous protein solutions with the ability to flow slowly through the duct, even at high concentrations, while the molecules can still form complex alignment patterns. Particularly, in the first two loops, the long axes of the rod-shaped silk protein molecules or molecular aggregates are oriented parallel to each other, but in a direction perpendicular to the secretory epithelial walls. The protein molecules gradually bend over eventually, with an increase in the distance, until they are exposed to the third loop of the spinning duct; then, they lie in a direction parallel to that of the long axis of the silk gland and spinning duct. It is likely that the initial perpendicular arrangement and subsequent

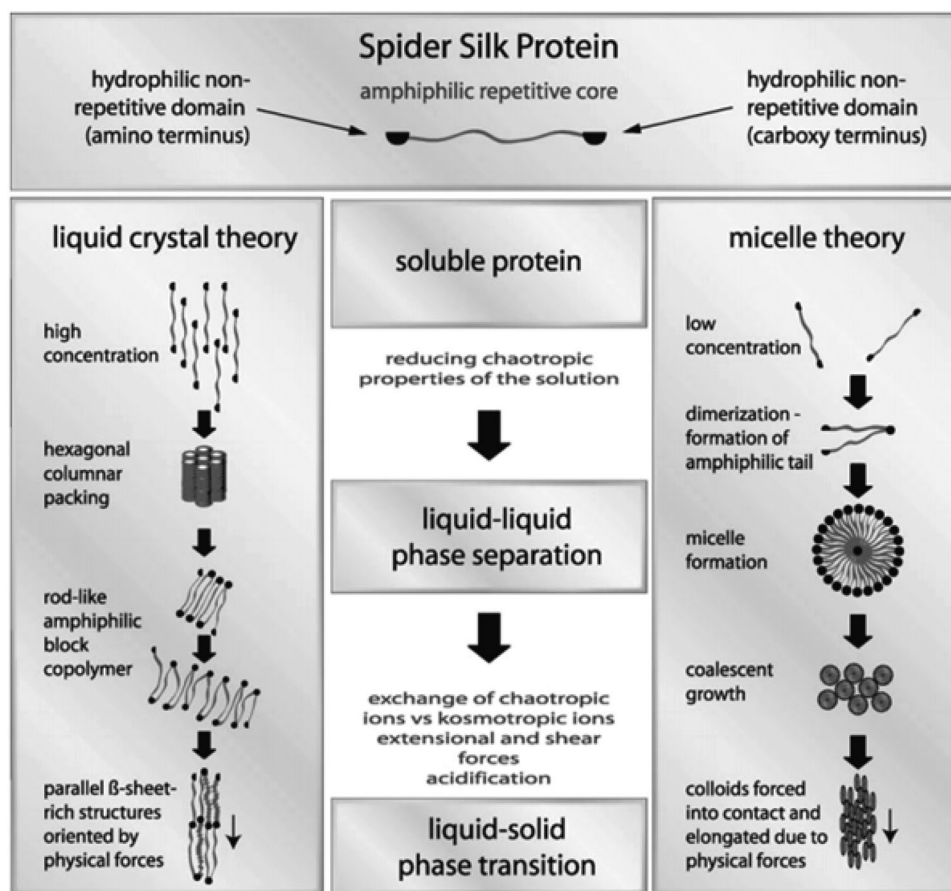


Figure 19. Two established models that describe spider silk thread formation. Reproduced with permission.^[62] Copyright 2009, Wiley-VCH.

parallel arrangement can prevent the liquid crystalline dope from breaking up into numerous small domains, which in turn suppress the formation of disclinations (this is a type of defect somewhat analogous to dislocations in solid crystals, and its presence can diminish the tensile strength of the spun thread). Within the framework of the “liquid crystal” model, the shear force created during the rapid thread extension process plays an important role in determining the conformational transition of SF molecules inside silk dope and the formation of silk threads.

Jin and Kaplan,^[14] who proposed the “micellar model,” claim that the self-assembly of dope proteins into silk fibers should be accomplished in a different way: As both hydrophobic and hydrophilic blocks are identified within the individual SF polypeptides, SF polypeptides might form micelle-like structures, that is, the hydrophobic blocks of protein molecules might self-assemble into micelles due to hydrophobic interactions, while the larger hydrophilic blocks at both the N and C terminals define the outer edges of the formed micelles (Figure 19). During this initial step of micelle formation, the subtly intervening smaller hydrophilic regions of protein molecules are still hydrated to ensure that they can maintain the solubility. Thus, the crystallization of proteins was avoided. By increasing the dope concentration (by secretion), interactions between nearby micelles are promoted, which leads to coalescence, and consequently the formation of larger globular structures. Finally,

during the last stage, the shear force and ductal wall boundaries exert great impact on the formation of solid-state silk thread. For instance, the shear force can initially elongate and align micelle-containing globules and trigger a structural transition from the predominant soluble silk I structure to the insoluble crystalline silk II structure, which establishes the basis for high-strength and toughness silk fibers. This shear force also simultaneously shape and determine the fibrillar morphology.

In interpreting some experimental observations, these two models are not mutually exclusive. In particular, the idea of lyotropic liquid crystals can be applied to explain the amphiphilic characteristics, leading to the self-assembly into different morphologies. At low concentrations, lyotropic liquid crystals spontaneously assemble into micelles (i.e., the micellar model), while at higher concentrations, they are packed into hexagonal columns (as described by the liquid crystal model). Such concentration-dependent characteristics of the lyotropic liquid crystals can somewhat explain the significant variance between *in vivo* and *in vitro* fibroin self-assembly experiments. For instance, during the *in vivo* investigations into silk glands (with a dope concentration of 30 wt%), liquid-crystalline behaviors are commonly seen; however, during the *in vitro* study of the regenerated silk fibroin (RSF) aqueous solution (that are much more diluted than the dope solution), only micellar-like aggregations can be produced.

4.2. Formation Mechanism of Multilevels of Crystal Networks within Framework of Nucleation Model

Although the two theories in Section 4.1 illustrate the SF self-assembly mechanism during the fiber spinning process in silk glands, they still cannot thoroughly explain why nanofibrils can still be spontaneously formed even in the absence of elongation flow/shear force (e.g., in stilled diluted SF solutions). By studying the hierarchical network structures of silk materials and the corresponding formation kinetics, we have proposed another refined self-assembly pathway for SF molecules, that is, a nucleation and growth model (also known as the crystal network model). In this model, SF molecules self-assemble into hierarchical network structures via several nucleation-controlled steps. Specifically, these require 1) SF molecules to assemble and nucleate into β -sheets; 2) the β -sheets to grow into β -crystallites through stacking; 3) many β -crystallites to be linked via amorphous chains and altogether form the crystal network; and 4) nanofibrils to further grow and interact with each other, and consequently lead to the formation of nanofibrils networks. In detail, during stage 1, most SF molecules are in the random coil or α -helix conformations and are therefore soluble. Gradually, because of thermal fluctuations, such molecules begin to move forward toward each other. Along with the breakage of initial intramolecular H-bonds and formation of intermolecular H-bonds, the transition to β -sheets is triggered. The total free energy of the entire system is lowered because of the formation of β -sheets, and the β -sheets have a more compact structure than their precursors. In this regard, such a conformation transitional process can be identified to be a crystallization process. During stage 2, because more β -sheets are present in the solution, intersheet interactions (such as hydrophobic interactions, van der Waals interactions) further give rise to the stacking of nearby β -sheets and result in the crystallization of β -crystallites. β -crystallites are attributable for the closed package and well-defined patterns of β -sheets, and should be regarded as more stable “polymorphs” of β -sheets. During stage 3, the shear force (such as the force in the silk spinneret) orient the β -crystallites into a parallel direction. However, in the absence of such shear forces (e.g., during the SF hydrogelation process), the orientation of crystallites is less orderly. In stage 4, the differences in nanofibril interaction strength and the nanofibrils network architecture give rise to different mechanical performance of silk materials accordingly.

The formation of mesoscopic hierarchical meso crystalline network structure of silk materials has been found to follow the nucleation mechanism.^[12] The nucleation kinetics of both the homogeneous nucleation and heterogeneous nucleation processes can be thoroughly quantified by determining the nucleation rate, which is defined as the number of mature nuclei created per unit volume-time in the system. The nucleation rate is usually highly correlated to many factors, especially the concentration of the nucleating phase and the surrounding chemical environments. We have described several key environmental factors in terms of crystallization mechanism that affect the crystallization kinetics, crystallinity, and structure of silk fibers during the natural spinning process (Note S4, Supporting Information).

According to classical nucleation theory (CNT), nucleation occurs only if the so-called nucleation barriers can be overcome.^[63] Besides, the newly formed crystalline phases are not thermodynamically stable until the dimensions are beyond the critical size. Mathematically, the nucleation barrier ΔG^* and the critical size R_c are represented by Equation (6):

$$\Delta G^* = \frac{16\pi\gamma^3}{3(\rho_c\Delta\mu)^2} \text{ and } R_c = \frac{2\gamma}{\rho_c\Delta\mu} \quad (6)$$

Here, ρ_c is the particle density in nuclei, γ is the surface free energy area density and $\Delta\mu$ is the chemical potential differences between the mother phase and crystalline phase.^[63] As observed in Equation (6), it is evident that $\Delta\mu$ is the prime factor; hence, we need to highlight and comprehensively discuss it. The following equation can be obtained from the definition of $\Delta\mu$:

$$\frac{\Delta\mu}{k_B T} = \ln \frac{a}{a^{eq}} \approx \ln \frac{C}{C^{eq}} \quad (7)$$

Here, a^{eq} and C^{eq} represent the equilibrium activity and concentration, respectively. By altering either the concentration of SF solutions or the equilibrium concentration for SF molecules (can be achieved by changing the pH, ionic strength, temperature, etc.), the crystallization kinetics can be effectively controlled accordingly.

As the probability of nucleation is uniform throughout the entire system, the above process is therefore known as homogeneous nucleation. However, in reality, it is difficult for homogeneous nucleation to occur due to its extremely high nucleation barrier. Nevertheless, foreign bodies/substrates are always present in the system (e.g., the wall of solution containers, foreign particles, or substrates). In principle, if strong interactions can occur between the crystalline phase and foreign substrates, the occurrence of such foreign bodies will significantly lower the nucleation barrier; hence, the probability of occurrence of nucleation adjacent to the foreign bodies is higher than elsewhere in the system (**Figure 20A**). This is referred to as heterogeneous nucleation.^[10,63] To quantify the ability of foreign bodies to lower the nucleation barrier with regard to the homogeneous nucleation barrier, the interfacial correlation factor $f(m)$ has been proposed; the parameter m describes the structural match between the crystalline phase and the substrate. Specifically, in the case of a perfect match, $f(m) \approx 0$. This implies that the heterogeneous nucleation barrier vanishes completely when the nucleating phase is well ordered and oriented along the structure of the foreign body substrates. However, when the structural match is poor (i.e., $f(m) \rightarrow 1$), there is almost no correlation between the foreign body substrates and nucleating phase. In this extreme case, the substrate has almost no influence on the nucleation process, which is equivalent to homogeneous nucleation.^[10,63] In nucleation cases, f usually ranges from 0 to 1, which suggests that primary nucleation is somehow governed by heterogeneous nucleation.

Specifically, in case of heterogeneous nucleation in SF molecules, the role of foreign substrates/surfaces/nanoparticles in directing the self-assembly of SF proteins and polypeptides has been reported recently. By carefully selecting functional nanomaterials and controlling the SF solution conditions, the

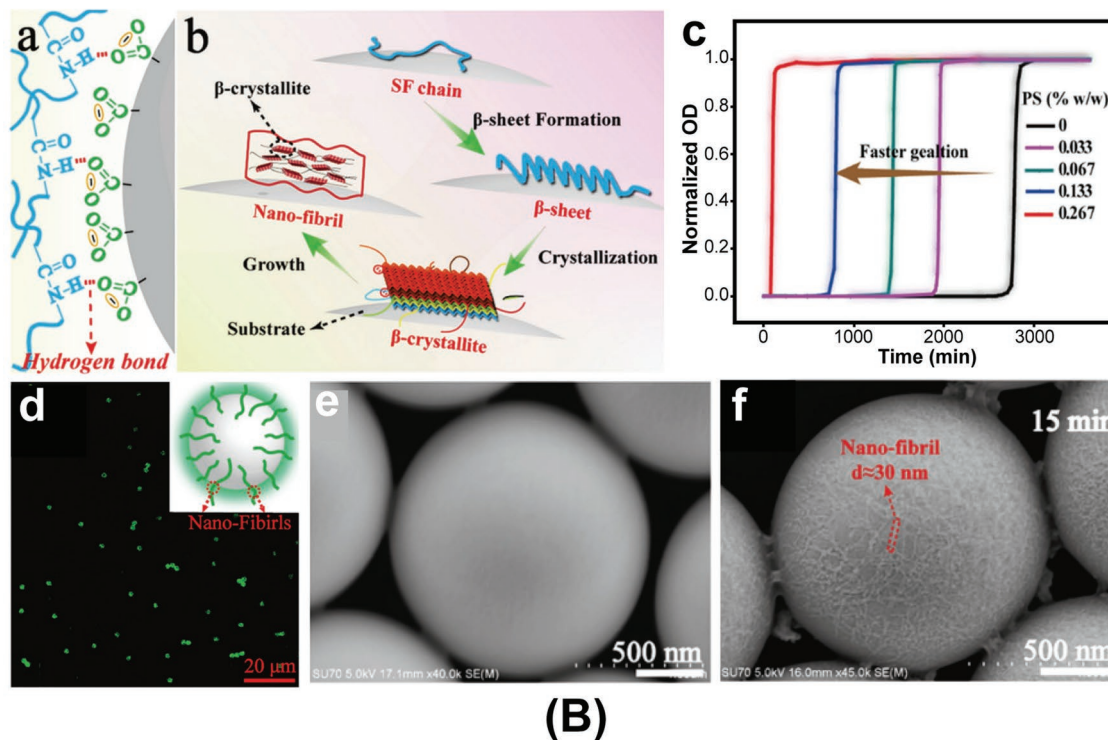
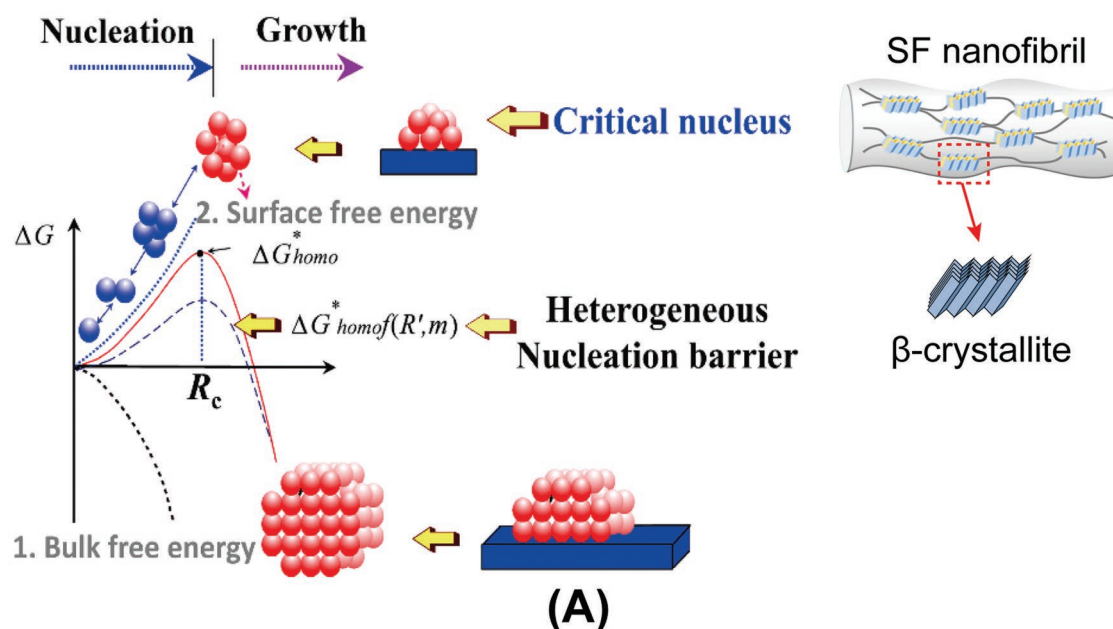


Figure 20. Schematic showing heterogeneous nucleation and the effect of foreign substrates. A) Heterogeneous nucleation can decrease the nucleation barrier so that crystallization of SF molecules are promoted. Reproduced with permission.^[10] Copyright 2015, Royal Society of Chemistry. B) a) Illustration of H-bonds between the amino groups of SF peptide chains and carboxyl groups on the surface of foreign nanoparticles. b) Schematic of foreign nanoparticle-induced heterogeneous nucleation of SF. c) Normalized OD changes of neat SF solution and SF-PS mixtures with various PS concentrations. The PS templates can greatly accelerate the nucleation rate of SF molecules. d) Confocal laser scanning microscopy image of PS particles (2 μm) incubated in a FITC-labeled SF solution for 30 min. SEM images of PS particles incubated in SF solutions for e) 0 min and f) 15 min, respectively. SF nanofibrils with a diameter of around 30 nm can be seen on the surface of PS particles after 15 min. Reproduced with permission.^[11] Copyright 2016, Wiley-VCH.

foreign substrates can show a strong templating effect during SF protein heterogeneous nucleation. For instance, some monodispersed nanoparticles (coated with numerous functional

carboxyl groups on the surface) can serve as an ideal foreign body that provide nucleation sites, at which the interactions between such nanoparticles and SF molecules mainly include

the formation of H-bonds between the amino groups of SF peptide chains and carboxyl groups on nanoparticle surfaces.^[12] This strong interaction can reduce the nucleation barrier and speed up the nucleation of β -sheets as well as β -crystallites. SF molecules should be more likely to crystallize on the surface of such nanoparticles; this phenomenon has already been confirmed by confocal laser scanning microscopy and SEM,^[12] as shown in Figure 20B-d and Figure 20B-f, respectively. It is clearly observed that green fluorescence-labeled SF molecules accumulated around the nanoparticles. On the other hand, SEM images of nanoparticles incubated in SF solutions also clearly displayed the accumulation of SF nanofibrils on the surface of these nanoparticles; with longer induction time, the number of SF nanofibrils increased.

Apart from H-bonding, it has recently been reported that hydrophobic interactions between foreign substrates (e.g., graphene) and SF molecules are also effective in templating SF heterogeneous crystallization.^[64] For instance, by controlling the experimental conditions precisely, an almost complete coverage of graphene nanosheets by layers of densely packed SF nanofibrils can be achieved.^[64] On the contrary, very few ($\approx 1\%$) SF nanofibrils are observed outside of graphene nanosheets, suggesting that nanofibril formation (heterogeneous nucleation) occurs in a highly selective manner, only on graphene nanosheets.^[64] This heterogeneous nucleation of SF molecules on foreign bodies might shed new light into the synthesis of composite silk materials.

We notice that this nucleation-controlled SF network formation model allows the interpretation of many novel effects observed in silk materials. Subject to the nature of nanocrystallites, the formation of nanofibrils (crystals networks) is controlled by intermolecular nucleation, which allows the reconstruction and mesofunctionalization of silk materials. More details will be given by the following sections.

5. Mesoscopic Reconstruction and Mesoscopic Engineering

In 12, we characterized the multilevel structures in silk materials and studied the corresponding structural factors associated with the macroscopic performance. In Section 2, we introduced several advanced characterization techniques that revealed the hierarchical structure factors, especially those of the second and third level. In Section 3, we investigated different models, described how dope proteins are self-assembled and proposed a refined “crystallization” model that was based on the crystallization mechanism. Besides, we also comprehensively discussed several factors influencing nucleation kinetics and pathways. Altogether, the comprehensive knowledge of the hierarchical network structures of silk materials and the formation mechanism has enabled the identification of effective strategies for designing and programming silk materials exhibiting an enhanced level of performance. In this section, we will highlight how these strategies can be implemented in detail. Noticing that structure and mechanical property of silk materials are highly process-dependent in which the hierarchical structures are constructed by a totally spontaneous process of self-assembly, it is suggested that the concept of “nanoarchitectonics” fits well

with SF materials. Nanoarchitectonics is a unified concept combining nanotechnology and methodologies and it concerns the harmonized assembly of nanoscale objects into higher order functional materials.^[65–67] Within the framework of nanoarchitectonics, several techniques for constructing mesoscopic structures within silk materials will be discussed. For instance, the regulated molecular manipulation (e.g., gene modification), the chemistry-based molecular modification (e.g., tethering functional groups/substrates to polypeptide chains), the controlled physicochemical interactions (e.g., manipulating hydrogen bonding, hydrophobic interactions), the self-assembly and self-organization, and the structural regulation of physical stimuli (ultrasonication, electric field, vortex-induced shearing force, etc.).^[67] In addition, given the significant difference between the silk fibers and non-fiber silk materials (because of the differences in strength in the internanofibril interactions), we shall discuss mesoreconstruction methods for fabricating silk fibers and non-fibrous materials separately.

5.1. Silk Fibers

5.1.1. Natural Silk Fibers

Genetic Modification to Produce Functionalized Silk Fibers: As discussed, the primary structure of silk fibers refers to the amino acid sequences. If the amino acid sequences are changed, the corresponding structure and mechanical performance are also altered. It is reported that genetic modification techniques have been successfully applied for producing fluorescent colored silks.^[68] According to previous studies, the gene for the fluorescent colored protein (e.g., green fluorescent protein [GFP]) can be inserted into the silkworm genome and then the SF proteins and fluorescent proteins are co-expressed simultaneously. Consequently, transgenic, fluorescent colored silk fibers are obtained. As the primary structure of silk fibers is incorporated within the sequence of fluorescent proteins, the mechanical strength of the hybrid silk fibers is slightly improved (or decreased).^[68]

Although fluorescent protein sequences can be incorporated into the primary structure of silk fibers and consequently change the mechanical properties, the modulation ability is not satisfying. Because the mechanical properties of spider silks (especially the dragline silk fiber) are superior to those of silkworm silk, numerous efforts have recently been devoted to the use of genetically modified silkworms as the host for the production of transgenic spider silk fibers.^[69–71] Previously, most relevant attempts focus on transposon-mediated transgenic silkworms. These silkworms can successfully produce reinforced silk fibers. However, the amount of spider silk proteins in these transgenic silkworms is very low ($<5\%$); this may be attributable to the variable promoter activities and endogenous SF protein expression.^[70,71] Recently, Xu et al.^[69] put forward a system for the production of massive amounts of spider silk in silkworms using a transcription activator-like effector nuclease (TALENs)-mediated technique, to replace the fibroin H-chain gene of silkworms with the MA spideroin-1 gene (Figure 21). According to their experimental results, the achieved yield of chimeric spider protein within the obtained hybrid silk fibers is

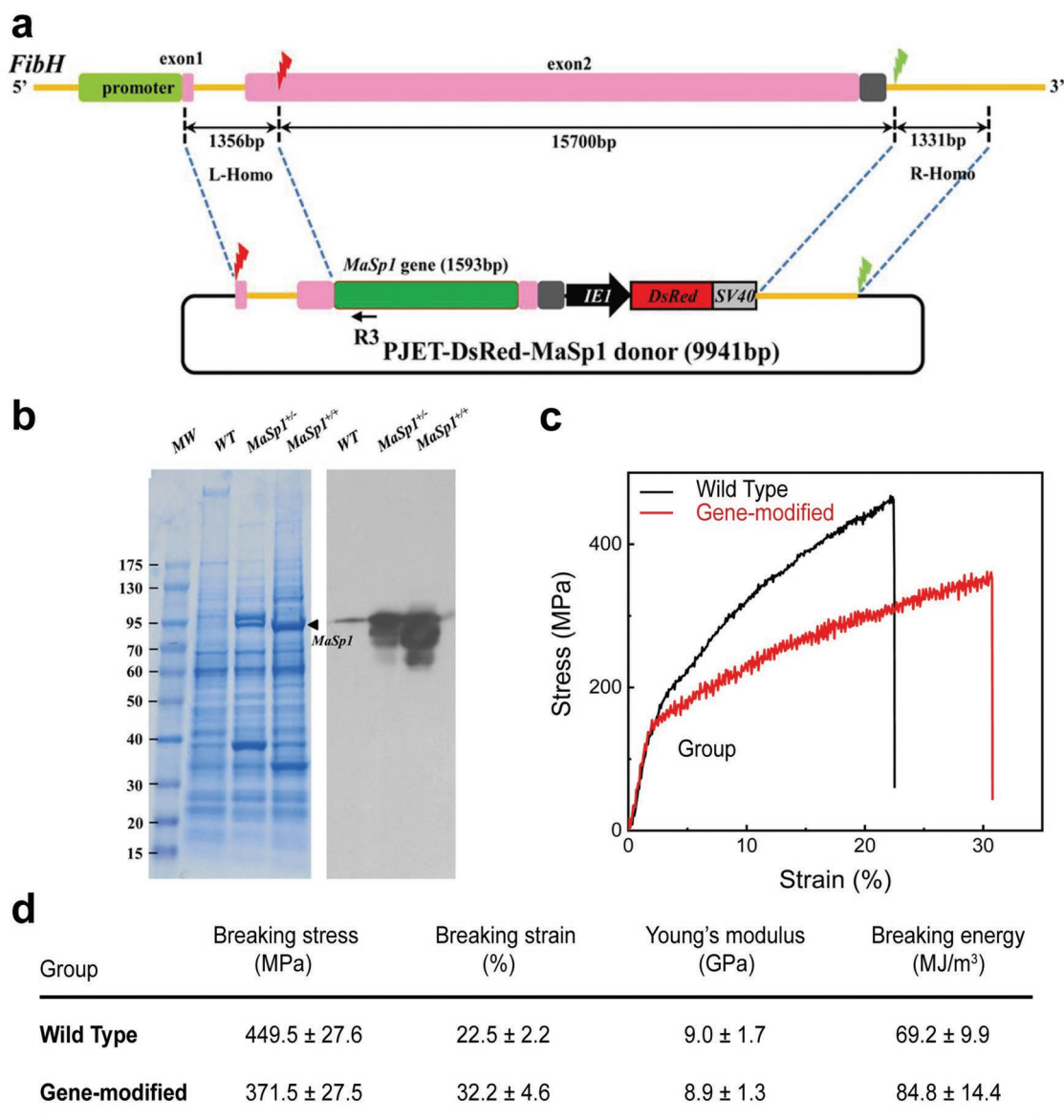


Figure 21. Genetic modification technique can be applied to produce functionalized silkworm silk fibers. a) Schematic representation of the TALEN-mediated gene replacement system. The partial sequence of the spider MA fiber protein is shown using the green box. It is inserted into the protein sequence of silkworm fibers. b) Spider MA proteins were successfully expressed in the silk glands of gene-modified silkworms. The black arrows indicate the MaSp1 protein. c) Typical stress–strain curves of the wild-type and gene-modified silk fibers. d) Mechanical properties of wild-type and gene-modified silk fibers. The breaking strain as well breaking energy are improved. Reproduced with permission.^[69] Copyright 2018, National Academy of Sciences.

up to 35.2% of the total amount. More importantly, the relative abundance of the primary structure of spidroin significantly improves the toughness of the transgenic fibers, and especially increase the extensibility (Figure 21c,d).^[69]

Feeding Technique for Producing Functionalized Silk Fibers: The feeding technique is another *in vivo* method for producing intrinsically functionalized silk fibers. In comparison to the gene modification method, the feeding method is much more versatile and effective. Besides, this method can also be well understood within the framework of SF molecule crystallization theory. It is reported that fluorescent silk cocoons and fibers can be directly obtained by simply feeding silkworms

various small fluorescent molecules (e.g., rhodamine B, rhodamine 101, and rhodamine 110).^[72] It follows that all these small fluorescent molecules can directly conjugate with the SF molecules via molecular recognition.^[73] Thus, these small fluorescent dyes are trapped into the silk fibers along with the SF molecule crystals during the natural spinning process. Further structural characterization confirms that the secondary structure of silk fibers is modified via feeding.^[73] Specifically, micro-FTIR shows that there is no apparent structural homogeneity within silk fibers; such structural fluctuations might be the reason why these modified fibers display unsatisfactory mechanical properties (e.g., tensile strength).^[73]

Apart from the small fluorescent dye molecules, it is recently reported that some specific nanoscale materials, such as functionalized TiO₂ nanoparticles,^[74] single-walled carbon nanotubes (SWNTs), and graphene^[75] can also be directly conjugated into silk fibers by feeding silkworms artificial diets. Besides, these additives can largely improve the macroscopic performance of the composite silk fibers. For instance, it is determined that a 1% ratio of TiO₂ nanoparticles greatly enhance both the breaking strength and elongation of the composite fiber (Figure 22a).^[74] Besides, these functionalized TiO₂ particles can also endow the composite fibers with an anti-UV property (Figure 22b), which is extremely important for the long-term storage of silk fibers.^[74] Similarly, Wang et al.^[75] have obtained mechanically enhanced silk fibers by feeding *B. mori* larval silkworms with SWNTs and graphene (Figure 22c). In addition, the incorporation of graphene and SWNT can increase the conductivity of these fibers accordingly (Figure 22d).^[75] To quantify the influence of additives, a structural survey was also carried out, especially for second level. Because the α -helix and random coil are relatively softer than the β -sheet, a higher α -helix/random coil structure content should result in a material with a larger breaking tensile strength and modules with greater toughness. However, the content of β -sheet in the composite fibers is found to be relatively smaller than that of the natural control fibers, which suggests that the presence of SWNTs and graphene in the silk matrix may hinder the conformational transition from random coil/ α -helix to β -sheet.^[75] To some degree, this result is reasonable because of the fact that

the relatively large dimensions of SWNTs and graphene might give rise to a steric hindrance effect and consequently prevent the crystallization of SF molecules. However, this finding is in conflict with the hierarchical network structure model proposed in this review, which claims that a lower β -sheet content should be accompanied by a lower level of breaking stress. Nevertheless, the enhancement in breaking strength is reportedly more attributable to the presence of the relatively stronger mechanical additives (i.e., the SWNTs and graphene).^[75] Specifically, it is hypothesized that these additives in the silk matrix may act as “knots” (similar slipknot structure is widely found in other biological structures such as proteins and DNA strands),^[76] and act as a key frictional element, reshape the entire fiber, and dissipate the additional fracture energy, which consequently results in enhanced mechanical properties in the fibers. The inclusion of more additives in the composite fibers may not necessarily produce stronger fibers; on the contrary, it is determined that if excessive additives are incorporated into the silk matrix, such additives tend to aggregate and cause defects, which eventually results in silk fiber with an inferior mechanical performance.^[74,75] In summary, this natural feeding method is not only straightforward, but also effective. More importantly, this method can be easily scaled up and thus shed light on the massive production of reinforced silk fibers.

Forced Reeling of Natural Silk Fiber: As discussed, with an increase in the force reeling speed of both silkworm silk (Figure 23a,d) and spider MA fibers (Figure 23b), the mechanical performance, and especially the breaking stress values, can

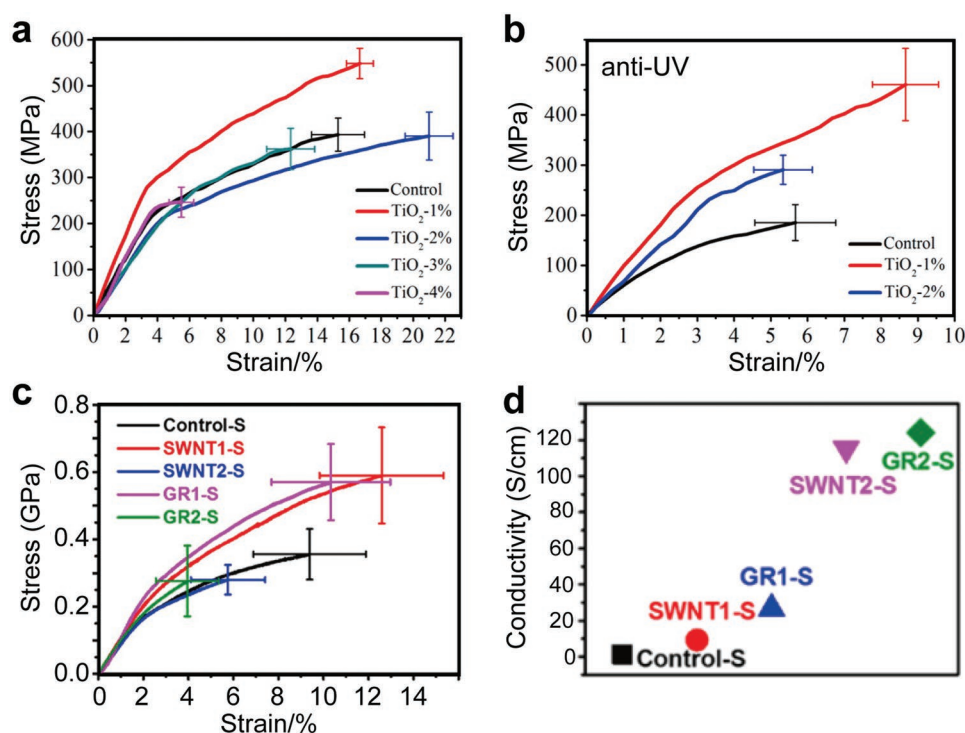


Figure 22. Production of functionalized silk fibers via feeding. a) Stress–strain curves of silk fibers produced by silkworms that have consumed TiO₂ nanoparticles. b) TiO₂ nanoparticles endow composite fibers with an anti-UV property. a,b) Reproduced with permission.^[74] Copyright 2015, American Chemical Society c) stress–strain curves of silk fibers produced by silkworms that have consumed normal and excessive amounts of SWNT and graphene. d) Electrical conductivity of carbonized silk fibers derived from different samples. The incorporation of graphene and SWNT can increase the conductivity accordingly. c,d) Reproduced with permission.^[75] Copyright 2016, American Chemical Society.

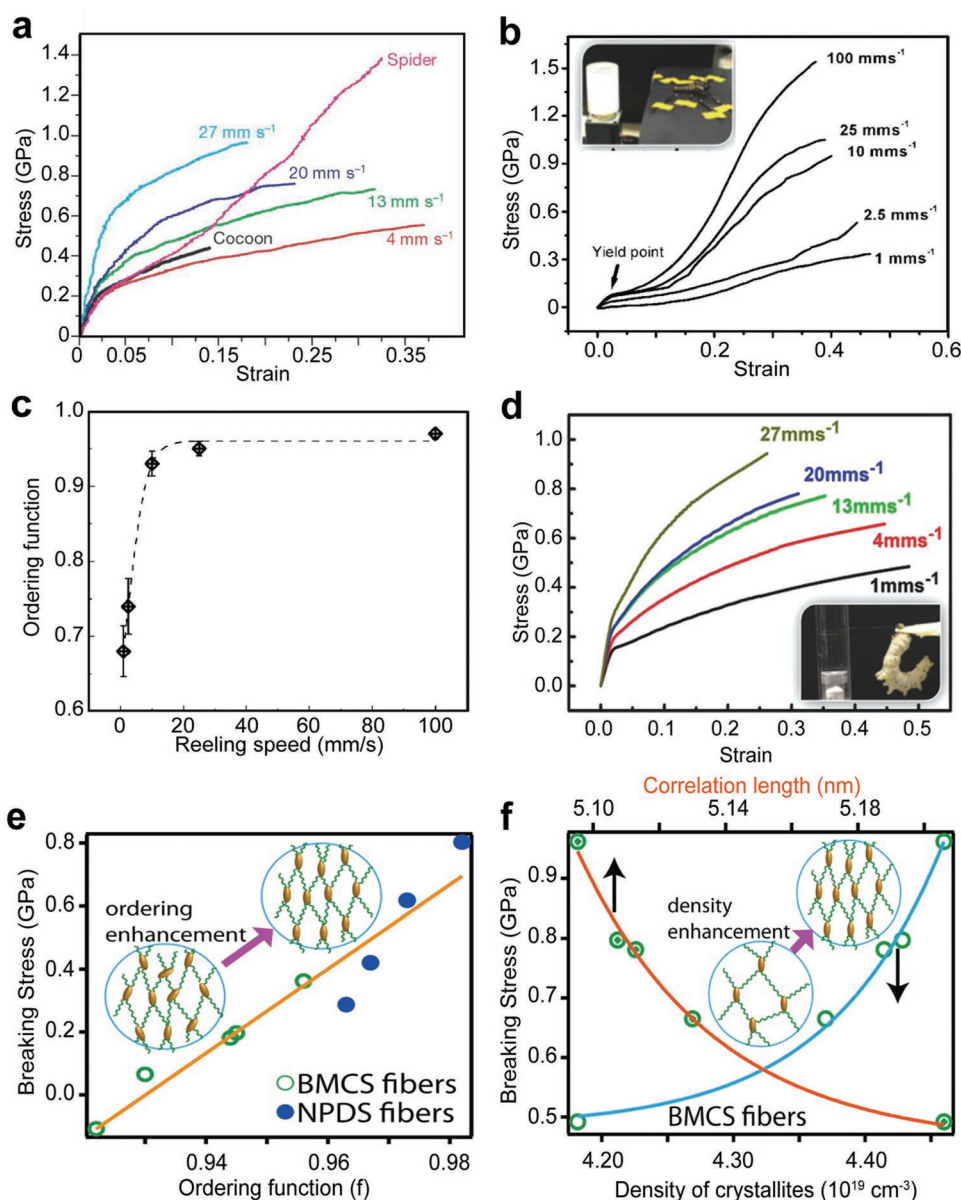


Figure 23. Influence of forced reeling speed on mechanical performance of fibers and orientation function. a) Silkworm silk fibers spun by forced reeling can be compared to spider fibers. Reproduced with permission.^[1] Copyright 2002, Springer Nature; b) spider MA dragline fibers under different reeling speeds. Reproduced with permission.^[25] Copyright 2015, Wiley-VCH. c) Orientation function of the force-spun silk fibers in (b) increases with the reeling speed. Reproduced with permission.^[46] Copyright 2006, Elsevier. d) Silkworm silk fibers under different reeling speeds. Reproduced with permission.^[25] Copyright 2015, Wiley-VCH. e) The influence of the ordering function of crystallites; the breaking stress of both BMCS fibers and NPDS fibers increases linearly with an increase in the value of f . Both fibers can be fitted by the same curve, which suggests that the strength of the two types of fibers is governed by similar structures, that is, the hierarchical network structure. f) The influence of the density and correlation length of the crystallites was observed; the breaking stress of both BMCS fibers increases exponentially with an increase in the density of crystallites but decreases exponentially with the correlation length. e,f) Reproduced with permission.^[11] Copyright 2016, Wiley-VCH.

be improved accordingly. Structural characterization reveals that it is the mesoreconstruction of the hierarchical structures, especially the level 3 and level 4 structures, that results in mechanical enhancement. Specifically, the crystallite size decrease monotonously with the acceleration of the reeling speed. Meanwhile, the orientation function and the density of crystallites increased (Figure 23c).^[11] Recently, Xu et al.^[23] have revealed that the key structural parameters, that is, f (orientation

function), n_{β} (the number of crystallites at the cross section of a nanofibril), A (effective loading area of a peptide chain in the β -crystallites), etc., were changed because of the reeling speed, consequently resulting in modifications in the toughness of silk fibers. In a similar way, Liu et al.^[11] also measured the orientation function and density of crystallites with varying the reeling speed, and quantitatively studied the correlation with the mechanical performance of silk fibers (Figure 23e,f).

5.1.2. Artificial Spinning of Regenerated Silk Fibroin Fiber Based on Homogeneous Nucleation

Although the above techniques can successfully produce mechanically enhanced natural silk fibers (neat or composite), the mechanical properties of the obtained silk fibers still to a large extent depends on the rearing conditions of silkworms. With the development of techno-polymer fibers based on petrochemicals, more and more efforts are devoted to artificially extruding strong and tough silk fibers from regenerated silk protein solutions. So far, electrospinning, dry-spinning, and wet-spinning techniques have been developed to successfully fabricate mechanically enhanced RSF fibers. Among these techniques, dry-spinning and wet-spinning techniques largely biomimic the natural silk fiber reeling process in vitro, in which the natural fibers are produced under benign and physiological conditions (i.e., at relatively ambient temperature, low hydraulic pressures, using water as the protein solvents). In particular, the wet-spinning technique, which is performed via the ejection of the spinning dope solution into some specific coagulation bath, is the most common and versatile approach; hence, we will comprehensively introduce it within the framework of the SF molecule crystallization theory in the following subsection.

Several prerequisite factors, such as dope concentration, pH, ion concentration, and proper shearing force (reeling speed) play an important role in determining the structure as well as performance of the RSF fibers, in a manner similar to that of the natural silk fiber spinning process. Besides, several other details of the RSF fiber extrusion system needs attention, including the category of solvents, molecular weight of dope proteins, constituents of SF solution, proper selection of coagulation bath, and treatment of post-drawing.

Molecular Weight: Unlike the natural spinning process in silk glands, where large amounts of dope proteins (with regular molecular weights) are stocked, the prerequisite factor to artificially wet-spin RSF fibers is the preparation of dope proteins with suitable rheological properties. This can be achieved by controlling the molecular weights of dope proteins. Take the wet-spinning of spider silk fiber as an example, due to spider cannibalism, it is very difficult to obtain substantial amounts of natural spidroin proteins directly from spider MA gland. Under these conditions, recombinant spidroin proteins with similar amino acid sequences can serve as surrogate proteins which are produced by heterologous hosts (e.g., *Escherichia coli*) on a large scale.^[77,78] Recently, it has been reported that although several recombinant spidroins with different molecular weights have been successfully used to spin artificial fibers, the mechanical properties are significantly distinct from each other. In particular, the as-spun fibers made using relatively smaller molecular weight dope proteins have displayed disappointing breaking stress levels (only around 200 MPa).^[79] However, when larger dope proteins were applied, the strength of the obtained as-spun fibers becomes greater, comparable to that of natural dragline silk.^[80] The use of dope proteins with even larger molecular weights might not necessarily be advantageous for spinning artificial silk fibers. In fact, recombinant spidroins with very high molecular weights are not soluble in aqueous solutions at high concentrations. They are more likely

to be dissolved in 1,1,1,3,3,3-hexafluoro-2-propanol (HFIP) solvents and become coagulated in either methanol or isopropanol atmospheres, the resulting products might be relatively less environmentally friendly. More importantly, these denaturing chemical environments might result in a folded hierarchical structure with an unsatisfactory mechanical performance.^[81]

Solvents: It is important to choose the proper solvents to dissolve SF proteins. Currently, there are three main categories of solvents, they are 1) organic solvents, such as formic acid, HFIP, and hexafluoroacetone (HFA), 2) ionic liquids including 1-butyl-3-methylimidazolium chloride (BMIM⁺ Cl⁻) and 1-ethyl-3-methylimidazolium chloride (EMIM⁺ Cl⁻), and 3) aqueous solvents. Notably, most of the aforementioned organic solvents either severely degrade the SF proteins or are too expensive and toxic for large-scale usage in industries. Besides, the mechanical properties of most as-spun fibers fabricated from organic solvents are unsatisfactory, except those of the fibers fabricated by Ha et al.^[82] in which they chose trifluoroacetic acid (TFA) as the solvent. Notably, the regenerated fibers exhibited a tenacity of 8.04 g per den and a breaking elongation of 6.79%. However, these fibers were still much thicker and rougher than natural silk fibers, and the cost of TFA was high.^[82]

The reason why ionic liquids can be applied to dissolve SF macromolecules lies on the ability of ionic liquids to disrupt the hydrogen bonding present between the SF chains. In this regard, the solubility of SF in different kinds of ionic liquids is determined by the identity of both the cation and anion, between which the anion playing a more important role.^[83] Specifically, the more the cation and anion participate in hydrogen bonding, the greater the solubility of the silk fibroin is. Compared with SF solution dissolved in organic solvents, a significant distinct is that once the ionic liquids are removed by rinsing with organic solvents or water, the SF molecules will spontaneously precipitate. On one hand, this feature endows the SF/ionic liquids solution the possibility of being produced into artificial silk fiber by wet-spinning and patterned silk film as scaffold. On the other hand, the ionic liquids can be recycled and applied for dissolving for the next time. Despite of the versatility of ionic liquids, it is noticed that the solubility of silk at room temperature is far behind satisfy. In principle, on the basis of the melting points of ionic liquids are relatively high (e.g., it is 65 °C for BMIM⁺ Cl⁻ and 89 °C for EMIM⁺ Cl⁻, respectively), silk dissolving experiments are usually performed at reasonably high temperatures.^[83] For instance, it is reported that silk fiber dissolved in *N*-methyl morpholine *N*-oxide (NMMO) very slowly at 95 °C, the silk fiber dissolution takes approximately 5 h before completion. With increasing temperature (e.g., from 95 to 120 °C), although the dissolving process becomes accelerated, such high temperature might induce a greater risk of the degradation of SF molecular chains during the solvation procedure.^[84] Consequently, the SF materials from such SF/ionic liquids solution are relatively poor in terms of the mechanical performances. Considering above disadvantage of ionic liquids, recently, some alternative ionic liquids with a lower melting point have been applied as the solvent. Among them, 1-allyl-3-methylimidazolium chloride (Amim⁺ Cl⁻), whose melting point is 17 °C, is conformed to be capable of dissolving silk more rapidly at a relatively low temperature.^[85] Besides, the obtained SF solution is quite stable. With proper

sealed at room temperature, the SF/Amim⁺ Cl⁻ solution can be stored for more than 1.5 years without any precipitation and gelation. It is worth mention that due to the hygroscopic nature of the ionic liquids, the dissolution process must be conducted under inert atmospheres and waterless conditions, which brings difficulties for dissolving silk fibers.

The application of aqueous solvents is environmental-friendly: they are the natural choice for fibers obtained from the silkworm gland and spider MA gland; more importantly, it can ensure that protein chains with high packing fractions are generated, in order to produce RSF fibers with outstanding toughness.

SF Solution Preparation: In natural silkworm silk glands, the concentration of the dope solution can be up to 30%. However, when regenerated fibroin aqueous solutions are applied as the dope solution during the wet-spinning technique, the concentration was much lower. To prepare RSF solutions, the conventional method, which usually involves the sequential processes of dissolution and dialysis, is complicated. Initially, the silk fibers obtained from cocoons are dissolved in concentrated aqueous LiBr solutions, after which they are dialyzed against deionized water, to ensure the removal of the small salt molecules. In principle, this method can only yield a dilute SF solution (with a concentration of 4–6 wt%). Because the ability to spin a polymer (in an aqueous solution) is significantly related to its viscoelasticity, which is concentration-dependent, the fabrication of RSF fibers requires the concentration of the dope solution to be greatly increased. To solve this problem, the initial dilute solutions require another reverse dialysis, by immersing dilute SF solutions into 25 wt% polyethylene glycol (PEG, 10 000 g mol⁻¹) solutions, so that the concentrated (specifically, the concentration is proportional to the reverse dialysis time) SF solutions can finally be obtained. To study the effect of the RSF dope concentration, Yan et al.^[86] monitor the tenacity and morphology of the RSF fibers spun from SF solutions with varied SF concentrations and confirm that when the dope concentration is below 11 wt%, only dispersed floccules instead of fibers are produced. With a 13 wt% dope solution, silk fibers are processed, but the cross sections are so irregular that they display numerous small voids on the surface. Besides, such RSF fibers are too weak in mechanical performance. Further increasing the concentration of the dope solution to 19 wt% enable moderately strong RSF fibers to be spun; such fibers have the smoothest appearance with a homogeneous and void-free cross section. Upon using a solution with an even higher dope concentration that exceeding 19 wt%, the spun fibers exhibit an irregular morphology and are very fragile.^[86] The same tendency is also observed when the dry-spinning technique is used to extrude artificial RSF fibers,^[87] although the concentration range of the dope solutions used is much higher (39.8–55%). These effects can be explained thoroughly within the framework of the “crystallization” model. Upon increasing the concentration of the dope solution (corresponding to a larger supersaturation level), the crystallization of the SF molecules in the crystal network is simultaneously promoted. However, if the level of supersaturation (i.e., >19 wt%) is very high, the local process of nucleation of crystallites will occur so rapidly that the amount of time available for the newly formed β -crystallites to reorient themselves into a well-aligned direction

become not enough. Consequently, this results into an uneven distribution of defects in the fibers and protein aggregations, which results in the production of fibers exhibiting an inferior mechanical performance.

During the dissolution process, aqueous LiBr solution (specifically, the lithium ions) is applied to break intermolecular hydrogen bonds, to tear the initially insoluble β -sheet apart and gradually to transform it into a random coil/ α -helix secondary structure so that the SF molecules become soluble in aqueous solutions. Thus, the presence of strong metallic ions can greatly influence the disassociation of SF molecules and consequently affect the molecular weight of the obtained RSF molecules. After the reverse dialysis process, components with low molecular weights were already excluded, while larger H-chain fragments were retained. Thus, the reverse dialysis process should positively affect the mechanical properties of the spun RSF fibers.

Constituents of SF Molecules: It is worth mentioning that although all the above methods can be successfully used to control the wet-spinning process, it is still challenging to spin advanced RSF fibers that retain the advantages of natural silk fibers, in terms of structural hierarchy and mechanical properties. Recently, Ling et al.^[88] have developed a facile bioinspired spinning strategy; they prepared the SF dope solution by partially dissolving silk fibers into micro-sized fibrils alone. This dope solution is not only highly viscous and stable, but also display a typical nematic liquid crystalline property, allowing it to be directly dry-spinning into artificial silk fibers as soon, immediately after it emerged from the spinning apparatus and being exposed to air gaps. Another fascinating property of this dope solution is that it maintains the hierarchical structures of natural silks, which is a key feature of natural protein fibers. They adopted the HFIP solution as a solvent and the concentrated dope solution containing micro fibrils (with diameters of 5–10 μ m and contour length of several hundreds to thousands μ m) is obtained after incubating silk fiber/HFIP (weight ratio, 1:20) mixtures at 60 °C for 7–15 days. Owing to the semiliquid property of the dope solution, the concentrated dope solution can flow through the spinneret, even under moderate external forces. Its semicrystalline property ensures that the dope solution is easily transformed into a solid-state fiber. The spun fibers retain the structural hierarchy as well as the orderly patterned silk nanofibrils network structure, which is critical for achieving the outstanding strength, extensibility, and toughness of natural silk fibers.^[88] Thus, the spun artificial fiber exhibit mechanical properties that are comparable to those of natural silk fibers, including a maximum average modulus of 11 \pm 4 GPa (the highest value can be up to 19 GPa), which is even higher than that of natural spider dragline silk (10 GPa, cf. Figure 24).

Coagulation Bath: During a typical wet-spinning process for the production of artificial fibers, the concentrated dope solution (in either organic solvents, aqueous or ionic liquids) is always directly injected into a coagulation bath.^[89] For example, it is reported that several solvents including methanol, acetonitrile, and water have been applied as the coagulation baths synthesizing RSF fibers spun from SF/ionic liquids solution. Accordingly, the methanol bath results into clear, solid fibers, the acetonitrile bath leads to crusted, white fibers, and the

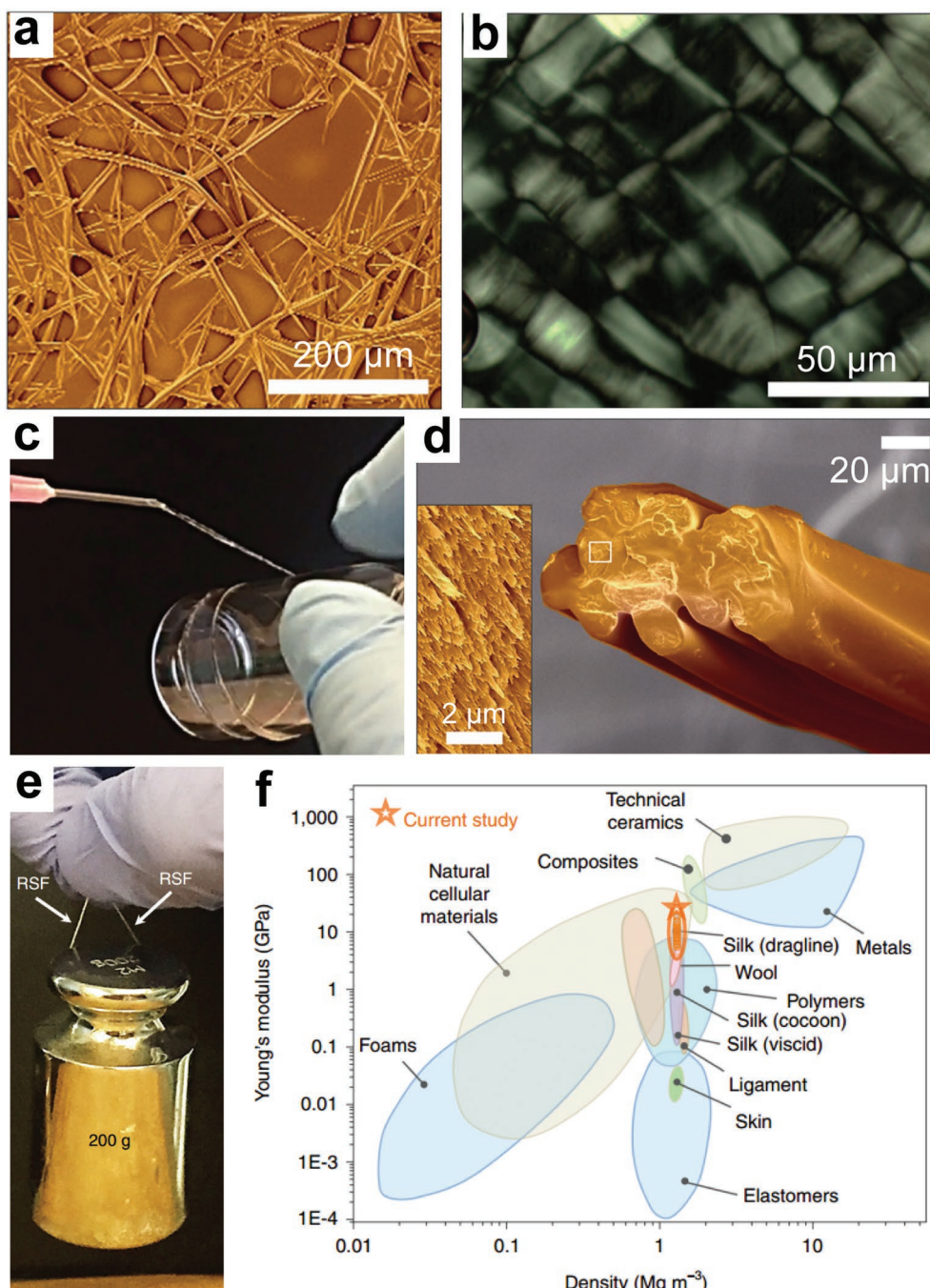


Figure 24. Visual appearance, structural characterization, and mechanical performance of the RSF dope solution containing microfibrils and the resultant RSF fibers. a) SEM image of the *B. mori* silk fiber/HFIP mixture; after incubation at 60 °C for 15 days, the silk fiber was partially dissolved to form microfibrils. b) Polarized light microscopy image of the RSF dope solution shows a liquid crystal-like texture. c) Photograph showing the facile bioinspired spinning process. The nematic mixture dope solution can be directly spun with hand to synthesize RSF fiber. d) SEM image of the cross section of the resultant RSF fiber; it is composed of highly oriented and bound microfibrils. The inset image is a high-resolution SEM image of a cross section of RSF fibers. e) A photograph showing a single RSF fiber (with a weight of 7 mg and length of 15 cm), which can bear a weight of 200 g without breaking. f) Comparison of Young's modulus and densities of RSFs with those of other materials. Reproduced with permission.^[88] Copyright 2017, Springer Nature.

water bath gives rise to fibers similar to the methanol bath.^[90] Apart from the morphology, the solvents used as coagulation bath also greatly affect the mechanical performance of the as-spun RSF fibers. In fact, only the fibers from methanol bath

can be gathered. RSF fibers from either acetonitrile or water bath adhere to the coagulation bath tank and are broken during removal.^[90] In principle, the purpose of usage of coagulation bath is to enhance the local concentration of the dope

solution (because the protein dissolves relatively slowly in the coagulation solution), which consequently facilitates the crystallization of β -sheet and β -crystallites.^[89] Many organic and inorganic compounds, including methanol, ethanol, isopropanol, *n*-butanol, glycol, glycerin, and various sodium, potassium, zinc, magnesium, and ammonium salts (chloride, sulfate, nitrate, phosphate, and acetate), have been used in the coagulation bath in case of wet-spinning RSF fibers from SF aqueous solutions. Within the framework of the crystallization mechanism, because of the correlation between structure and performance, a moderate coagulation rate is mostly useful for fabricating strong RSF fibers. If the coagulation rate (corresponding to slow crystallization kinetics) is too low, either the dope solution is not spinnable, or the hardly spun fibers exhibit an irregular cross section. On the other hand, if the coagulation rate is too fast (e.g., in methanol), the as-spun RSF fibers become brittle; this may be attributable to the poorly oriented patterns of the crystallites within the crystal network. In comparison, when a moderate coagulation rate (e.g., in ammonium sulfate solution) is applied, the crystallization of both β -sheet and β -crystallites can occur, and the amount of time available for the newly formed crystallites to reach their optimal directions is sufficient, which consequently contributes to a greater level of toughness. In principle, the category of the coagulation solution is not the only determining factor, the concentration and operation temperature also affect the morphology and mechanical performance of the as-spun RSF fibers. For example, it is found that the morphology of the RSF fibers is worse upon using a 40 wt% solution of ammonium sulfate, as compared to that observed upon using a 30 wt% solution. In addition, more microvoids are also clearly observed in RSF fibers formed in the 40 wt% coagulation bath.^[86] Again, this tendency is consistent with the excess crystallization rate (and water removal rate) in relatively concentrated coagulation baths. Although the wet-spinning technique is rather successful for fabricating artificial RSF fibers, it still differs from the natural spinning process, where the natural fiber extrusion occurs in the air gap, instead of in the solution. In other words, if the coagulation process occurs in the air, this artificial spinning technique can be referred to as the dry-spinning technique. Recently, the dry-spinning technique has attracted significant interest and has been developed significantly. For instance, Wei et al.^[87] have developed a capillary spinning equipment for the dry spinning of RSF fibers. They also comprehensively investigated the effects of different spinning conditions (including metallic ions, pH, dope concentration). It is confirmed that a similar tendency is observed with regard to the mechanical performance; if the dope solution has a moderate pH ranging from 5.2 to 6.9, it mostly results in spinnable fibers, especially for the dope solution with a pH of 6.0 and 0.3 M calcium ions are incorporated.^[87]

Post-Treatment: RSF fibers coagulated in the coagulation bath (usually referred to as the as-spun fibers) are still relatively fragile. This is due to the relatively low crystallinity as well as the poor orientation function of crystallites within the crystal network, which had been proven by the experimental data using Raman spectroscopy,^[87,91] synchrotron radiation X-ray microdiffraction, and birefringence measurements.^[92] In fact, the characteristic crystalline structures are barely monitored

and only roughly random patterns of crystallites are characterized in the as-spun fibers. Hence, post-treatments need to be performed, either post-draw in the air gap or in solution, and steam annealing should be applied to make the as-spun RSF fiber stronger, as it increases the crystallinity as well as the orientation function of the crystallite network. Zhou et al.^[91] and Sun et al.^[92] have comprehensively studied the influence of post-draw-down ratios on the morphology and mechanical properties of wet-spun and dry-spun RSF fibers, respectively, from the perspective of performance of different hierarchical structures. According to Zhou et al.,^[91] post-draw treatment can dramatically improve the morphology of the as-spun RSF fibers. For instance, the surface of the post-treated RSF fibers displays a smooth and highly lustrous appearance. Besides, the diameters of these final fibers not only become smaller, but also become more uniform, as compared to those of the as-spun components. More importantly, it appears that fewer voids and pores exist in the post-treated RSF fibers, with the toughness improved greatly.^[91] To quantify the effect of post-draw treatment on the mechanical enhancement of RSF fibers, the molecular structure of RSF fibers is studied in detail.^[81] For instance, Zhou et al.^[91] have applied different post-draw ratios on a series of as-spun fibers, and reported that simply increasing the ratios from 1 to 6 lead to a progressive increase in the molecular alignment. In addition, they also confirm that the post-draw treatment lead to better-oriented β -sheet secondary structures as well as a greater level of crystallinity in fibers.^[91] Obviously, these aforementioned changes in the mesoscopic structure should generate robust RSF fibers. The changes observed after post-draw treatments are observed not only for the wet-spinning technique but are also observed for the dry-spinning technique. Increasing the draw-down ratios results in larger crystallinity levels and a better degree of molecular orientation, both in the crystalline and amorphous regions. In addition, Sun et al.^[92] further confirm that the crystallites in the dry-spun RSF fibers become smaller with an increase in the draw-down ratios. Again, these findings can be explained thoroughly by the crystallization mechanism and hierarchical network structures of silk materials. Owing to the above changes in the mesoscopic structure, the post-treated RSF fibers exhibit a drastic improvement in the breaking stress. For instance, the average breaking stress of wet-spun RSF fibers with a draw-down ratio of 6 can be up to 0.45 ± 0.02 GPa, which is comparable to natural-spun silk fibers (Figure 25c).^[86] As for the dry-spun RSF fibers, the post-draw process with a draw-down ratio of 4 significantly improves the breaking stress of the obtained RSF fibers, that is, from 45.7 to 326.7 MPa (Figure 25d).^[92]

5.1.3. Artificial Spinning of Composite RSF Fiber Based on Heterogeneous Nucleation

In general, there are two different methods for the reinforcement of artificial RSF fibers. One involves the control of the spinning process, as discussed above, in which the neat SF solutions are applied as the feedstock. The other method involves the addition of some specific reinforcement agents or foreign nanoparticles into the dope solution, to extrude composite RSF fibers. By activating the heterogeneous nucleation of the SF

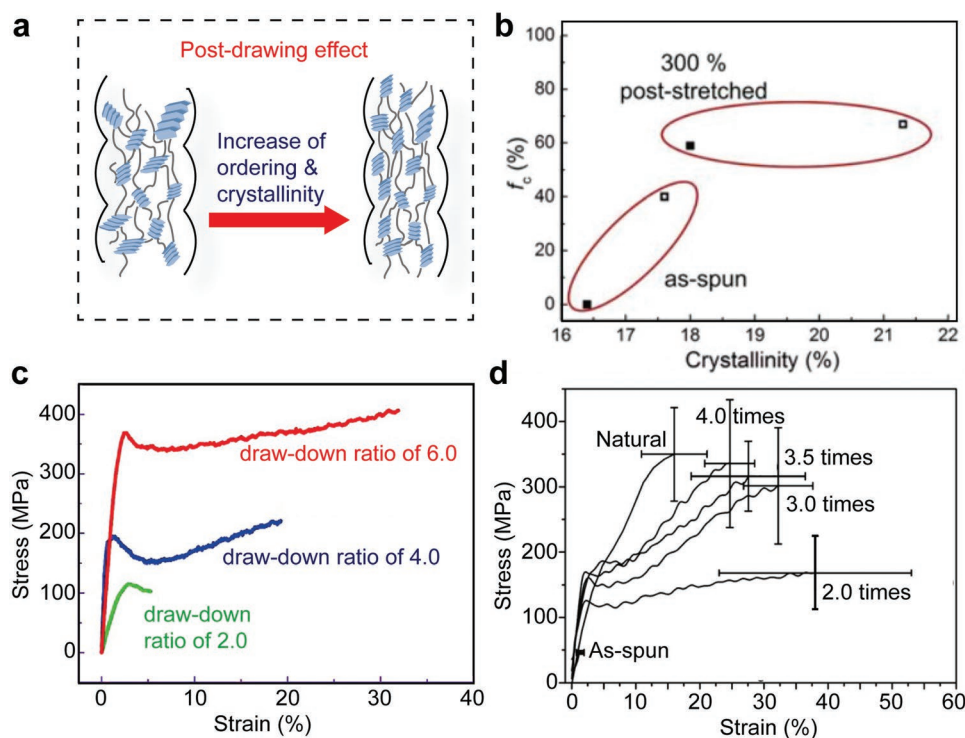


Figure 25. Influence of post-draw ratios on the structures and stress–strain profiles of RSF Fibers. a) Schematic illustration of the effect of post-draw treatment on the molecular crystal network. b) Post-draw treatment increases the crystalline orientation and crystallinity. Reproduced with permission.^[81] Copyright 2016, Springer Nature c) Post-draw ratios increases the mechanical performance of wet-spun RSF fibers. Reproduced with permission.^[86] Copyright 2010, American Chemical Society. d) Post-draw ratios increases the mechanical performance of dry-spun RSF fibers. Reproduced with permission.^[92] Copyright 2012, Royal Society of Chemistry.

molecules, the nucleation barrier can be suppressed, thereby increasing the probability of crystallization, which consequently results in a higher crystal density and smaller correlation length of the molecular crystal networks within the composite RSF fibers. Thus, mechanically enhanced RSF fibers can be synthesized. So far, this method has successfully been used to fabricate several significantly reinforced composite RSF fibers (or mats). For instance, Chen et al.^[12] reported that by simply mixing the dope solution with certain foreign particles (specifically referred to as nanoscale particles that can interact with SF molecules, such as monodispersed polystyrene (PS) nanoparticles (NPs), graphene, silica NPs, and nanocrystal cellulose), the macroscopic performance of the wet-spun composite RSF fibers can be programmed. According to the results, PS NPs can mostly improve mechanical performance due to the perfect spherical shape, smooth surface, uniform particle size, and most importantly, the strong interactions with SF molecules.^[12] Within the framework of the crystallization mechanism, this affinity interaction between PS NPs and SF molecules (specifically referred to as the intermolecular hydrogen bonds between the carboxyl groups on the surface of PS NPs and amino groups within SF peptide chains) can significantly decrease the surface tension and lower the nucleation barrier. Thus, the heterogeneous nucleation of SF molecules is greatly promoted on/near the surface of PS NPs, which results in the generation of more nucleation sites (corresponding to a larger crystal density within the spun RSF fibers). As discussed before, both natural silk fibers and RSF fibers exhibit strong internanofibril

interactions. Consequently, this increase in density will result into stronger fibers. As shown in **Figure 26b**, the incorporation of PS NPs within a certain range do improve both the toughness and breaking stress of the composite RSF fibers; Specifically, the addition of more PS NPs leads to stronger fibers. According to their statistical data, the breaking strength (Figure 26c) and elastic modulus of composite RSF fibers is nearly doubled than neat RSF fiber, indicating that this method for performing manipulation by triggering heterogeneous nucleation is feasible and effective.

Apart from the aforementioned nanoparticles, other functionalized composite RSF fibers (or mats), such as those containing multiwalled carbon nanotubes (MWNTs),^[93] hydroxyapatite (HAP) nanoparticles,^[94] and cellulose^[95] have also been successfully fabricated using the electrospinning technique. It is further reported that the improvements caused by the incorporation of foreign additives on the breaking stress of composite RSF fibers might occur at relatively low concentrations, as compared to that observed for PS NPs. For instance, the incorporation of MWNTs can significantly enhance the composite fiber toughness, when the concentration is <1 wt%. A further increase in the ratio of MWNTs might result in an inferior mechanical performance (Figure 26d). Besides, it is notable that not all additives are beneficial for the heterogeneous nucleation for SF molecules.^[93] On the contrary, some of the additives has a high tendency of self-assembly. In this condition, when mixed such additive with SF dope solutions, large clusters (or aggregates) of additives will form

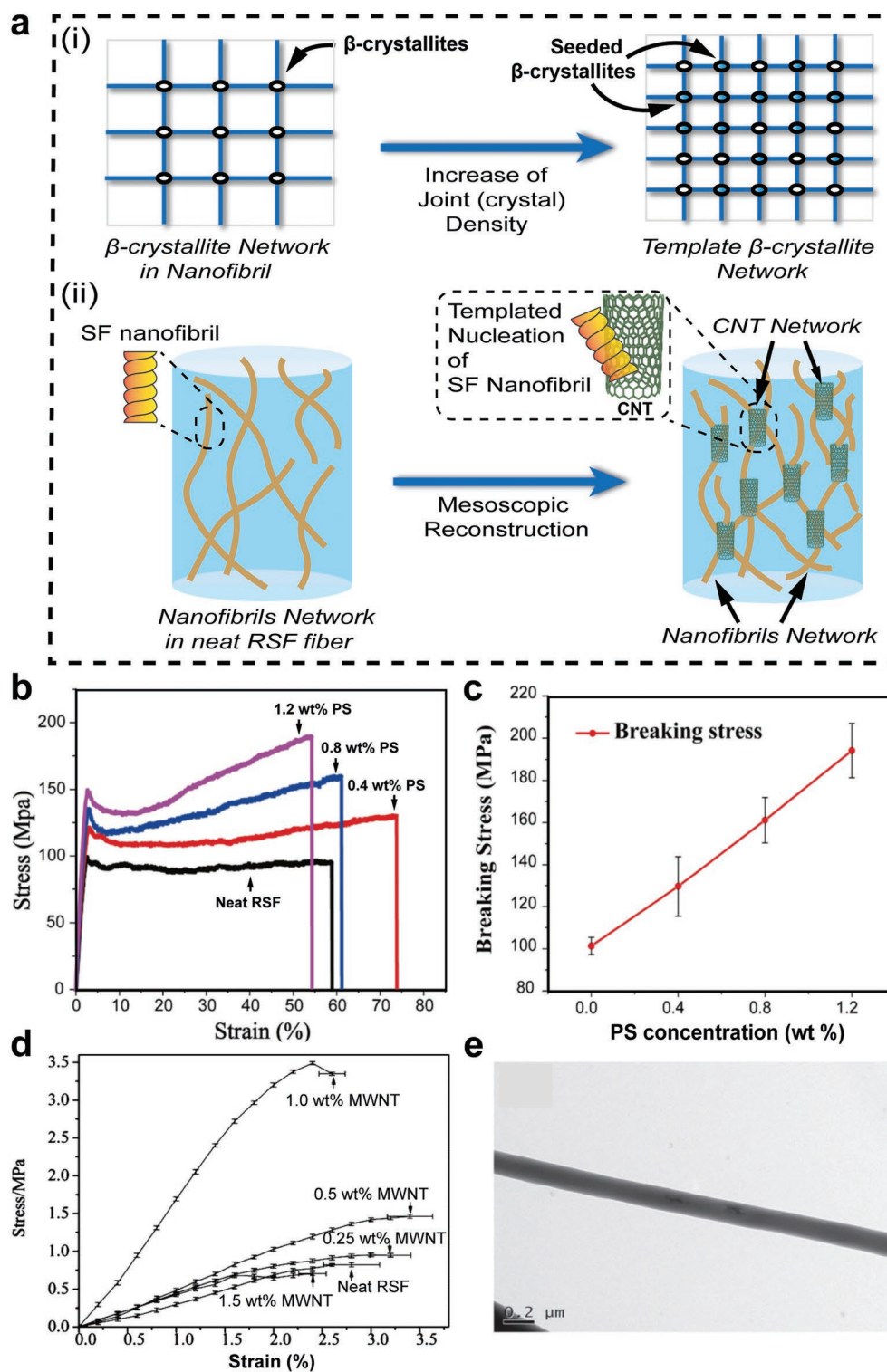


Figure 26. a) i: Schematic illustration of the effect of templated (heterogeneous) nucleation which substantially increases the density of crystallites within the molecular and nanofibrils networks; this will significantly increase the joint (crystals) density of the networks. ii) Schematic illustration of the CNTs templating nucleation of SF nanofibrils. CNTs will give rise to the mesoscopic reconstruction of the nanofibrils network, b) stress–strain curves of RSF fibers containing various concentrations of PS NPs. The addition of 1.2 wt% of PS will double the breaking stress of regenerated SF fibers. c) The correlation between the breaking stress of RSFs and concentration of PS NPs. b, c) Reproduced with permission.^[11] Copyright 2016, Wiley-VCH; d) stress–strain curves of RSF mats containing different ratios of MWNT. Reproduced with permission.^[93] Copyright 2012, American Chemical Society; e) TEM images of SF/HAP composite fibers after effective surface treatment. No HAP aggregation was observed on the surface. Reproduced with permission.^[94] Copyright 2014, Elsevier.

spontaneously, which lead to defects and result in the generation of fibers that are inferior to composite RSF fibers. Hence, a uniformly dispersed mixture solution is essential. Normally, small ratios of surfactants can be incorporated into the mixture to increase the dispersion of additives. Upon performing this procedure, the obtained composite RSF fibers can generally display a bead-free nanofiber morphology that does not exhibit any aggregation of additives^[94] (Figure 26e) and the mechanical properties are improved accordingly. Further structural analyses have clearly shown that such composite RSF fibers have a larger β -sheet and β -crystallite content than neat RSF fibers.^[93] Another notable finding is that the blending of SF with other functionalized additives is an effective method for endowing RSF fibers with the unique advantages associated with the incorporated additives, especially with regard to the biological aspects.^[93–95]

5.2. Non-Fibrous Silk Materials

Owing to the enhanced biocompatibility, controllable degradation rate, and unique optical and electronic properties, SF molecules have become promising building blocks for next generation green biomaterial devices. Natural silk fibers have been adopted for centuries and several efforts have been made to describe the relationship between the mesoscopic structure and macroscopic performance. The relevant studies not only comprehensively enhance our insight into silk fibers, but also lead to the transformation into a large variety of non-fibrous silk material formats, including membrane/films, hydrogels, and scaffolds.^[5,96,97] In a manner similar to that observed for silk fibers, the factor distinguishing non-fibrous silk materials from other biopolymers used in high technology applications is the fact that the robust mechanical properties of silk materials can also be process-dependently programmed at the mesoscopic level. In this section, we will describe some methods for fabricating some non-fibrous silk materials in detail, and discuss the conditions accordingly required for mesoscopic engineering. Besides, we will prove that such methods are not empirical; on the contrary, the hidden mechanisms can be explained thoroughly in terms of crystallization theory.

5.2.1. SF Film

SF films have been successfully fabricated from SF solutions, in which SF molecules are dissolved either in aqueous, organic solvents, or ionic liquids. In case of SF/ionic liquids solutions, they can be used to cast films on different substrates. Once the ionic liquids are removed by rinsing with organic solvents including acetonitrile or methanol, the SF molecules turn into SF film spontaneously. In principle, the rinsing solutions will to a large extent determine the structure as well as mechanical performance of the obtained SF film. For instance, the methanol-rinsed film exhibits a large crystallinity that is comparable to the natural fiber. The acetonitrile-rinsed SF film, on the other hand, displays a relatively smaller content of crystallites.^[83] As for SF aqueous solutions, two conventional methods producing SF films are by casting and spin-coating.

The basic principle is that the removal of solvent molecules from SF solutions can consequently increase the local concentration (supersaturation) of SF molecules, and finally lead to phase separation and crystallization. For example, while using the casting method, the SF molecules dispersed in solvents still exhibit an amorphous/ α -helix conformation, so that they are soluble and free to move. Gradually, upon the evaporation of non-bound solvent molecules, SF molecules are pushed toward each other, consequently crystallization and solidification are triggered and finally SF films are synthesized. As for the spin-coating method, apart from solvent evaporation, the shear force during spinning also has significant effects on the kinetics of SF molecule crystallization.^[98] Recently, several novel advanced methods are developed to synthesize ultrathin SF films or special SF films with a controlled thickness, desired morphology, and unique applications. For instance, Bressner et al.^[99] reported about a so-called “electrogelation” method, in which some anodes (with closed-loop structure) are used as templates and an electric field is then applied to trigger the sol–gel transformation of SF molecules; finally, upon drying, an optically transparent SF films are formed. Owing to the unique curved geometry of the anode templates, the most fascinating advantage of this method is that the obtained SF films can exhibit a designed morphology.

Jiang and Tsukruk^[100] have developed an advanced spin-assist layer-by-layer (SA-LBL) method to achieve a precise control over the thickness of SF films. The thickness of SF films can be precisely modulated by simply controlling the number of layers they contain. Wang et al.,^[101] who used a similar experimental design, report about a “stepwise deposition” (or dip-coating) LBL method for the synthesis of SF films with a controlled level of thickness. They immerse different substrates into the SF dipping solution for 2 min at room temperature and then wash away the excess solution with deionized water or methanol/water. This combination of the dipping and washing procedures is referred to as an individual step, and by repeating the desired number of the aforementioned steps, the thickness of the obtained SF films can be controlled conveniently.

The macroscopic performance of SF films, which is attributed to the same structural building blocks and similar hierarchical structural factors, is also largely determined by the mesoscopic structures. Specifically, the alterations in the crystallinity of SF films can result in a distinct mechanical robustness as well as degradation rates. The content of secondary structures, on the other hand, is directly correlated to the oxygen and water molecule permeability.^[102] Thus, engineering the structures of SF films is of utmost importance. So far, several methods have been proposed for the structure reconstruction of SF films, including treatment with methanol/ethanol or other organic solvents (Figure 27a), blending with other polymers (Figure 27b),^[103] control of SF solution conditions,^[101] post-treatment with water steam, and application of uniaxial extension (Figure 27c).^[104] To the best of our knowledge, all these engineering methods can all be explained thoroughly within the framework of the crystallization process.

Similar as the as-spun RSF fibers, the freshly prepared SF films are still fragile because of the relatively low content of crystallites. To further strengthen such SF films, a methanol treatment is usually applied. As discussed earlier, methanol treatment promotes the conformational transition of a SF

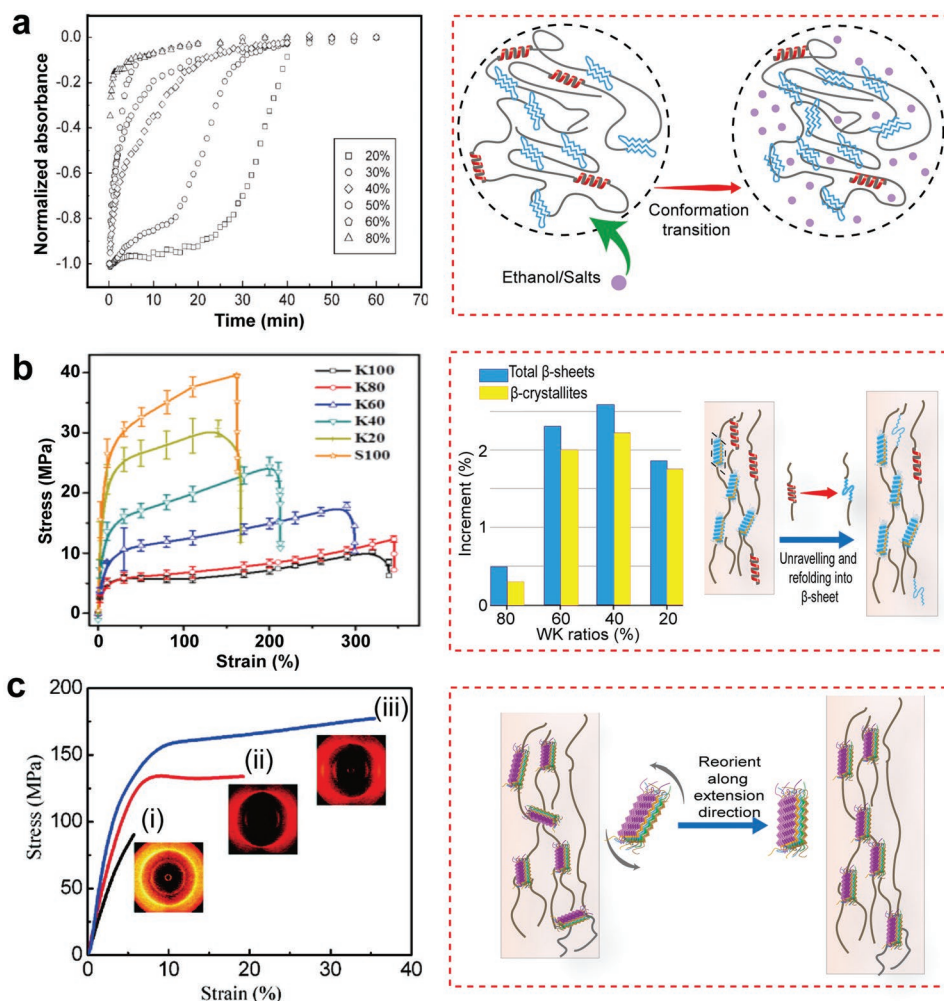


Figure 27. a) Influence of ethanol treatment on β -sheet content. The incorporation of ethanol would push SF molecules closer and give rise to a conformational transition. Reproduced with permission.^[48] Copyright 2007, Wiley-VCH. b) The mechanical performance of SF/WK composite films can be altered by changing the ratios of WK. The WK α -helix can interact with the SF molecules and promote the formation of β -sheets and β -crystallites, which consequently alter the performance. Reproduced with permission.^[28] Copyright 2016, Wiley-VCH. c) Representative stress–strain curves of SF films before and after extension. The inset exhibits 2D WAXD patterns, which suggests that the orientation function was improved upon extension. i) Obtained film, ii) film exhibiting twice the level of extension, and iii) film exhibiting thrice the level of extension. Reproduced with permission.^[104] Copyright 2010, American Chemical Society.

molecule from a random coil/ α -helix to a β -sheet. In other words, this treatment is beneficial to the crystallization process and consequently leads to the reinforcement of the obtained SF films. To some degree, the role of this methanol treatment is similar to that of the coagulation bath used for spinning RSF fibers. The use of uniaxial extensions on SF films (at the wet/swollen stages) is comparable to that of post-draw procedures in the spinning technique. The corresponding WAXS patterns on stretched SF films clearly indicate that stretching can significantly lead to well-aligned patterns of molecular chains within SF films (in a direction parallel to that in which uniaxial stretching occurs). In this regard, the stretched SF films become mechanically enhanced (Figure 27c).^[104] Wang et al.^[101] comprehensively investigate the effects of many factors influencing the results of the “dip-coating” engineering method, including the concentration of the SF solution, incorporation of metallic ions, and proper choice of substrates. Obviously, the thickness of the

obtained SF films (which can correspond to the total amount of deposited SF molecules) should increase with an increase in the concentration of the SF dipping solution. Besides, within a certain concentration range, the efficiency of dip-coating is also proportional to the concentration of the incorporated metallic ions (e.g., sodium ions). Moreover, it is proven that after replacing hydrophilic substrates with hydrophobic components, enhanced deposition is achieved. These findings remain consistent with the classical mechanism of protein crystallization. As discussed previously, intermolecular interactions (especially hydrophobic interactions between the hydrophobic domains within SF chains) are the primary physical driving force that lead to the crystallization of β -sheets and crystallites; similarly, hydrophobic interactions are also the primary force used to anchor SF molecules in solutions onto substrates. In this case, hydrophobic substrates are more favored due to the relatively stronger hydrophobic interactions with SF molecules. The incorporation of salt

into the SF dipping solution, on the other hand, increase the local electrostatic attractive interactions between SF molecules and consequently supplement the total attractive interactions, which in turn favors crystallization.

Because of the advantages of composite RSF fibers, methods for blending neat SF solutions with other specific polymers (such as wool keratin, WK) and synthesis of composite SF films with a tunable performance are also proposed and greatly developed. For instance, SF/WK composite films that have a high tensile strength and are biodegradable can be developed by simply adjusting the ratios of SF versus WK.^[28] Structural characterization show that modifications in hierarchical structures affect the mechanical performance. Specifically, it is shown that an increase in the SF ratios of composite films can increase the density of β -crystallites; this consequently enhances the toughness and decreases the biodegradation rate. In comparison, an increase in the ratio of WK can increase the extensibility and ability to recover from any deformation.^[28]

5.2.2. SF Hydrogels

Hydrogels generally refer to a series of materials with a typical 3D structure that can partially swell but cannot dissolve on exposure to aqueous solutions. Owing to the porous architecture, great biocompatibility, and controllable degradation rate, hydrogel-based biomaterials represent an important alternative that can be useful for developing tissue engineering and cell/drug delivery applications.^[96,97] SF hydrogels, which can be spontaneously formed from SF solutions, have also been proven to be good candidates. Previously, the conventional process of gelation of SF solutions occur at a relatively low pH, high temperature, or high ionic environment. However, at the above conditions, the SF gelation process usually occurs slowly, which lasts from a few weeks to months. Recently, a lot of efforts have been devoted to the development of advanced and controllable SF hydrogelation techniques.

In principle, the gelation process is initialized by polymer chain crosslinking (either chemically, physically, or both); as a result, the obtained hydrogels should typically exhibit a network structure. It is reported that the intermolecular interactions (e.g., the hydrophobic interactions and hydrogen bonds) of SF hydrogels promote sol–gel transition kinetics, and that the β -sheet crystallites serve as the main physical crosslinkers that made SF hydrogels adequately stable. The mechanical properties of SF hydrogels are similar to those of SF fibers and are highly structure-dependent. The structure of SF hydrogels can be examined thoroughly using the characterization techniques mentioned in 23. The rheometer is also an ideal tool to conveniently monitor gelation kinetics as well as to measure the modulus of an SF gel. In addition, SEM/TEM/AFM imaging techniques can further be applied to record the process of morphological evolution during SF hydrogelation. For instance, Nguyen et al.^[25] have revealed that during the early stages of SF hydrogelation (during ultrasonication), the formation of protein aggregates and nanofibrils is observed, followed by nanofibril growth and continuous interconnectivity between some nanofibrils network domains. The hierarchical structure of silk materials shows that each individual nanofibril is a network of

molecular crystallites. Knowledge regarding the crystallization process will provide comprehensive insight into SF hydrogelation kinetics and techniques that can be used for the manipulation, so that the structures and performances of SF hydrogels can consequently be programmed.

To perform hydrogelation in a rapid and controlled manner, the techniques that have proven effective include vortexing (shearing),^[105] ultrasonication,^[25,106] direct electrical current (electrogelation) application,^[107] incorporation of specific metallic ions or surfactants,^[108–110] controlling of SF solution conditions (e.g., pH and concentration),^[109] and blending with specific polymers or nanoparticles.^[28,109] All of these techniques can be used to synthesize relatively weak SF films in a short period of time. **Figure 28a** shows several typical SF hydrogel fabrication methods. Among these, the vortex method is the simplest, and it avoids the direct contact between the SF solution and other probes (especially probes used in ultrasonication or electrogelation techniques). The principle of the vortex method relies on the use of vortex-induced shearing force with a characteristic gradient. It is reported that the vortexing of neat SF solutions for 2 min can lead to a detectable increase in the β -sheet content as well as the turbidity of the solution (this suggests the occurrence of large amounts of crystallites and a uniform dispersion). To precisely control the kinetics of this hydrogelation process (sol–gel transition can be regarded as crystallization), the vortexing time, temperature, and the concentration of SF solutions need to be controlled. Specifically, the duration of the hydrogelation process can be varied from minutes to hours.

Gelation will occur spontaneously when the SF solution is exposed to a relatively low direct current, in a manner similar to that of the “electrogelation” process, based on the SF film fabrication technique. The obtained SF hydrogels are stable enough to retain the functions.^[107] It is reported that such electroinduced sol–gel transitions can be reversed by simply changing the DC voltage polarity, that is, the obtained fresh gel can dissolve back into a solution upon being subjected to DC current with opposite polarity (Figure 28b).^[107] Apart from electric fields, many other stimuli can also manipulate the SF gelation process (crystallization). Among these, ultrasonication is powerful due to its diverse physical and chemical effects. Recently, Nguyen et al.^[25] have developed an advanced ultrasonication-based method for fabricating SF hydrogels that can precisely control gelation kinetics. The role of ultrasonication within the SF protein crystallization framework is that it can create abundant nucleation centers (also known as nucleation seeds) in the SF solution (Figure 28c), which accelerates the crystallization of β -sheets as well as β -crystal networks (nanofibrils). Besides, such nucleation seeds also give rise to different mesoscopic structures and different storage modulus of SF hydrogels. According to the results, ultrasonication significantly affects SF crystallization kinetics. For instance, while monitoring the crystallization process via AFM imaging, it is found that even after performing ultrasonication only for 30 seconds, a dilute RSF solution (0.04 wt%) can display many nanofibrils. However, in ultrasonication-free conditions, the occurrence of nanofibrils becomes significantly rarer. To gain more insight into the effects attributable to ultrasonication parameters (such as the power and exposure time), Nguyen et al.^[25] used a rheometer to quantify the gelation kinetics as well as to compare the mechanical properties. It is clearly revealed

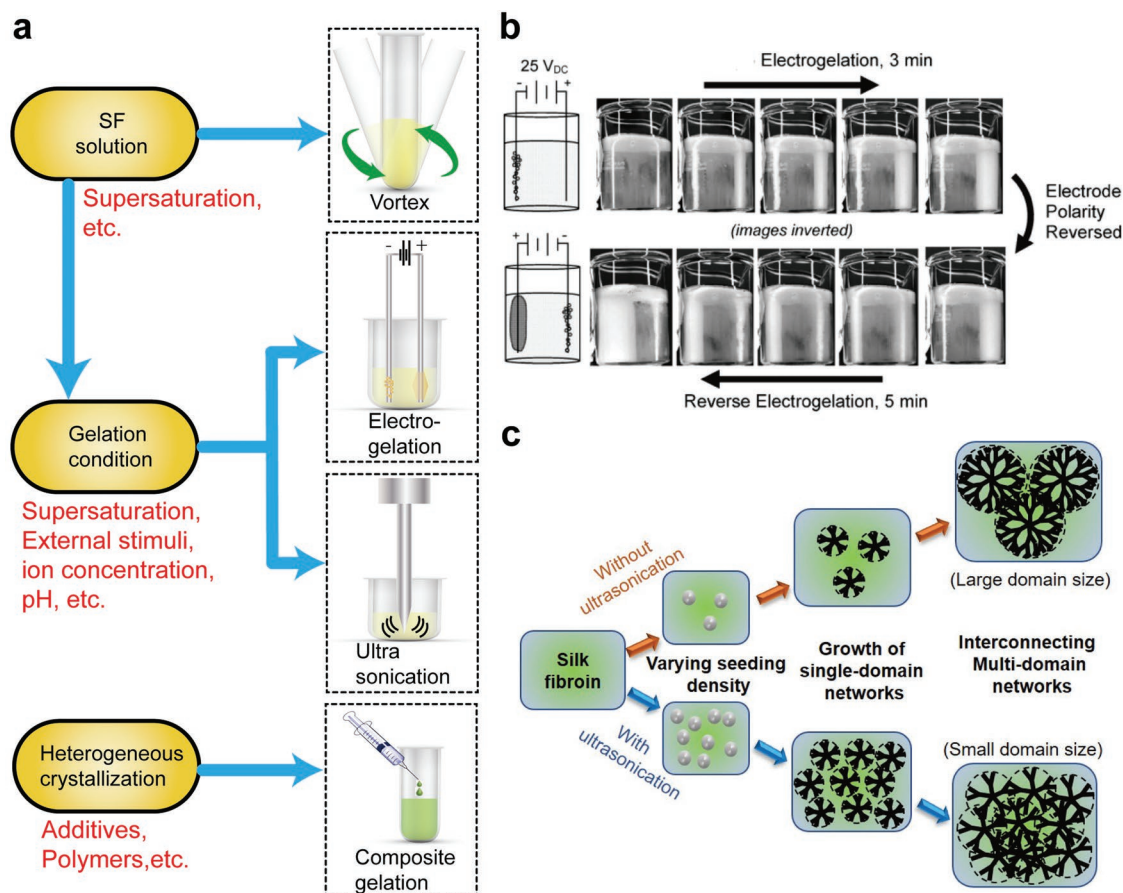


Figure 28. a) Methods for preparing SF hydrogels and the corresponding factors influencing the crystallization kinetics. b) Silk e-gel process applied to an 8 wt% silk aqueous solution after applying 25 V DC, using mechanical pencil-lead electrodes. Over 3 min, the gel is formed around the positive electrode and gas is released at both electrodes; however, the gelation process is reversed with the application of reversed polarity DC voltage. Reproduced with permission.^[107] Copyright 2010, Wiley-VCH. c) Influence of ultrasonication on the crystallization of SF proteins into hydrogels and the corresponding structures, upon varying the density of nucleation centers.

that a longer ultrasonication duration can shorten the gelation time (defined as the time where storage modulus abruptly increases) and increase the densities of nanofibril domains. Because SF hydrogels are formed by weak nanofibril–nanofibril interactions, such an increase in the nanofibril density (with an increase in ultrasonication time) consequently leads to an inferior storage modulus, as shown in **Figure 29c**.

By comparing the gelation time, the effects of environmental factors on SF hydrogelation (crystallization) kinetics can also be quantified. For instance, it is reported that the gelation time decreases with a decrease in pH and increase the hydrogelation temperature (**Figure 30b**), SF protein concentration (**Figure 30c**), and amount of added calcium ions (**Figure 30d**).^[109] All these findings are consistent with the crystallization mechanism for SF molecules (cf. **Figure 30a**). Heterogeneous crystallization is similar to the crystallization observed for composite RSF fibers and SF films, and the mixing of a neat SF solution with some specific foreign additives can also result in the engineering of mesoscopic structures of SF hydrogels. For instance, Chen et al.^[12] reported that the incorporation of PS NPs in proper ratios can significantly shorten the hydrogelation process and lead to a relatively weaker storage modulus in SF hydrogels.

5.2.3. SF Porous Scaffolds

Biocompatible scaffolds are widely applied in areas such as tissue engineering. In general, typical 3D structured scaffolds should satisfy at least the following requirements: first, the mechanical stability should adequately enable cell attachment and proliferation to occur. In fact, mechanical strength is of the utmost importance for the maintenance of utility of scaffolds, especially when they are applied for bone tissue regeneration. Second, the degradation rate of biocompatible scaffolds should be controlled to ensure that it is comparable to the growth rate of new tissues. In addition, porosity is another important parameter that can ensure the occurrence of cell migration as well as nutrient and waste transportation. Owing to the good inherent biocompatibility of these materials, the adjustable mechanical performance, and degradation rate of silk materials, SF scaffolds have already become attractive candidates for a broad range of tissue engineering applications.^[111]

In the past few decades, great efforts have been devoted to study the processability of 3D structured highly porous SF scaffolds. They have so far been successfully fabricated from RSF solutions via different methods. Among these, the most widely

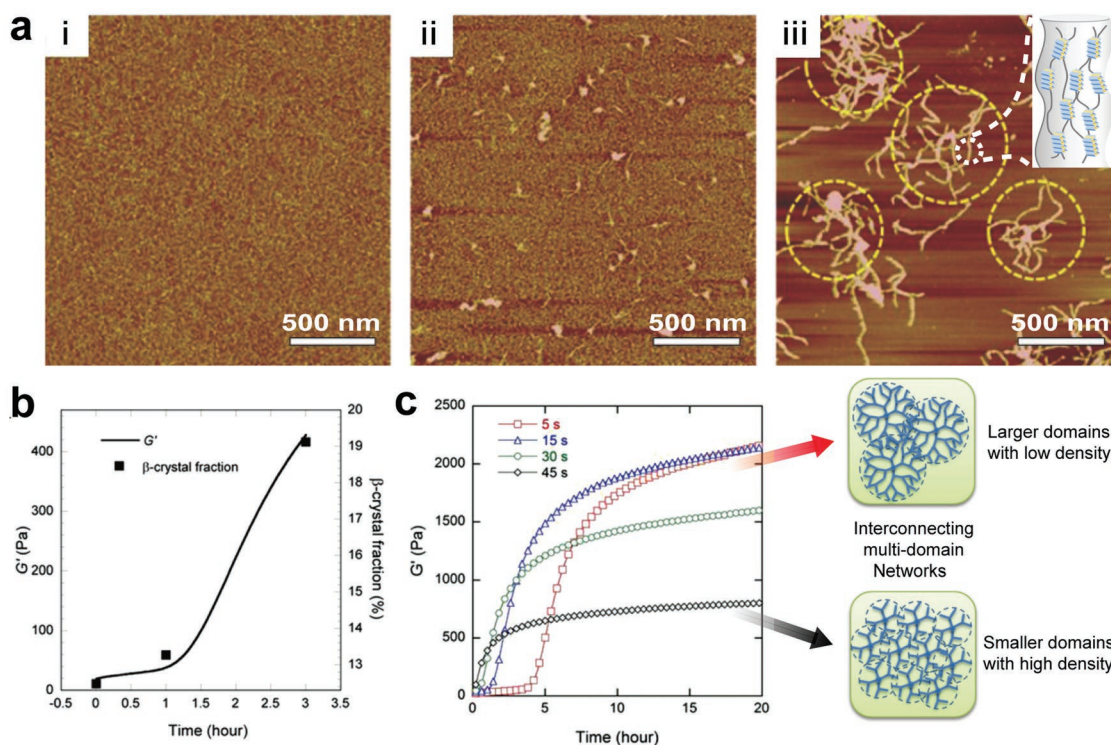


Figure 29. a) AFM images of RSF solution (0.04% w/v) at different gelation stages: i) before ultrasonication, ii) right after ultrasonication, and iii) 30 min after ultrasonication. Protein aggregation, nanofibrils, and nanofibril domains are clearly observed. b) The correspondence between storage modulus and content of β -crystallite within SF hydrogels. c) Rheological evolution of ultrasonicated SF solutions within different ultrasonication time periods. Both gelation time and storage modulus of samples with a shorter ultrasonication time period are higher, which is correlated to the density of domains. Reproduced with permission.^[25] Copyright 2014, Wiley-VCH.

used methods include the freeze-drying and salt leaching methods. The microstructures of SF scaffolds (e.g., pore size, pore walls thickness, and porosity) can also be programmed by changing the crystallization conditions, in a manner similar to that of other silk materials. The salt leaching method usually utilizes sodium chloride granules as the porogen,^[112] which is attributable to the insolubility of this salt in organic solvents such as HFIP; this results in the presence of pores inside the SF scaffolds (made from SF molecules dissolved in organic solvents) after leaching. Under such conditions, the dimensions of the created pores are determined by the size of the salt granules. However, the porosity is proportional to the amount of incorporated salt granules.^[112] It is reported that scaffolds prepared with smaller salt particles show a higher strength and modulus, due to the relatively smaller pore size, because a smaller pore size can give rise to thicker pore walls, which consequently offer more pathways for distributing the external stress and serve as barriers against crack propagation.^[112] In aqueous SF solutions, as the salts are partially soluble; thus, the dimensions of pores created because of salt leaching become smaller than the original dimensions of salt granules.^[97] Besides, the morphology of aqueous-based scaffolds are also rougher than that of organic solvent-based scaffolds. However, such rough surfaces can cause improved cell attachment in aqueous-based SF scaffolds.^[97]

Apart from the above-mentioned parameters, the amount of incorporated salt granules exert great impact on the local supersaturation of aqueous SF solutions. Specifically, the partial

dissolution of salt leads to the decrease of the solubility of SF molecules in solutions (referred to as the salting-out effect). Afterward, crystallization kinetics is accelerated and results in smaller pore sizes, thicker pore walls and larger porosities, which correspond to the stronger mechanical properties of SF scaffolds. In a similar manner, the concentration of SF solutions is also highly correlated to the structure and performance of SF scaffolds.^[112]

In case of the freeze-drying method, which is performed in the absence of foreign porogens, the pores in scaffold were generated by ice crystallite templates. In other words, the pore size is highly correlated to the ice crystallization process. Specifically, with lowering the freezing temperature (increasing thermodynamic driving force for ice crystallization), the pore size in scaffold become larger. It is noted via aforementioned freeze-drying method solely, the pore size created by ice crystallite sublimation is usually single-dispersed at a fixed temperature. However, scaffolds with hierarchical porous structures are more beneficial in tissue engineering with multiple functions. Different from the normal freeze-drying method (Figure 31a, i–iii) to produce monopore-sized scaffold, Wang et al.^[113] have designed and fabricated SF scaffolds with multiple pore size distribution by carefully tuning liquid–liquid separation of RSF aqueous solutions via adding an electrolyte (Figure 31a, i'–iii'). Accordingly, the addition of calcium ions can lead to aggregation of SF molecules and give rise to the phase separation: a highly dispersed dense proteinaceous phase and a dilute phase.

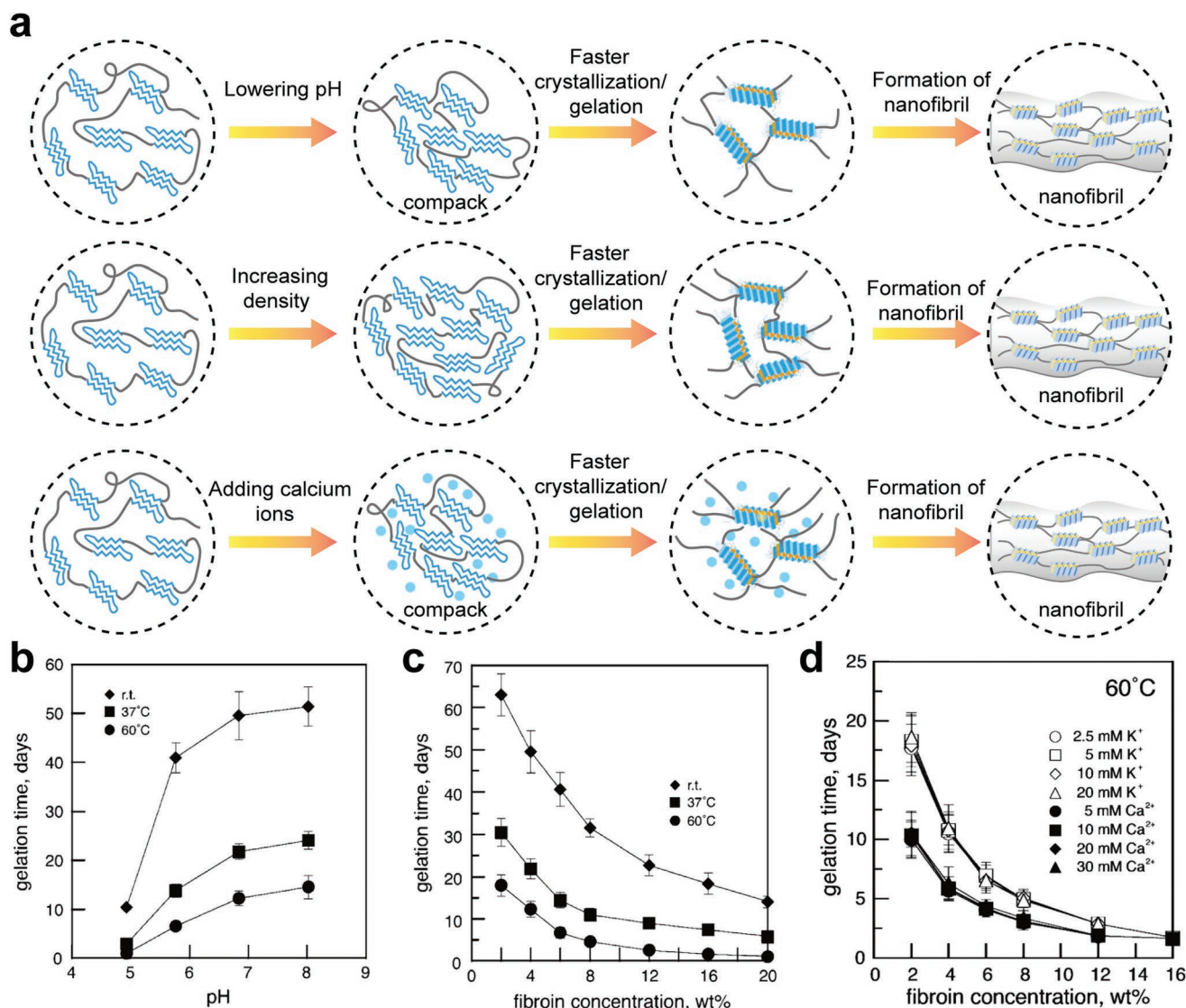


Figure 30. a) Schematic illustration of the influence of pH, SF concentration, and calcium ions on the SF solution gelation kinetics. b) Gelation time for 4 wt% SF aqueous solutions at various pH and temperature. c) Gelation time of SF aqueous solutions at various SF concentrations. d) Gelation time of 4 wt% SF aqueous solutions at various metallic ion concentrations. Reproduced with permission.^[109] Copyright 2004, American Chemical Society.

In the subsequent freezing process, the larger ice crystals are formed in the dilute phase, whereas the micro ice crystallites are generated from the highly dispersed proteinaceous phase. After ice sublimation, SF scaffolds with multiscale pores structure are obtained (Figure 31b).^[113]

Similar as the role of calcium ions, the addition of *n*-butanol to the SF aqueous solution can also generate phase separation; thus, SF crystallization is favored because of the relatively high local SF concentration.^[114] The post-methanol treatment can further induce a conformational transition in the fibroin molecules. Specifically, a longer immersion time results in a larger β -sheet content, and consequently increases the toughness of SF scaffolds. However, a certain limitation is associated with this post-treatment, due to the intrinsic characteristics of SF molecules. Recently, based on silk protein-protein interfacial bonding, micron-sized silk fibers (10–600 μm in size; obtained via partial

alkali hydrolysis)^[115] and silk particles (fabricated by physical milling)^[116] are used as reinforcement fillers to fabricate compact SF scaffolds. This enhancement is attributed to the high crystallinity of microsized silk fibers/particles and the strong interactions with SF molecules, which consequently promotes SF molecule crystallization. In this regard, the strength and tensile properties of SF scaffolds can be conveniently programmed, by changing the amount of reinforcement fillers used.

6. Conclusions and Perspectives

In this review, the hierarchical network structures and correlation between structure and performance of silk materials have been extensively discussed. In a bottom–top manner, the hierarchical network structure is identified to have five levels, that is,

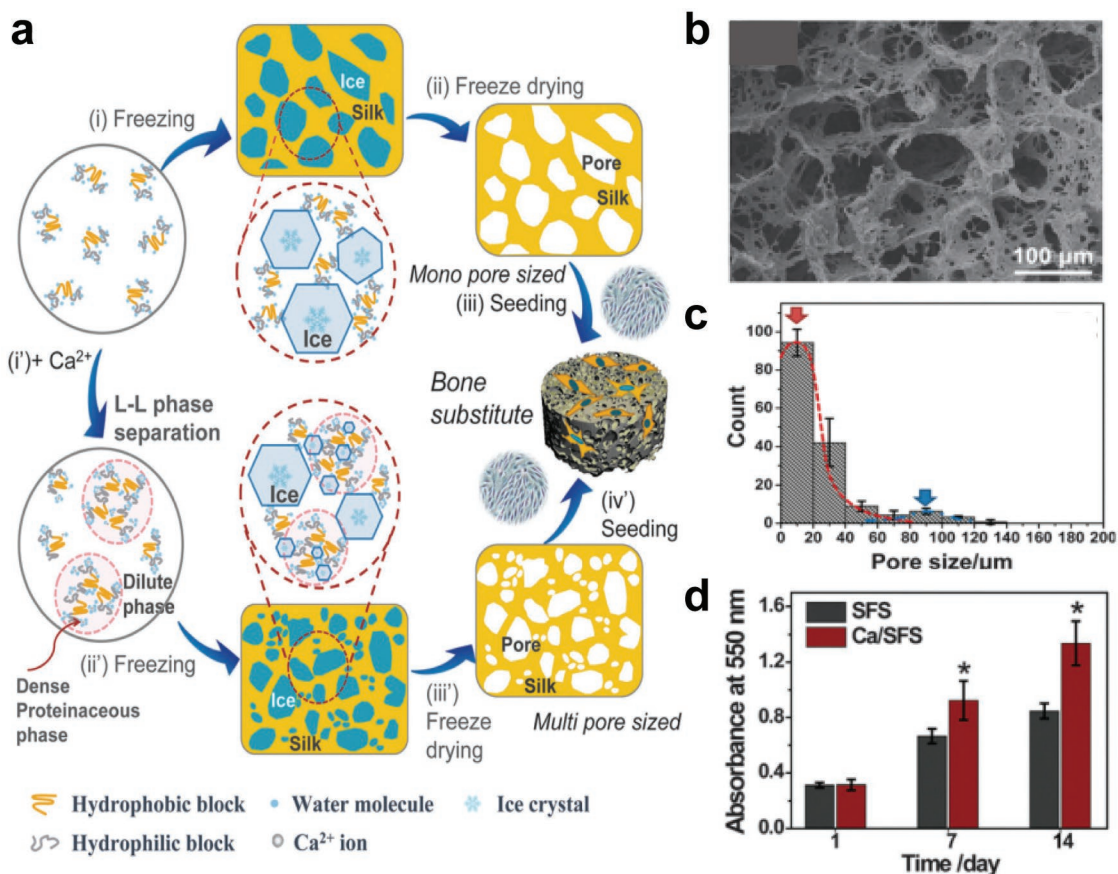


Figure 31. a) Schematic illustration of processing stages in the formation of calcium induced porous silk scaffolds. i–iii) Normal freeze-drying process to produce the monopore-sized scaffold. i'–iii') calcium ions induced multiphase freeze-drying process to produce the multipore-sized scaffold. b) SEM micrographs of scaffolds with multipore-sized structure. c) The pore size distribution has two distinct levels of pore structure peaks, tiny micropores (1–20 μm) appearing on the walls around the ≈90 μm bigger pores. d) Cell proliferation on SFSs and Ca/SFSs for 1, 7, and 14 days. Reproduced with permission.^[113] Copyright 2013, Royal Society of Chemistry.

amino acid sequence, secondary structure, β-crystallites, crystal network, and nanofibrils network, respectively. It follows that the outstanding mechanical performance of silk materials results from the nanofishnet topology structure of β-crystallites in the

molecular-scale crystal networks and from the strong linkage (friction) among nanofibrils in the mesoscopic nanofibrils networks (Figure 32). In comparison, although non-fibrous silk materials (i.e., films, hydrogels, and scaffolds) and silk fibers

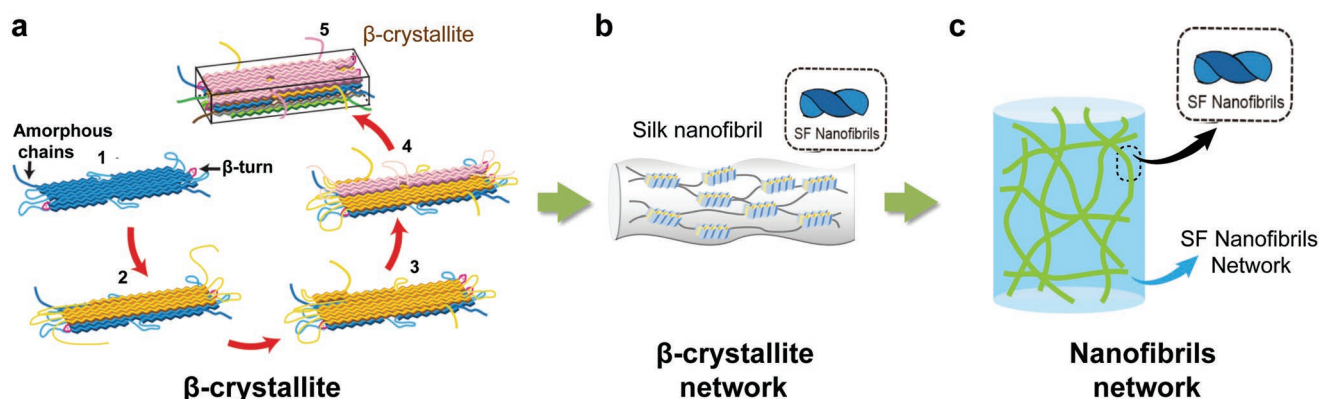


Figure 32. Schematic illustration of crystallization in controlling SF meso networks formation. This turns out to be the key principle in controlling mesoscopic structure engineering. a) Crystallization of β-sheets from different molecules gives rise to the formation of intermolecular β-crystallites. Reproduced with permission.^[111] Copyright 2016, Wiley-VCH. b) This leads to the formation of β-crystallites networks (nanofibrils). c) Nanofibrils will further interact to bundle or entangle to form nanofibrils networks, which play an important role in the macroscopic properties of SF materials.

share similar hierarchical structures, the difference in internanofibril interaction strength and nanofibril architecture results in distinct performance. To demonstrate how the hierarchical network structure affects the macroscopic performance (e.g., the rheological properties of SF hydrogels and mechanical stability of silk fibers, respectively), several mesoscopic engineering methods are applied to control different levels of the network structures of silk materials. The control of β -crystallization is crucial in mesoscopic engineering of flexible (i.e., SF) materials (Figure 32): Crystallization of β -sheets from different molecules gives rise to the formation of intermolecular β -crystallites (Figure 32a). This gives rise to β -crystallites networks (nanofibrils) formation (Figure 32b). Nanofibrils will further interact or entangle to form nanofibrils networks (Figure 32c), which plays an important role in the macroscopic properties of SF materials. Within the framework of the crystallization of SF molecule and network formation mechanism of silk materials, an increase in the crystallinity and a better alignment of β -crystallites will correspondingly result in stronger materials. Evidently, the knowledge obtained in this review will shed light on the preparation of ultraperformance silk materials from the crystallization and structural point of view.

Supporting Information

Supporting Information is available from the Wiley Online Library or from the author.

Acknowledgements

This work was financially supported by NUS AcRF Tier 1 (R-144-000-416-114), 111 project (B16029), National Nature Science Foundation (No. U1405226), Doctoral Fund of the Ministry of Education (20130121110018), China Postdoctoral Science Foundation (Grant No. 2017M612133), and the 1000 Talents Program funding from the Xiamen University.

Conflict of Interest

The authors declare no conflict of interest.

Keywords

hierarchical structure, mechanical performance, mesoscopic engineering, nucleation model, silk fibroin materials

Received: July 19, 2019

Revised: September 27, 2019

Published online: October 28, 2019

-
- [1] Z. Z. Shao, F. Vollrath, *Nature* **2002**, *418*, 741.
 [2] F. Vollrath, D. P. Knight, *Nature* **2001**, *410*, 541.
 [3] F. G. Omenetto, D. L. Kaplan, *Science* **2010**, *329*, 528.
 [4] A. Girotti, D. Orbanic, A. Ibanez-Fonseca, C. Gonzalez-Obeso, J. C. Rodriguez-Cabello, *Adv. Healthcare Mater.* **2015**, *4*, 2423.
 [5] H. Tao, D. L. Kaplan, F. G. Omenetto, *Adv. Mater.* **2012**, *24*, 2824.

- [6] B. Zhu, H. Wang, W. R. Leow, Y. Cai, X. J. Loh, M.-Y. Han, X. Chen, *Adv. Mater.* **2016**, *28*, 4250.
 [7] Y. Tian, X. J. Jiang, X. Chen, Z. Z. Shao, W. L. Yang, *Adv. Mater.* **2014**, *26*, 7393.
 [8] M. Zourab, J. E. Gough, R. V. Ulijn, *Adv. Mater.* **2006**, *18*, 655.
 [9] M. T. Wang, H. G. Braun, T. Kratzmuller, E. Meyer, *Adv. Mater.* **2001**, *13*, 1312.
 [10] N. B. Lin, X. Y. Liu, *Chem. Soc. Rev.* **2015**, *44*, 7917.
 [11] R. C. Liu, Q. Q. Deng, Z. Yang, D. W. Yang, M. Y. Han, X. Y. Liu, *Adv. Funct. Mater.* **2016**, *26*, 5534.
 [12] Z. W. Chen, H. H. Zhang, Z. F. Lin, Y. H. Lin, J. H. van Esch, X. Y. Liu, *Adv. Funct. Mater.* **2016**, *26*, 8978.
 [13] M. Zelzer, R. V. Ulijn, *Chem. Soc. Rev.* **2010**, *39*, 3351.
 [14] H. J. Jin, D. L. Kaplan, *Nature* **2003**, *424*, 1057.
 [15] C. P. Brown, C. Harnagea, H. S. Gill, A. J. Price, E. Traversa, S. Licoccia, F. Rosei, *ACS Nano* **2012**, *6*, 1961.
 [16] A. H. Simmons, C. A. Michal, L. W. Jelinski, *Science* **1996**, *271*, 84.
 [17] F. Vollrath, T. Holtet, H. C. Thogersen, S. Frische, *Proc. R. Soc. London, Ser. B* **1996**, *263*, 147.
 [18] S. Putthanasarat, N. Stribeck, S. A. Fossey, R. K. Eby, W. W. Adams, *Polymer* **2000**, *41*, 7735.
 [19] F. Hagn, L. Eisoldt, J. G. Hardy, C. Vendrely, M. Coles, T. Scheibel, H. Kessler, *Nature* **2010**, *465*, 239.
 [20] Y. Termonia, *Macromolecules* **1994**, *27*, 7378.
 [21] T. P. Knowles, A. W. Fitzpatrick, S. Meehan, H. R. Mott, M. Vendruscolo, C. M. Dobson, M. E. Welland, *Science* **2007**, *318*, 1900.
 [22] Z. Lin, W. D. Huang, J. F. Zhang, J. S. Fan, D. W. Yang, *Proc. Natl. Acad. Sci. U. S. A.* **2009**, *106*, 8906.
 [23] G. Q. Xu, L. Gong, Z. Yang, X. Y. Liu, *Soft Matter* **2014**, *10*, 2116.
 [24] N. Du, Z. Yang, X. Y. Liu, Y. Li, H. Y. Xu, *Adv. Funct. Mater.* **2011**, *21*, 772.
 [25] A. T. Nguyen, Q. L. Huang, Z. Yang, N. B. Lin, G. Q. Xu, X. Y. Liu, *Small* **2015**, *11*, 1039.
 [26] A. Karsai, Z. Martonfalvi, A. Nagy, L. Grama, B. Penke, M. S. Z. Kellermayer, *J. Struct. Biol.* **2006**, *155*, 316.
 [27] E. Oroudjev, J. Soares, S. Arcidiacono, J. B. Thompson, S. A. Fossey, H. G. Hansma, *Proc. Natl. Acad. Sci. U. S. A.* **2002**, *99*, 6460.
 [28] H. Tu, R. Yu, Z. F. Lin, L. Zhang, N. B. Lin, W. D. Yu, X. Y. Liu, *Adv. Funct. Mater.* **2016**, *26*, 9032.
 [29] C. Z. Zhou, F. Confalonieri, N. Medina, Y. Zivanovic, C. Esnault, T. Yang, M. Jacquet, J. Janin, M. Duguet, R. Perasso, Z. G. Li, *Nucleic Acids Res.* **2000**, *28*, 2413.
 [30] L. D. Koh, Y. Cheng, C. P. Teng, Y. W. Khin, X. J. Loh, S. Y. Tee, M. Low, E. Y. Ye, H. D. Yu, Y. W. Zhang, M. Y. Han, *Prog. Polym. Sci.* **2015**, *46*, 86.
 [31] S. W. Ha, H. S. Gracz, A. E. Tonelli, S. M. Hudson, *Biomacromolecules* **2005**, *6*, 2563.
 [32] C. Z. Zhou, F. Confalonieri, M. Jacquet, R. Perasso, Z. G. Li, J. Janin, *Proteins: Struct., Funct., Genet.* **2001**, *44*, 119.
 [33] Y. Takahashi, M. Gehoh, K. Yuzuriha, *Int. J. Biol. Macromol.* **1999**, *24*, 127.
 [34] S. A. Fossey, G. Nemethy, K. D. Gibson, H. A. Scheraga, *Biopolymers* **1991**, *31*, 1529.
 [35] A. Rising, H. Nimmervoll, S. Grip, A. Fernandez-Arias, E. Storckenfeldt, D. P. Knight, F. Vollrath, W. Engstrom, *Zool. Sci.* **2005**, *22*, 273.
 [36] G. P. Holland, R. V. Lewis, J. L. Yarger, *J. Am. Chem. Soc.* **2004**, *126*, 5867.
 [37] J. D. van Beek, S. Hess, F. Vollrath, B. H. Meier, *Proc. Natl. Acad. Sci. U. S. A.* **2002**, *99*, 10266.
 [38] A. E. Brooks, S. M. Stricker, S. B. Joshi, T. J. Kamerzell, C. R. Middaugh, R. V. Lewis, *Biomacromolecules* **2008**, *9*, 1506.
 [39] C. Y. Hayashi, R. V. Lewis, *BioEssays* **2001**, *23*, 750.

- [40] Y. Liu, A. Spohner, D. Porter, F. Vollrath, *Biomacromolecules* **2008**, *9*, 116.
- [41] A. C. Mendes, E. T. Baran, R. L. Reis, H. S. Azevedo, *Wiley Interdiscip. Rev.: Nanomed. Nanobiotechnol.* **2013**, *5*, 582.
- [42] C. C. Guo, J. Zhang, X. G. Wang, A. T. Nguyen, X. Y. Liu, D. L. Kaplan, *Small* **2017**, *13*, 1702266.
- [43] X. Wu, X. Y. Liu, N. Du, G. Q. Xu, B. W. Li, *Appl. Phys. Lett.* **2009**, *95*, 093703.
- [44] S. Keten, Z. P. Xu, B. Ihle, M. J. Buehler, *Nat. Mater.* **2010**, *9*, 359.
- [45] Z. G. Gong, L. Huang, Y. H. Yang, X. Chen, Z. Z. Shao, *Chem. Commun.* **2009**, *48*, 7506.
- [46] N. Du, X. Y. Liu, J. Narayanan, L. A. Li, M. L. M. Lim, D. Q. Li, *Biophys. J.* **2006**, *91*, 4528.
- [47] X. Chen, Z. Z. Shao, N. S. Marinkovic, L. M. Miller, P. Zhou, M. R. Chance, *Biophys. Chem.* **2001**, *89*, 25.
- [48] X. Chen, Z. Z. Shao, D. P. Knight, F. Vollrath, *Proteins: Struct., Funct., Bioinf.* **2007**, *68*, 223.
- [49] T. Lefevre, M. E. Rousseau, M. Pezolet, *Biophys. J.* **2007**, *92*, 2885.
- [50] M. E. Rousseau, T. Lefevre, L. Beaulieu, T. Asakura, M. Pezolet, *Biomacromolecules* **2004**, *5*, 2247.
- [51] Y. H. Yang, Z. Z. Shao, X. Chen, P. Zhou, *Biomacromolecules* **2004**, *5*, 773.
- [52] M. Carrion-Vazquez, A. F. Oberhauser, T. E. Fisher, P. E. Marszalek, H. B. Li, J. M. Fernandez, *Prog. Biophys. Mol. Biol.* **2000**, *74*, 63.
- [53] J. Z. Shao, J. H. Zheng, J. Q. Liu, C. M. Carr, *J. Appl. Polym. Sci.* **2005**, *96*, 1999.
- [54] M. E. Rousseau, L. Beaulieu, T. Lefevre, J. Paradis, T. Asakura, M. Pezolet, *Biomacromolecules* **2006**, *7*, 2512.
- [55] L. F. Drummy, B. L. Farmer, R. R. Naik, *Soft Matter* **2007**, *3*, 877.
- [56] C. Dicko, D. Knight, J. M. Kenney, F. Vollrath, *Biomacromolecules* **2004**, *5*, 758.
- [57] M. Canetti, A. Seves, F. Secundo, G. Vecchio, *Biopolymers* **1989**, *28*, 1613.
- [58] G. Y. Li, P. Zhou, Z. Z. Shao, X. Xie, X. Chen, H. H. Wang, L. J. Chunyu, T. Y. Yu, *Eur. J. Biochem.* **2001**, *268*, 6600.
- [59] A. Sinsawat, S. Putthanarat, Y. Magoshi, R. Pachter, R. K. Eby, *Polymer* **2002**, *43*, 1323.
- [60] J. E. Trancik, J. T. Czernuszka, F. I. Bell, C. Viney, *Polymer* **2006**, *47*, 5633.
- [61] Y. Xing, C. Shi, J. Zhao, W. Qiu, N. Lin, J. Wang, X. B. Yan, W. D. Yu, X. Y. Liu, *Small* **2017**, *13*, 1702390.
- [62] M. Heim, D. Keerl, T. Scheibel, *Angew. Chem., Int. Ed.* **2009**, *48*, 3584.
- [63] T. H. Zhang, X. Y. Liu, *Chem. Soc. Rev.* **2014**, *43*, 2324.
- [64] S. J. Ling, C. X. Li, J. Adamcik, S. H. Wang, Z. Z. Shao, X. Chen, R. Mezzenga, *ACS Macro Lett.* **2014**, *3*, 146.
- [65] L. Y. Zhao, Q. L. Zou, X. H. Yan, *Bull. Chem. Soc. Jpn.* **2019**, *92*, 70.
- [66] K. Ariga, D. T. Leong, T. Mori, *Adv. Funct. Mater.* **2018**, *28*, 1702905.
- [67] M. Komiya, K. Yoshimoto, M. Sisido, K. Ariga, *Bull. Chem. Soc. Jpn.* **2017**, *90*, 967.
- [68] T. Iizuka, H. Sezutsu, K. Tatematsu, I. Kobayashi, N. Yonemura, K. Uchino, K. Nakajima, K. Kojima, C. Takabayashi, H. Machii, K. Yamada, H. Kurihara, T. Asakura, Y. Nakazawa, A. Miyawaki, S. Karasawa, H. Kobayashi, J. Yamaguchi, N. Kuwabara, T. Nakamura, K. Yoshii, T. Tamura, *Adv. Funct. Mater.* **2013**, *23*, 5232.
- [69] J. Xu, Q. L. Dong, Y. Yu, B. L. Niu, D. F. Ji, M. W. Li, Y. P. Huang, X. Chen, A. J. Tan, *Proc. Natl. Acad. Sci. U. S. A.* **2018**, *115*, 8757.
- [70] Y. Kuwana, H. Sezutsu, K. Nakajima, Y. Tamada, K. Kojima, *PLoS One* **2014**, *9*, e105325.
- [71] F. Teule, Y. G. Miao, B. H. Sohn, Y. S. Kim, J. J. Hull, M. J. Fraser, R. V. Lewis, D. L. Jarvis, *Proc. Natl. Acad. Sci. U. S. A.* **2012**, *109*, 923.
- [72] N. C. Tansil, Y. Li, C. P. Teng, S. Y. Zhang, K. Y. Win, X. Chen, X. Y. Liu, M. Y. Han, *Adv. Mater.* **2011**, *23*, 1463.
- [73] K. Li, J. L. Zhao, J. J. Zhang, J. Y. Ji, Y. Ma, X. Y. Liu, H. Y. Xu, *ACS Biomater. Sci. Eng.* **2015**, *1*, 494.
- [74] L. Y. Cai, H. L. Shao, X. C. Hu, Y. P. Zhang, *ACS Sustainable Chem. Eng.* **2015**, *3*, 2551.
- [75] Q. Wang, C. Y. Wang, M. C. Zhang, M. Q. Jian, Y. Y. Zhang, *Nano Lett.* **2016**, *16*, 6695.
- [76] N. M. Pugno, *PLoS One* **2014**, *9*, e93079.
- [77] X. X. Xia, Z. G. Qian, C. S. Ki, Y. H. Park, D. L. Kaplan, S. Y. Lee, *Proc. Natl. Acad. Sci. U. S. A.* **2010**, *107*, 14059.
- [78] Z. Lin, Q. Q. Deng, X. Y. Liu, D. W. Yang, *Adv. Mater.* **2013**, *25*, 1216.
- [79] M. Stark, S. Grip, A. Rising, M. Hedhammar, W. Engstrom, G. Hjalm, J. Johansson, *Biomacromolecules* **2007**, *8*, 1695.
- [80] A. Heidebrecht, L. Eisdoldt, J. Diehl, A. Schmidt, M. Geffers, G. Lang, T. Scheibel, *Adv. Mater.* **2015**, *27*, 2189.
- [81] Q. F. Peng, Y. P. Zhang, L. Lu, H. L. Shao, K. K. Qin, X. C. Hu, X. X. Xia, *Sci. Rep.* **2016**, *6*, 36473.
- [82] S. W. Ha, A. E. Tonelli, S. M. Hudson, *Biomacromolecules* **2005**, *6*, 1722.
- [83] D. M. Phillips, L. F. Drummy, D. G. Conrady, D. M. Fox, R. R. Naik, M. O. Stone, P. C. Trulove, H. C. De Long, R. A. Mantz, *J. Am. Chem. Soc.* **2004**, *126*, 14350.
- [84] Y. Xu, Y. P. Zhang, H. L. Shao, X. C. Hu, *Int. J. Biol. Macromol.* **2005**, *35*, 155.
- [85] Q. Wang, Y. H. Yang, X. Chen, Z. Z. Shao, *Biomacromolecules* **2012**, *13*, 1875.
- [86] J. P. Yan, G. Q. Zhou, D. P. Knight, Z. Z. Shao, X. Chen, *Biomacromolecules* **2010**, *11*, 1.
- [87] W. Wei, Y. P. Zhang, Y. M. Zhao, J. Luo, H. L. Shao, X. C. Hu, *Mater. Sci. Eng., C* **2011**, *31*, 1602.
- [88] S. Ling, Z. Qin, C. Li, W. Huang, D. L. Kaplan, M. J. Buehler, *Nat. Commun.* **2017**, *8*, 1387.
- [89] I. C. Um, H. Y. Kweon, K. G. Lee, D. W. Ihm, J. H. Lee, Y. H. Park, *Int. J. Biol. Macromol.* **2004**, *34*, 89.
- [90] D. M. Phillips, L. F. Drummy, R. R. Naik, H. C. De Long, D. M. Fox, P. C. Trulove, R. A. Mantz, *J. Mater. Chem.* **2005**, *15*, 4206.
- [91] G. Q. Zhou, Z. Z. Shao, D. P. Knight, J. P. Yan, X. Chen, *Adv. Mater.* **2009**, *21*, 366.
- [92] M. J. Sun, Y. P. Zhang, Y. M. Zhao, H. L. Shao, X. C. Hu, *J. Mater. Chem.* **2012**, *22*, 18372.
- [93] H. Pan, Y. P. Zhang, Y. C. Hang, H. L. Shao, X. C. Hu, Y. M. Xu, C. Feng, *Biomacromolecules* **2012**, *13*, 2859.
- [94] H. Kim, L. Che, Y. Ha, W. Ryu, *Mater. Sci. Eng., C* **2014**, *40*, 324.
- [95] L. Zhou, Q. Wang, J. C. Wen, X. Chen, Z. Z. Shao, *Polymer* **2013**, *54*, 5035.
- [96] D. N. Rockwood, R. C. Preda, T. Yucel, X. Q. Wang, M. L. Lovett, D. L. Kaplan, *Nat. Protoc.* **2011**, *6*, 1612.
- [97] C. Vepari, D. L. Kaplan, *Prog. Polym. Sci.* **2007**, *32*, 991.
- [98] I. Greving, M. Z. Cai, F. Vollrath, H. C. Schniepp, *Biomacromolecules* **2012**, *13*, 676.
- [99] J. E. Bressner, B. Marelli, G. K. Qin, L. E. Klinker, Y. J. Zhang, D. L. Kaplan, F. G. Omenetto, *J. Mater. Chem. B* **2014**, *2*, 4983.
- [100] C. Y. Jiang, V. V. Tsukruk, *Adv. Mater.* **2006**, *18*, 829.
- [101] X. Y. Wang, H. J. Kim, P. Xu, A. Matsumoto, D. L. Kaplan, *Langmuir* **2005**, *21*, 11335.
- [102] N. Minoura, M. Tsukada, M. Nagura, *Polymer* **1990**, *31*, 265.
- [103] G. Freddi, M. Romano, M. R. Massafra, M. Tsukada, *J. Appl. Polym. Sci.* **1995**, *56*, 1537.
- [104] J. W. Yin, E. Q. Chen, D. Porter, Z. Z. Shao, *Biomacromolecules* **2010**, *11*, 2890.
- [105] T. Yucel, P. Cebe, D. L. Kaplan, *Biophys. J.* **2009**, *97*, 2044.
- [106] X. Q. Wang, J. A. Kluge, G. G. Leisk, D. L. Kaplan, *Biomaterials* **2008**, *29*, 1054.
- [107] G. G. Leisk, T. J. Lo, T. Yucel, Q. Lu, D. L. Kaplan, *Adv. Mater.* **2010**, *22*, 711.

- [108] Y. X. Liu, S. J. Ling, S. H. Wang, X. Chen, Z. Z. Shao, *Biomater. Sci.* **2014**, *2*, 1338.
- [109] U. J. Kim, J. Y. Park, C. M. Li, H. J. Jin, R. Valluzzi, D. L. Kaplan, *Biomacromolecules* **2004**, *5*, 786.
- [110] X. L. Wu, J. Hou, M. Z. Li, J. N. Wang, D. L. Kaplan, S. Z. Lu, *Acta Biomater.* **2012**, *8*, 2185.
- [111] R. Nazarov, H. J. Jin, D. L. Kaplan, *Biomacromolecules* **2004**, *5*, 718.
- [112] U. J. Kim, J. Park, H. J. Kim, M. Wada, D. L. Kaplan, *Biomaterials* **2005**, *26*, 2775.
- [113] H. Wang, X. Y. Liu, Y. J. Chuah, J. C. H. Goh, J. L. Li, H. Y. Xu, *Chem. Commun.* **2013**, *49*, 1431.
- [114] Z. B. Cao, J. C. Wen, J. R. Yao, X. Chen, Y. S. Ni, Z. Z. Shao, *Mater. Sci. Eng., C* **2013**, *33*, 3522.
- [115] B. Mandal, A. Grinberg, E. S. Gil, B. Panilaitis, D. Kaplan, *J. Tissue Eng. Regener. Med.* **2012**, *6*, 181.
- [116] E. S. Gil, J. A. Kluge, D. N. Rockwood, R. Rajkhowa, L. J. Wang, X. G. Wang, D. L. Kaplan, *J. Biomed. Mater. Res., Part A* **2011**, *99A*, 16.